I. Physikalisches Institut

Justus-Liebig-Universität Gießen

Point Defects in Oxide and Nitride Semiconductors

Dissertation zur Erlangung des Doktorgrades der Naturwissenschaften

am Fachbereich 07 der Justus-Liebig-Universität Gießen

vorgelegt von Jan Eric Stehr

Gutachter: 1. Prof. Dr. Bruno K. Meyer

2. Prof. Dr. Detlev M. Hofmann

Datum der Promotion: 12. Dezember 2011

Table of Contents

1 Introduction

Semiconducting oxides and nitrides are, due to their large band gap energies, the two most interesting groups to employ in optoelectronic devices operating in the visible and UV spectral range. There are to mention Zinc Oxide (ZnO) and Gallium Oxide (Ga_2O_3) on the oxide side and Gallium Nitride (GaN) together with Indium Nitride (InN) and Aluminum Nitride (AlN) for the nitrides. These semiconducting materials combine unique properties on their crystallography and growth mechanisms, as well as on their optical, electrical and magnetic properties. Hence it is not surprising that with these materials it was possible to build novel displays, light emitters, data storages, bio- and environmental-sensors and energy generating- or saving-devices. For any device application one has to solve problems related to the growth mechanisms of the materials. Defect characterization of the materials is a necessity, since relevant physical properties are affected by intrinsic and extrinsic defects. There are various characterization tools ranging from the electrical- or optical- and magnetic methods to microscopy's such as electron- or atomic force microscopy which give information on the structural- or surface-properties. The choice which one suits best to achieve the given purpose depends on the specific information one needs.

In the pool of characterization methods magnetic resonance spectroscopy is a powerful tool, providing access to information on defect structures, chemical identity, magnetic properties and also energetic positions. Thus Electron Paramagnetic Resonance (EPR) in conjunction with optical spectroscopy (photo-EPR) was chosen in this work to study defects in ZnO, AlN and Ga_2O_3 to achieve a better understanding of these materials and their defects in order to help to optimize the growth parameters and conditions as well as device designing.

This work is divided in three parts dealing with the material systems ZnO, AlN and Ga_2O_3, respectively. Chapter 1 consists of a short introduction to the technique of EPR. The second chapter of this work focusses on the nitrogen center in ZnO and whether it acts as a shallow or deep acceptor. Defects in AlN are investigated in the third chapter and the last part (chapter 4) treats the characterization of point defects in Ga_2O_3. In the beginning of each chapter there are more detailed introductions to specific material properties and the related problems.

2 Theoretical background

2.1 Electron Paramagnetic Resonance

Magnetic resonance spectroscopy is a topic for several spectroscopy methods. The most common technique is nuclear magnetic resonance (NMR) spectroscopy. In this technique the nuclear magnetic moments of a sample absorb radio frequency energy to induce transitions between the nuclear Zeeman levels. From the energy positions of these transitions one can obtain information about the atomic nuclei involved. NMR is used in the fields of biology, chemistry, geology, medicine and material sciences. Electron paramagnetic resonance (EPR) and electron spin resonance (ESR) spectroscopy are synonymous terms used to describe the same technique. Here, transitions between the electron Zeeman levels are induced by exposing the sample to microwave radiation. This technique is used in the fields of chemistry, materials science, and physics to perform basic research.

The major limitation of EPR is the necessity to have a net spin angular momentum, i.e. at least one unpaired electron spin. However, there are many materials fulfilling this requirement, for example by the presence of point defects such as vacancies, antisites, and impurities. Most of these defects can contain unpaired electrons. For the ones not being in a paramagnetic state there is the possibility to illuminate the material and therefore to convert the defects into a paramagnetic charge state.

2.1.1 Basic principles of EPR

A simple mathematical model for the description of resonance phenomena with relaxation effects was given by Bloch et al. [1]. One starts with the Magnetization $\vec{M} = n\langle\vec{\mu}\rangle_{average}$ which is defined as the average magnetic dipole moment μ per standard volume, n is the spin density.

In a static magnetic field $\vec{B}_0$ the magnetization $\vec{M}$ has a thermal equilibrium $\vec{M}_0$ which is connected to the static magnetic field through the susceptibility χ, therefore $\vec{M}_0 = \chi\vec{B}_0$. When $\vec{M}$ differs from $\vec{M}_0$ a simple rate model describes the process to obtain an equilibrium state. For a magnetic field along the z direction of the coordinate system

$\vec{B} = (0,0,B_z)$ the alteration of M_z is related to an alteration of the magnetic energy $E = -M_z B_z$. Alterations of M_x or M_y are independent of the energy, since the scalar product vanishes $\left(E = -M_{x,y} B_z = 0\right)$. Hence it is in principle necessary to distinguish between the magnetization component in magnetic field direction and the components perpendicular to the magnetic field direction.

In a process leading to the equilibrium of M_z energy has to be transferred into or out of the spin system. For a solid state this is only possible through phonon interactions, a coupling to the lattice of the crystal. Therefore the equation looks like:

$$\frac{d}{dt} M_z = \frac{M_0 - M_z}{T_1} \tag{2.1}$$

T_1 is a value for the coupling of the spin system to the phonon system and is known as the longitudinal relaxation time or spin-lattice relaxation time. This is the characteristic time that an electron needs to relax from an excited state to its ground state by emitting one or more phonons.

The equations for the transversal magnetization components are the following:

$$\frac{d}{dt} M_x = -\frac{M_x}{T_2} \tag{2.2}$$

$$\frac{d}{dt} M_y = -\frac{M_y}{T_2}$$

T_2 describes the transversal relaxation time or spin-spin relaxation time. This is due to the fact that M_x and M_y can change through interactions with the spin system without a coupling to the lattice. T_2 is also a measure of how long the single dipole moments contributing to M_x and M_y are staying in phase. In most cases T_2 is shorter than T_1.

However, one must also take into account that the magnetization $\vec{M}$ precesses around $\vec{B}_0$. This process is best described by Ehrenfest's theorem in analogy to the classical gyroscope equation [2].

$$\frac{d}{dt} \vec{M} = \gamma \vec{B} \times \vec{M} \tag{2.3}$$

$$\gamma = g_e \mu_B \tag{2.4}$$

Where γ is the gyromagnetic ratio, μ_B is the Bohr magneton and g_e is the electron g-value, which equals 2.00232 for a free electron. Combination of equations (2.1), (2.2) and (2.3) yields the Bloch equations [3, 4]:

$$\frac{d}{dt}M_x = \gamma\left(\vec{B} \times \vec{M}\right)_x - \frac{M_x}{T_2} \tag{2.5}$$

$$\frac{d}{dt}M_y = \gamma\left(\vec{B} \times \vec{M}\right)_y - \frac{M_y}{T_2}$$

$$\frac{d}{dt}M_z = \gamma\left(\vec{B} \times \vec{M}\right)_z + \frac{M_0 - M_z}{T_1}$$

In a resonance experiment, it is necessary to apply another high frequency field. It is described by a magnetic field $\vec{B}_1$ in the xy-plane which rotates with the frequency ω. The average absorption power is given by the following equation:

$$P = \frac{1}{T}\int_0^T \vec{B}\frac{d\vec{M}}{dt}dt = \omega B_1 M_{y'} \tag{2.6}$$

In this case B_1 is the amplitude of the high frequency field and $M_{y'}$ is the y component of the magnetization in a frame of reference rotating with B_1. From equation (2.6) it is obvious that $M_{y'}$ is responsible for the absorption. Since $M_{x'}$ is not present in equation (2.6), the power dependence is independent of it and therefore $M_{x'}$ is connected to the dispersion. Now the Bloch equations have to be solved for the rotating frame of reference. This yields the following equations for $M_{x'}$ and $M_{y'}$ [1]:

$$M_{x'} = \frac{\gamma(\gamma B_0 - \omega)T_2^2 M_0 B_1}{1 + (\gamma B_0 - \omega)^2 T_2^2 + \gamma^2 B_1^2 T_1 T_2} \tag{2.7}$$

$$M_{y'} = \frac{-\gamma T_2 M_0 B_1}{1 + (\gamma B_0 - \omega)^2 T_2^2 + \gamma^2 B_1^2 T_1 T_2} \tag{2.8}$$

The first thing one can realize from these equations is that $M_{x'}$ vanishes if the resonance condition $\omega = \gamma B_0$ is fulfilled, i.e. the dispersion equals zero for the resonance case. On the other hand, reaches $|M_{y'}|$ its maximum value and therefore the absorption signal is also at its maximum value in the resonance case. For resonance conditions, equation (2.8) becomes:

$$M_{y\prime} = \frac{-\gamma T_2 M_0 B_1}{1 + \gamma^2 B_1^2 T_1 T_2} = \frac{-\gamma T_2 M_0 B_1}{1 + S} \tag{2.9}$$

Introducing the saturation parameter $S = \gamma^2 B_1^2 T_1 T_2$. During an EPR measurement, the magnetizations $M_{x\prime}$ and $M_{y\prime}$of the sample are measured. If a linear detector is used, the absorption signal A_{abs} is proportional to the magnetization $M_{y\prime}$: $A_{abs} \propto M_{y\prime}$. Taking a closer look at the absorption signal A_{abs} in dependence of the amplitude of the high frequency microwave field B_1 and therefore at the microwave power $P_{mw} \propto B_1^2$, the indication saturation parameter becomes obvious.

As long as the saturation parameter is small against one ($S \ll 1$), the magnetization $M_{y\prime}$ increases proportional to B_1 (see equation (2.9)). Thus, in this region the absorption signal increases with B_1 and is therefore proportional to the square root of the microwave power: $A_{abs} \propto \sqrt{P_{mw}}$.

In the case ($S \geq 1$), which means that γB_1 is big against the product of the inverse relaxation times $\frac{1}{T_1 T_2}$, saturation occurs. Therefore the absorption signal is no longer proportional to B_1, it increases slower and reaches its maximum for $S = 1$. If the saturation parameter increases further ($S \gg 1$) the absorption signal decreases. The dependence of the absorption signal of the amplitude of the magnetic field B_1 is shown in Figure 2.1.

With this knowledge, it is possible to determine the relaxation times T_1 and T_2 with microwave power dependent EPR measurements. From equation (2.9) it is also obvious that the absorption signal is expected to have the shape of a Lorentzian line for neglected saturation. Nevertheless, in the experiment a Gaussian line shape is observed, which is due to inhomogeneous line broadening. This behavior can be caused by non-resolved hyperfine interactions or in rare cases by in-homogeneities of the magnetic field.

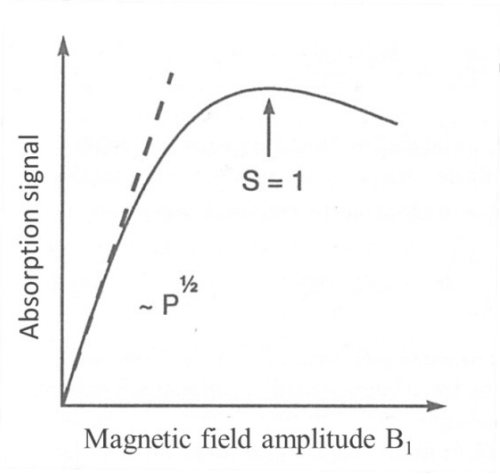

Figure 2.1: Dependence of the EPR absorption signal on the amplitude of the high frequency microwave field B_1. Since B_1 is proportional to the microwave power, the absorption signal increases linearly with the square root of the microwave power.

2.1.2 The spin Hamilton operator

To describe a paramagnetic ion in a crystalline solid the following Hamilton operator is used [5]:

$$H^0 = H_{el} + H_{crys} + H_{SO} + H_{SS} \tag{2.10}$$

The electric energy of the paramagnetic ion is described by H_{el}, H_{crys} is the interaction with the electric crystal field of the neighboring atoms. The spin-orbit- and the spin-spin-interaction energies are given by H_{SO} and H_{SS}. In the presence of an external magnetic field an additional operator describing the magnetic properties has to be added to H^0. Except for some special cases it is not possible to find an exact solution for the above Hamilton operator. This is due to the complexity between the interactions of the different terms. There are several approaches to obtain approximate solutions, for instance the crystal field theory.

Fortunately it is not necessary to solve the above Hamilton operator to discuss and understand magnetic resonance experiments. The energy of a microwave quantum in a typical EPR experiment is in the range of 10^{-5} eV. In contrast, the energy splitting between the ground state and the first excited state for defects in solids due to crystal

field or spin-orbit interaction is typically 1 eV. Therefore only ground states or occupied thermic excited states can be examined in magnetic resonance experiments. The spin-Hamilton-operator H_S [2] is based on this fact. It describes the manifold of the ground state only.

H_S is given by several terms, containing the operators of the magnetic field B, the electron spin S, and the nuclear spin I in the shape of $B^l S^m I^n$. Each of these terms encloses a coupling tensor, whose components can be determined by experiments or calculated theoretically.

The exponentials l, m, and n are subject to several restrictions. First, the time-reversal invariance of the electromagnetic interaction requires that the spin-Hamilton-operator is also invariant against time-reversals [1]. Due to this behavior the sum of l+m+n has to be even. Hence terms with the shape of BSI or S^3 will not be found in H_S. From the triangle inequality it is obvious, that $m \leq 2S$ and $n \leq 2I$ is valid [2]. So terms with S^2 can only appear for a spin $S \geq 1$. It is also found empirically that terms with large values of l, m, and n deliver only small contributions to H_S. Therefore it is adequate to consider only quadratic terms, or if those have no contribution, terms of the forth order [6].

To describe the defects in this work only the following parts of the spin-Hamilton-operator are necessary:

$$H = H_{EZ} + H_{FS} + H_{HF} + H_{NZ} + H_{NQ} \tag{2.11}$$

The individual terms are described in the following chapters.

The energy ranges of the different contributions of the spin Hamiltonian are compared in Figure 2.2. The comparison is done on the frequency scale, since in EPR the unit of interaction parameters is MHz, and also converted to a temperature scale.

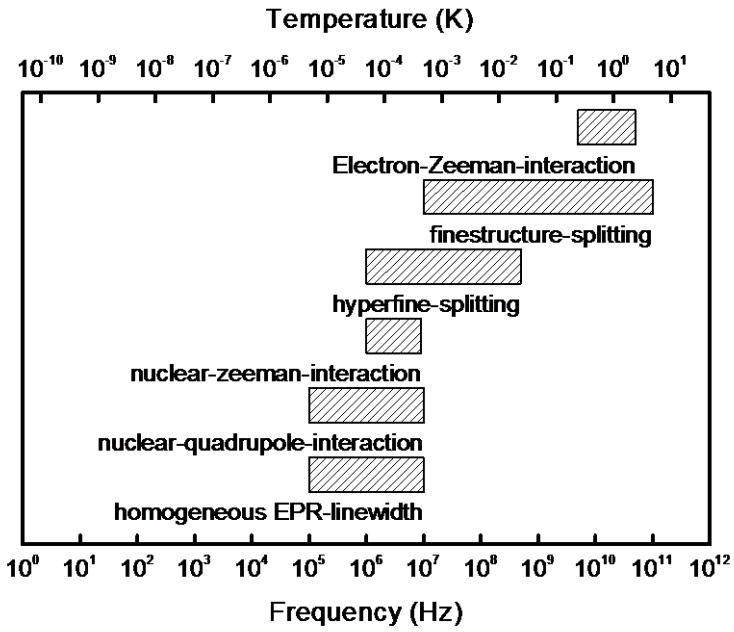

Figure 2.2: Energy scale comparison of the different interactions contributing to the spin Hamilton operator on the frequency and temperature scale.

2.1.3 Zeeman splitting

The description of the Zeeman splitting starts from the magnetic moment of an electron in a static magnetic field. The energy of a magnetic dipole in a magnetic field is defined as [7]:

$$E = -\vec{\mu} \cdot \vec{B} \tag{2.12}$$

Where $\vec{\mu}$ is the magnetic moment and $\vec{B}$ is the magnetic field. If the z axis is assumed to be along the direction of B, then the z component of the electron spin magnetic moment is [7]:

$$\mu_z = -\mu_B g m_s \tag{2.13}$$

With the Bohr magneton μ_B, the electron spin component along the z axis m_s, and the electron g-value. The negative sign is due to the negative charge of the electron. By combining equation (2.12) and equation (2.13) one obtains:

$$E = g\mu_B B m_S \tag{2.14}$$

From quantum mechanics it is known that the eigenvalues of m_s are discrete and range from -S to S with steps of 1, which results in 2S+1 possible values. For a free electron with a spin of S = ½ the values of m_s are +½ (spin up) and -½ (spin down). Therefore the Zeeman energies of these two states can be written as:

$$E = \pm\frac{1}{2} g\mu_B B \tag{2.15}$$

To induce an EPR transition between these two states it is necessary to expose the system to electromagnetic radiation of the energy hν matching the energy difference ΔE of these two states. The resonance condition for a spin a system with S = ½ is given by the following expression [7]:

$$\Delta E = E_+ - E_- = h\nu = g\mu_B B \tag{2.16}$$

EPR transitions are restricted by selection rules, only transitions with $\Delta m_s = \pm 1$ are allowed. Figure 2.3 shows the splitting of the energy levels with increasing magnetic field for an S = ½ spin system and the allowed EPR transition between them. If S is larger than ½ it is possible to observe "forbidden" transitions which follow the selection rule $\Delta m_s = \pm 2$.

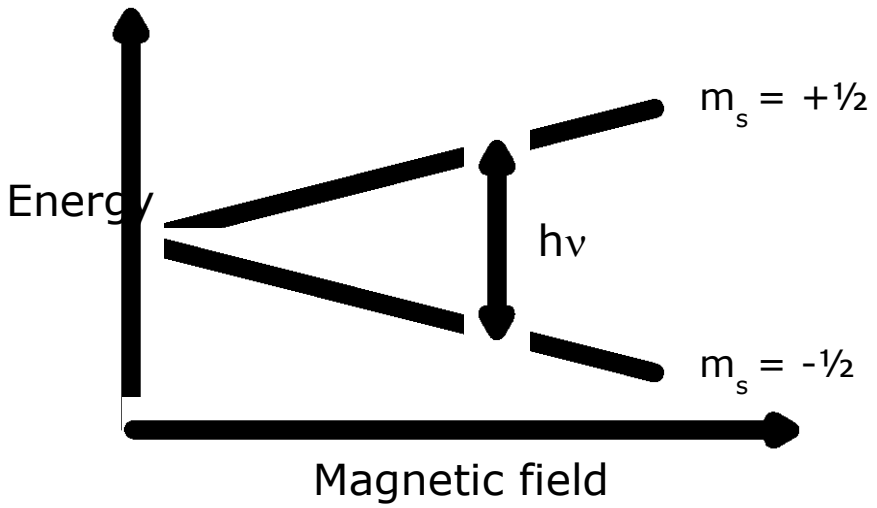

Figure 2.3: Schematic energy level diagram for an S = ½ system. The vertical arrow indicates the transition at the resonance position.

For the most samples this simple model is not sufficient, however, since the g-value often differs from the free electron value of 2.00232. This is due to spin-orbit and spin-spin interactions. Therefore the electron-Zeeman term of the spin-Hamilton operator has to be modified:

$$H_{EZ} = \mu_B \vec{B} \hat{g} \vec{S} \tag{2.17}$$

The coupling tensor $\hat{g}$ between the magnetic field and the electron spin describes all deviations from the free electron g-value. The components of the g-tensor are given by [1]:

$$g_{ij} = g_e \delta_{ij} - 2\lambda \sum_{n \neq 0} \frac{\langle 0|\vec{L}_i|n\rangle\langle n|\vec{L}_j|0\rangle}{E_n - E_0} \tag{2.18}$$

Here $|0\rangle$ is the orbital wave function of the ground state and $|n\rangle$ the orbital wave function of the excited state. $\vec{L}_i$ and $\vec{L}_j$ are the operators of the orbital angular momentum and λ is the spin-orbit-coupling constant. From equation (2.18) it is obvious that the components of $\hat{g}$ differ the more from g_e, the more the influence of the spin-orbit-coupling λ is increasing. On the other hand the crystal-field-splitting, which is responsible for the energy splitting $\Delta = E_n - E_0$, decreases the effect of the spin-orbit-coupling. The tendency of the crystal-field to suppress the spin-orbit-coupling is called orbital quenching. This is the reason why the deviations of $\hat{g}$ from g_e are relative small. In the first approximation equation (2.18) can be rewritten as follows:

$$g_{ii} = g_e - \alpha \frac{\lambda}{\Delta} \tag{2.19}$$

The coefficient α is a positive number with values between 1 and 10. Hence it is obvious that electron centers, which have a positive λ value, have a negative deviation from g_e. Hole centers, however, show a positive deviation from g_e because of their negative value of λ [1].

The symmetry of the g-tensor of course reflects the symmetry of the defect. After a transformation into a principal axis system it is given by:

$$\hat{g} = \begin{pmatrix} g_x & 0 & 0 \\ 0 & g_y & 0 \\ 0 & 0 & g_z \end{pmatrix} \tag{2.20}$$

Therefore the electron-Zeeman term of the spin-Hamilton operator appears as:

$$H_{EZ} = \mu_B \vec{B} \hat{g} \vec{S} = \mu_B \left(B_x g_x S_x + B_y g_y S_y + B_z g_z S_z \right) \tag{2.21}$$

For an axial g-tensor, where x and y direction are equivalent, directions parallel ($g_\parallel = g_z$) and perpendicular ($g_\perp = g_x = g_y$) to the direction of the magnetic field are introduced. The effective g-value g_{eff} is then defined as:

$$g_{eff} = \sqrt{g_\parallel^2 cos^2(\Phi) + g_\perp^2 sin^2(\Phi)} \tag{2.22}$$

Here ϕ is the angle between the magnetic field and the z-axis of $\hat{g}$ in the principal axis system.

2.1.4 Fine structure splitting

Since there are many paramagnetic systems with $S > 1/2$, like e.g. impurities due to transition metal-ions in semiconductors or insulators (e.g. Fe, Co, Mn, Cu, etc.), it is necessary to take into account the fine structure interaction occurring for spin systems with $S \geq 1$. There are two different physical effects contributing to the fine structure interaction: On the one hand, there is the effect of the crystal field on the electron spins due to the spin-orbit interaction. On the other hand, there is the dipole-dipole interaction between unpaired electrons of the defect. Both parts lead to the same mathematical formalism. Depending on the type of defect one or the other part is dominating. For instance, the spin-orbit coupling constant λ for C or Si is relatively small. That is why in diamond or SiC the dipole-dipole contribution to the fine structure term dominates. However, in II-VI semiconductors the effect of the crystal field is dominant due to a strong spin-orbit interaction [2].

As mentioned before a quadratic fine structure term ($\vec{S}\hat{D}\vec{S}$) in the spin Hamilton operator can only occur in a spin system with an effective spin $S \geq 1$. For a fine structure term of forth order (aS^4) an effective spin of $S \geq 2$ is required.

The quadratic fine structure term has the form of

$$H_{FS} = \vec{S}\hat{D}\vec{S} \tag{2.23}$$

with the fine structure tensor $\hat{D}$. By transformation into the principal axis system it becomes:

$$\hat{D} = \begin{pmatrix} D_{xx} & 0 & 0 \\ 0 & D_{yy} & 0 \\ 0 & 0 & D_{zz} \end{pmatrix} \tag{2.24}$$

The trace of $\hat{D}$ can be considered as zero, since a value unequal to zero would only lead to a uniform shift of all levels. Therefore the number of independent elements of $\hat{D}$ is reduced to two. These two parts are the parameters D and E, with which $\hat{D}$ appears as the following:

$$\hat{D} = \begin{pmatrix} -\frac{1}{3}D + E & 0 & 0 \\ 0 & -\frac{1}{3}D - E & 0 \\ 0 & 0 & +\frac{2}{3}D \end{pmatrix} = \begin{pmatrix} E & 0 & 0 \\ 0 & -E & 0 \\ 0 & 0 & D \end{pmatrix} - \frac{1}{3}D \begin{pmatrix} 1 & 0 & 0 \\ 0 & 1 & 0 \\ 0 & 0 & 1 \end{pmatrix} \tag{2.25}$$

That implies that the fine structure term of the spin Hamilton operator can be written as:

$$H_{FS} = \vec{S}\hat{D}\vec{S} = D\left[S_z^2 - \tfrac{1}{3}S(S+1)\right] + E\left[S_x^2 - S_y^2\right] \tag{2.26}$$

Where the relationship $S_x^2 + S_y^2 + S_z^2 = \vec{S}^2 = S(S+1)$ was used. From equation (2.26) it is evident that D is the axial symmetric part of the fine structure term and E describes the asymmetric part.

The axial symmetric part of the fine structure term D causes a uniform shift for all states with equal $|m_s|$, and therefore leads to a splitting into doublets (except for $m_s = 0$). This behavior is shown in Figure 2.4. It is evident that the fine structure interaction leads to a splitting of the energy levels even if there is no magnetic field applied. Hence the fine structure splitting is also known as zero field splitting.

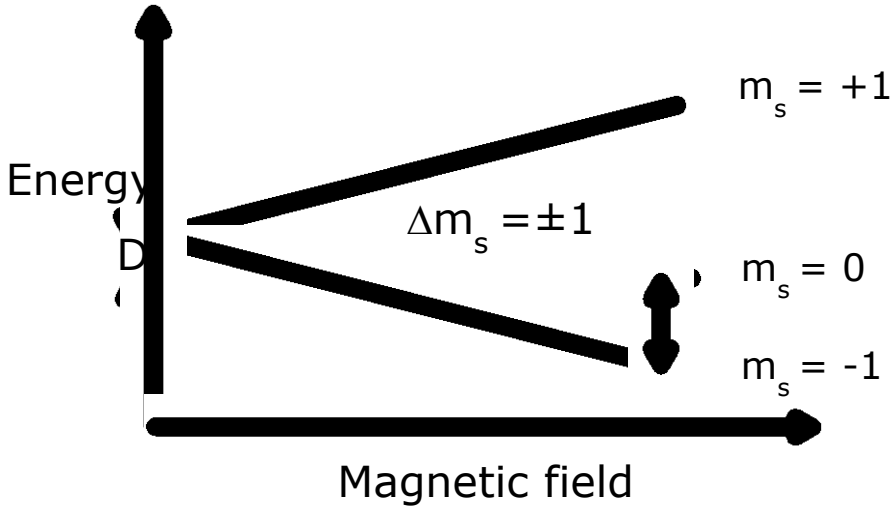

Figure 2.4: Schematic of the energy level splitting due to the isotropic Zeeman interaction and the fine structure interaction for a system with an electron spin of $S = 1$. The vertical arrows represent the allowed EPR transitions.

2.1.5 Hyperfine interactions

The interaction of unpaired electrons with the nuclear magnetic momentum of the central nucleus is referred to as hyperfine interaction. An interaction with one or more neighboring atoms is called superhyperfine interaction. In principle, they are described by the same spin-Hamilton term. The nuclear magnetic moment is described by the nuclear spin I, just as electron magnetic moments are described by the electron spin S. The nuclear magnetic spin quantizes along the magnetic field with the eigenvalues $m_I = I, I-1, \dots, -I+1, -I$. The mathematic description in form of an additional term to the spin-Hamilton operator is given by

$$H_{HF} = \vec{S}\hat{A}\vec{I} \tag{2.27}$$

with the electron spin $\vec{S}$, the nuclear spin $\vec{I}$, and the hyperfine coupling tensor $\hat{A}$, which can be split in to an isotropic part ($a\hat{1}$) and an anisotropic part $\hat{B}$. As a consequence of this, the hyperfine tensor can be written as

$$\hat{A} = a\hat{1} + \hat{B} \tag{2.28}$$

where $\hat{1}$ is the unit matrix. The scalar term a is the Fermi-contact term. The anisotropic hyperfine tensor $\hat{B}$ is traceless and can be described in its principal axis system by two anisotropic hyperfine interaction constants b and b' [7].

$$\hat{B} = \begin{pmatrix} -b + b' & 0 & 0 \\ 0 & -b - b' & 0 \\ 0 & 0 & 2b \end{pmatrix} \tag{2.29}$$

It follows that:

$$b = \frac{1}{2} B_{zz} \tag{2.30}$$

$$b' = \frac{1}{2}\left(B_{xx} - B_{yy}\right) \tag{2.31}$$

It is obvious that b' describes the deviation from the axial symmetry.

The Fermi-contact term describes the unpaired spin density at the nucleus site. Therefore it is obvious that for a defect in which the unpaired electron belongs to an s-orbital, a is non-vanishing, while it vanishes for all other orbitals, because their probability of presence at the nucleus is zero. The Fermi-contact term at a nucleus occupying the site r_l can be expressed as [3]:

$$a = \frac{2}{3} \mu_0 g_e \mu_B g_N \mu_N |\Psi(r_l)|^2 \tag{2.32}$$

$\Psi(r_l)$ is the wave function of the defect in the one-particle approximation. The elements of the anisotropic hyperfine tensor $\hat{B}$ are given by:

$$B_{ij} = \frac{\mu_0}{4\pi} \mu_B g_e g_N \mu_N \int \left(\frac{3x_i x_j}{r^5} - \frac{\delta_{ij}}{r^3} \right) |\Psi(r)|^2 dV \tag{2.33}$$

The anisotropic hyper fine constants b and b' reflect how the wave function decays radially. The different hyperfine interaction parameters are connected by the following equations [3]:

$$A_{\parallel} = a + B_{\parallel} = a + 2b \tag{2.34}$$

$$A_{\perp} = a + B_{\perp} = a - b \tag{2.35}$$

$$a = \frac{\left(A_{xx} + A_{yy} + A_{zz}\right)}{3} \tag{2.36}$$

Under the assumption of isotropic hyperfine and Zeeman interactions, and presuming $E_{HF} \ll E_{EZ}$, the energy eigenvalues of the Hamiltonian can be expressed as:

$$E = g\mu_B B m_s + a m_s m_i \tag{2.37}$$

Thereby m_s and m_I are the eigenvalues of $\vec{S}$ and $\vec{I}$ in magnetic field direction. It is obvious that the hyperfine interaction splits every single Zeeman level in m_I equidistant levels. Since in EPR there are no allowed transitions between different nuclear spin levels, the selection rules are $\Delta m_s = \pm 1$ and $\Delta m_I = 0$. However, also "forbidden" EPR transitions can be observed, which follow the selection rules $\Delta m_s = \pm 1$ and $\Delta m_I = \pm 1, \pm 2$.

This is why in EPR a splitting of the resonance line in $2I + 1$ hyperfine lines with a distance of $\Delta B = \frac{a}{g\mu_B}$ is observed. The hyperfine splitting for a system with S = ½ and I = ½ is shown in Figure 2.5.

The observation and analysis of the hyperfine splitting is the fundament of chemical identification in EPR. Consequently, if the hyperfine interaction can be observed in the EPR experiment it is possible to assign the defect to an element with a particular nuclear spin. The latter is then compared with values from the literature. Since there are only a few elements with the same nuclear spin this assignment is very accurate. Together with the isotope ratio, which is unique for each element, an unambiguous attribution is possible.

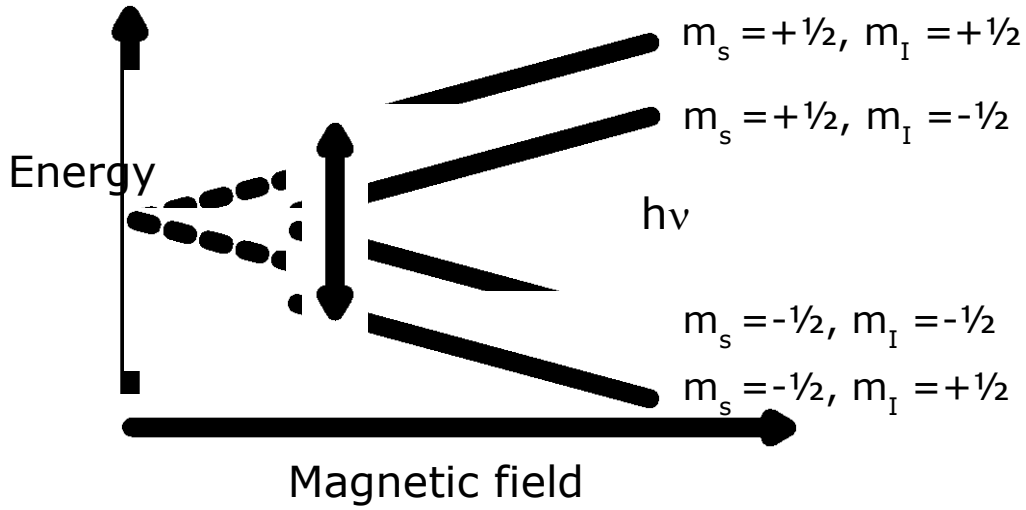

Figure 2.5: Schematic representation of the energy level splitting for a system with S=½ and I=½. The solid lines represent the energy levels split due to the hyperfine interaction and the dashed lines are the energy levels in absence of the a hyperfine interaction. Vertical arrows indicate the allowed EPR transitions.

2.1.6 Nuclear Zeeman interaction

Since a nuclear spin interacts with an applied magnetic field much like an electron does, there is also a corresponding contribution to the spin Hamiltonian. This effect is known as the nuclear Zeeman interaction.

$$H_{NZ} = -g_N \mu_N \vec{B}\vec{I} \tag{2.38}$$

Like an electron a nucleus possesses a g factor, but due to the lack of an equivalent to the orbital angular momentum of an electron g_N is isotropic. Its value can be obtained from the literature.

2.1.7 Nuclear quadrupole interaction

A nucleus with spin I ≥ ½ has an electric quadrupole moment which will interact with the electric field gradient at the nucleus site. These interactions can be described by the nuclear quadrupole tensor $\hat{P}$ and can be written in the following form:

$$H_{NQ} = \vec{I}\hat{P}\vec{I} \tag{2.39}$$

In its principal axis system the nuclear quadrupole tensor can be written as a traceless matrix:

$$\hat{P} = \begin{pmatrix} P_{xx} & 0 & 0 \\ 0 & P_{yy} & 0 \\ 0 & 0 & P_{zz} \end{pmatrix} = \begin{pmatrix} -K(1-\eta) & 0 & 0 \\ 0 & -K(1+\eta) & 0 \\ 0 & 0 & 2K \end{pmatrix} \tag{2.40}$$

K is the quadrupolar coupling constant. The relations between the diagonal parameters of $\hat{P}$ and the commonly used parameters e^2Qq/h and η are given by:

$$\frac{e^2Qq}{h} = 2I(2I-1)P_{zz} \tag{2.41}$$

e^2Qq/h is the largest component of the electric field gradient at the nucleus. η is an asymmetry parameter.

2.1.8 EPR transition probabilities

After all parts of the spin Hamiltonian necessary to describe EPR phenomena have been dealt with in the previous sections, in this chapter the probabilities and selection rules of EPR transitions will be discussed. There are two requirements to be fulfilled for EPR transitions: an external applied magnetic field to lift the degeneracy of the unpaired spin, and an oscillating magnetic field (i.e. the magnetic field component of a high frequency microwave) to induce the transitions between the Zeeman-splitting levels. This is shown in Figure 2.6, where N_+ and N_- are the occupation numbers of the spin states $|+1/2\rangle$ and $|-1/2\rangle$.

If the oscillating magnetic field is perpendicular to the applied magnetic field, the resulting field at the sample is given by:

$$\vec{B} = \begin{pmatrix} B_1 \cos \omega t \\ 0 \\ B_0 \end{pmatrix} \tag{2.42}$$

With the static magnetic field B_0, the oscillating magnetic field B_1, and the angular frequency of the oscillating magnetic field ω. Together with the spin Hamiltonian of the electron Zeeman energy as given by equation (2.21) we obtain [7]:

$$H = g\mu_B(B_0 S_z + B_1 S_x \cos\omega t) = \mathcal{H}_0 + \mathcal{H}_W \cos\omega t \tag{2.43}$$

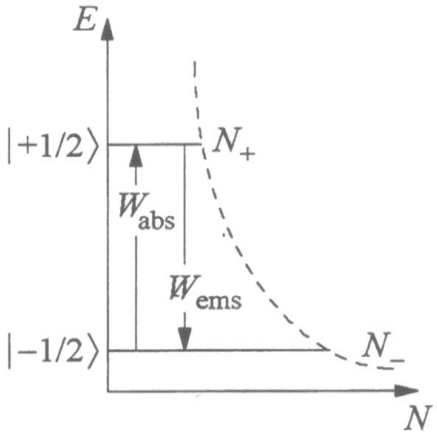

Figure 2.6: Occupation of the spin states in thermal equilibrium and microwave induced transitions between them.

To determine the transition probabilities between the $|+1/2\rangle$ (spin up) state and the $|-1/2\rangle$ (spin down) state one can use time dependent perturbation theory, as long as the oscillating magnetic field B_1 is much smaller than the static magnetic field B_0. This requirement is usually fulfilled for EPR and NMR spectroscopy. With "Fermi's Golden Rule" the transition probability is given by [7]:

$$W_{-1/2\leftrightarrow+1/2} = \frac{1}{4}\hbar^2 \left|\langle -1/2 \left|\mathcal{H}_W\right| +1/2\rangle\right|^2 g(\nu) \tag{2.44}$$

Where g(υ) is a form function. Note there are only transitions for the case that the oscillating magnetic field is perpendicular to the static magnetic field. If the oscillating magnetic field is parallel to the static magnetic field the transition probability is 0. For electrons the EPR transition probability can be written as [7]:

$$W_{EPR} = \frac{1}{4}\gamma_e^2 B_1^2 g(\nu) \tag{2.45}$$

The transition probabilities for absorption ($|-1/2\rangle \rightarrow |+1/2\rangle$) and stimulated emission ($|+1/2\rangle \rightarrow |-1/2\rangle$) are the same. The EPR transition selection rules are given by these applications of Fermi's golden rule. The eigenstates of the spin Hamilton operator may not only be the simple spin states, but also linear combinations of the spin states are possible. If such a behavior occurs so-called "forbidden" transitions can be observed.

Due to the fact that the EPR transition probabilities of the absorption process and the stimulated emission are the same, there has to be a difference in the populations N_+ and N_- of the spin states to allow an EPR transition. The easiest way to achieve a population difference is a change of the temperature, because the population numbers of the spin states in thermal equilibrium are given by the Boltzmann distribution:

$$\frac{N_+}{N_-} = exp\left(\frac{-h\nu}{k_B T}\right) \tag{2.46}$$

Due to the lower temperature the spin state with the lower energy N_- becomes more populated. Today the cooling methods of choice are the use of liquid helium (4 K) and liquid nitrogen (77 K). In the past liquid hydrogen (20 K) was also used for this purpose. At low temperatures one also has to take into account that the spin-lattice relaxation time increases. If the temperature is too low this would disrupt the population difference. The other value one has to adjust carefully is the microwave power. If it is too high the transition to the higher energy state would be induced faster than the electrons can relax to their ground state. Hence, it is necessary to find the optimal values for temperature and microwave power to maximize the EPR signal intensity.

2.2 EPR detected Photoionization (Photo-EPR)

A small drawback of EPR as described above is that it is not possible to gain any information on the energetic position of the defect in the band gap. However, in most cases it is possible to illuminate the sample with light of a defined wavelength to convert the defect into another charge level due to photoionization. This way one can observe EPR signals of defects that are normally not in a paramagnetic charge state.

Moreover, the change of the EPR signal intensity of the defect in dependence of the wavelength of the light can be detected. With this information the energy level position of the defect in the band gap can be determined [8].

There are two methods for photo-EPR measurements. First, there is the steady state method in which the equilibrium value of the EPR intensity is measured after a sufficiently long illumination time. In this case, the optical cross section of the photoionization can be determined from the dependence of the EPR signal intensity from the photon energy [8].

$$\sigma_{el}(E_{opt}, h\nu) \sim \frac{\sqrt{h\nu - E_{opt}}}{(h\nu)^3} \tag{2.47}$$

σ_{el} is the optical cross section. If one takes into account the electron-phonon interaction the formula appears as:

$$\sigma_0(h\nu) = \frac{1}{\sqrt{\pi}} \int_{-\beta}^{\infty} e^{-z^2} \sigma_{el}(E_{opt}) \left(1 + \frac{\Gamma}{h\nu}\right) dz \tag{2.48}$$

The parameter Γ describes the broadening of the photo transition absorption band at elevated temperatures.

$$\beta = \frac{h\nu - E_{opt}}{\Gamma} \tag{2.49}$$

$$\Gamma = \frac{\omega_0}{\omega_{ex}} \sqrt{2(E_{opt} - E_{th}) \hbar\omega_0 cth\left(\frac{\hbar\omega_0}{2k_B T}\right)} \tag{2.50}$$

The frequencies of the phonons coupled to the ground and excited states are given by ω_0 and ω_{ex}. The thermal and the optical ionization energy are connected by the lattice relaxation energy.

$$E_{rel} = E_{opt} - E_{th} \tag{2.51}$$

The second photo-EPR method is the initial slope method. Here, the time dependent variation of the EPR signal intensity after the light source is turned on is observed. From the slope of the signal increase it can be determined if one or more defects are involved in the photo transition. For a mono exponential slope only one defect is involved.

3 The nitrogen center in Zinc Oxide

3.1 Introduction

ZnO is a wide band gap semiconductor crystallizing in the wurtzite structure and has a direct band gap of 3.3 eV at room temperature. Together with the large exciton binding energy of 60 meV one of the most notably applications of ZnO is to use it for optoelectronic devices. But to use ZnO successful as an optoelectronic device material operating in the UV range n-type as well as p-type material is necessary. N-type doping in ZnO is already achieved with dopants like Ga, Al, In, H, Cl, F, or I substituting the respective cation or anion and forming shallow levels. In the case of p-type doping the situation looks different since ZnO shows like most wide band gap semiconductors an asymmetry in dopability [9]. Therefore it is difficult to achieve reliable and reproducible p-type doped ZnO. Since nitrogen acts as a shallow acceptor in other II-VI compounds [10] it was also considered as a suitable p-type dopant in ZnO [11]. Several groups reported the successful p-type doping of ZnO with nitrogen [12-14], but it remains still difficult as reported by Lee et al. [15].

This chapter deals with the characterization of the nitrogen acceptor in ZnO. Previous studies showed the existence of isolated nitrogen atoms substituting an oxygen atom (N_O) [16, 17] and molecular nitrogen $(N_2)^-$ [18], both are acceptors. From theoretical predictions and experimental data there are more and more hints that it should be a deep acceptor [16, 19-21]. However, the energy level position and hence the knowledge if it is a deep or a shallow acceptor is not finally clarified. This fact will be investigated in the following sections.

3.2 Experimental Results

A standard commercially available ZnO bulk crystal bought from Eagle Picher (Miami) was used for all the experiments described in this chapter. The crystal was grown by the method of seeded chemical vapor transport (CVT) (see Appendix A for more information on ZnO) and had a size of 7 mm x 3 mm x 1 mm. It was cut from a larger boule by the company.

In the as-grown state the crystal had a slightly yellow coloration and was an n-type conducting material with a carrier concentration of approximately 10^{17} cm^{-3} at room temperature as determined by Hall measurements. The crystal was irradiated with a beam of 3.8 MeV electrons from a van de Graaff electron accelerator at the University of Berlin in order to lower the position of the Fermi level. The current density was adjusted to 7.86 µA per cm^2 with a dose of 2.043 x 10^{18} electrons per cm^2. During the irradiation the temperature increased to 104 °C. From previous studies it is known that after a heat treatment or irradiation with electrons it is possible to observe nitrogen acceptors in ZnO in EPR measurements [16, 18]. Due to this treatment the conductivity is decreased significantly, but the crystal is still n-type conducting (about 10^{14} carriers per cubic centimeter, determined by Hall measurements). The color appears now a bit more yellow than in the as-grown state. By means of secondary ion mass spectroscopy (SIMS) measurements the nitrogen concentration was determined to (4±2)x10^{18} atoms per cm^3.

In order to gather more information on the nitrogen acceptor in ZnO the sample was investigated by photoluminescence spectroscopy, optical absorption spectroscopy and electron paramagnetic resonance spectroscopy. The results of these measurements are described in the following sections.

3.2.1 Photoluminescence measurements

For the photoluminescence spectroscopy a self-assembled setup was used. It consisted of an Omnichrome 3074 HeCd-Laser with a 325 nm line, an Oxford Helium bath cryostat with a temperature regime from 1.5 to 300 K and a Jobin-Yvon monochromator.

In Figure 3.1 a photoluminescence overview spectrum of the electron irradiated Eagle Picher ZnO sample is shown. The measurement was performed at 4 K with a 325 nm laser line for excitation. The first thing one can see on the low energy side of the spectrum is a broad unstructured band at 2.45 eV, which can in principal be explained by at least three models. The first model attributes it to Cu impurities in the sample [22]. This can be excluded in the present case, because the pronounced phonon

structure could not be observed. According to the second model, the low energy PL band originates from a shallow donor (D^0) to oxygen vacancy (V_O^0) recombination [23, 24]. The third model explains the feature by an internal triplet recombination of the neutral oxygen vacancy (S=1), similar to color center emissions in ionic crystals [25]. For the last model there is also an alternative interpretation of the defect model from Janotti et al. [20], in which the spin triplet (S=1) recombination is assigned to a singly negatively charged Zn vacancy (S=½) and a neutral shallow donor (S=½), which by exchange interaction form a pair defect in the S=1 state. Based on the experimental data only the first model can be ruled out and there are no hints at which defect causes the green emission in this sample. Hence, the low energy PL band could be caused by the defect described in the second or the third model or by a superposition of both of them.

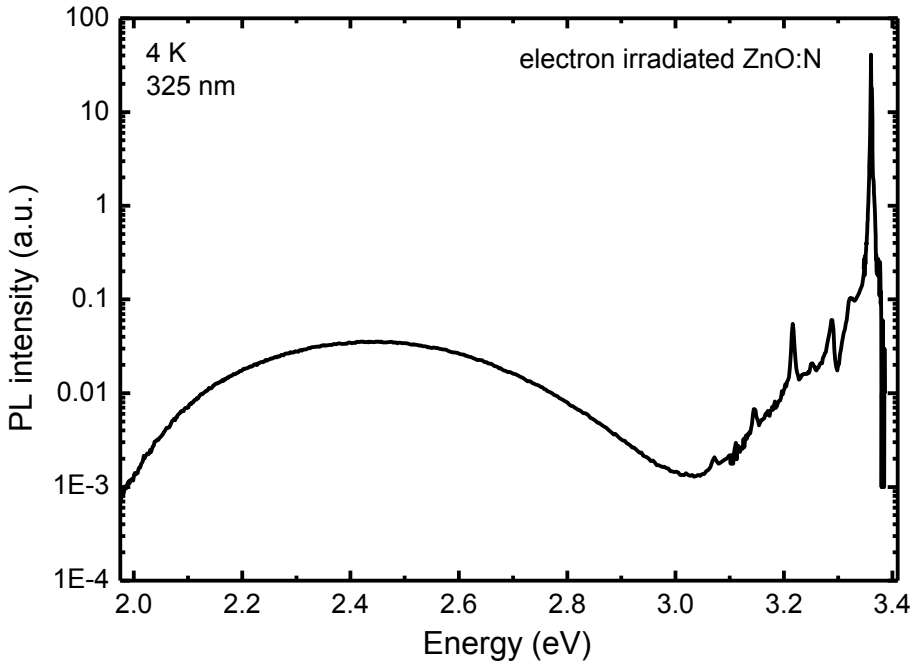

Figure 3.1: Photoluminescence overview spectrum of the electron irradiated Eagle Picher ZnO sample at 4 K illuminated with a 325 nm laser.

The high energy part of the spectrum is dominated by bound exciton recombinations and the corresponding longitudinal optical (LO) phonon replicas with an energy

separation of 72 meV. The observed shape of the spectrum in this part is common for ZnO bulk crystals [26]. A detailed spectrum of the excitonic region is depicted in Figure 3.2. Signals from at least three bound excitons can be observed and assigned to their corresponding defects. I_4 at 3.3628 eV assigned to hydrogen, at 3.3608 eV the I_6 peak attributed to aluminum and the I_7 peak at 3.36 eV with no assignment at present [27]. However, no evidences for a nitrogen acceptor, like e.g. a donor acceptor pair recombination (DAP) signal, were observed in the photoluminescence measurements. This could be due to the fact that n-type conductivity is still dominating in the sample or that the nitrogen concentration is too low to show up DAP's in photoluminescence measurements.

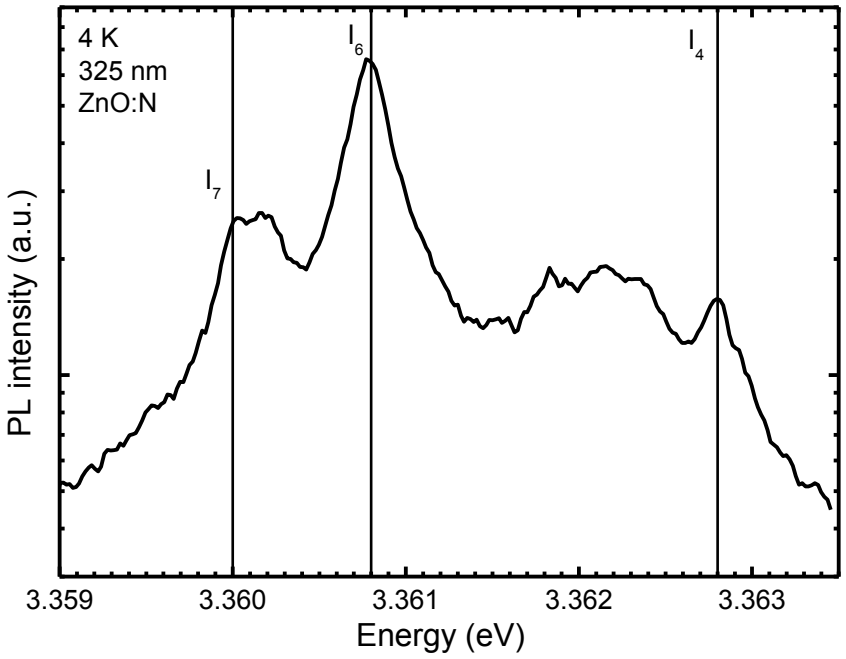

Figure 3.2: Detailed PL spectrum of the electron irradiated Eagle Picher ZnO sample at 4 K illuminated with a 325 nm laser. One can see the excitonic region with the I_4, I_6 and I_7 lines.

3.2.2 Electron Paramagnetic Resonance

All the EPR measurements are performed with a Bruker EPR spectrometer, which is described in the appendix. The EPR spectra of the sample before the electron irradiation look very similar to the most other ZnO bulk crystals. The only significant signal one can observe is a shallow donor signal at g = 1.96 which dominates the whole spectrum. Figure 3.3 shows the EPR spectra of the sample after the electron irradiation at 4 K. Therefore the sample was cooled down to 4 K in the dark to avoid any illumination effects due to ambient light. In Figure 3.3 (a) the EPR spectrum without illumination is shown, the only observable signal at 3467 G can be assigned to a shallow donor in ZnO with a g-value of g = 1.96 [26]. Compared to the EPR spectrum before the electron irradiation the intensity of the shallow donor signal has decreased significant. Due to the electron irradiation the position of the Fermi level has shifted towards lower energies and therefore less shallow donor states are occupied by an electron which leads to the decrease of the EPR intensity. After the sample was exposed to UV light 3 lines with different peak-to-peak amplitudes appear (see Figure 3.3 (b)). A mercury vapor lamp was used as illumination source in this case. These EPR signals were observed earlier by Carlos et al. [17] and Garces et al. [16] and are attributed to a neutral nitrogen atom substituting an oxygen atom in ZnO. However, the intensity of the shallow donor EPR signal doesn’t change. All the EPR spectra are measured at very low microwave powers, due to fast appearing saturation effects. The saturation behavior of the sample is discussed later in this chapter.

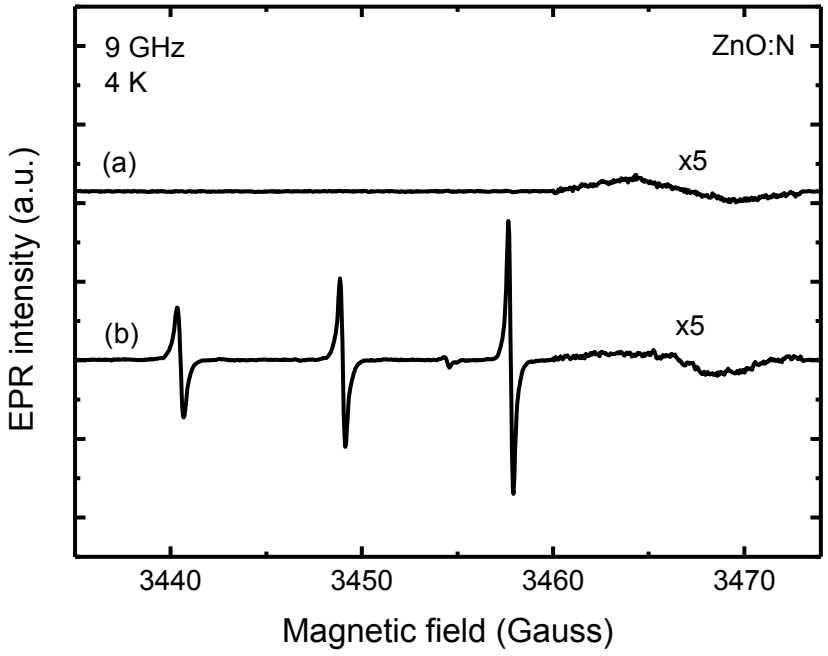

Figure 3.3: EPR spectra of the nitrogen center and a shallow donor in ZnO taken at 4 K without (a) and with UV light illumination (b). The shallow donor signal intensity was multiplied by 5.

In Figure 3.4 a detailed spectrum of the nitrogen center is shown. The EPR signal of the shallow donor is also visible in this spectrum approximately at 3467 G. One can clearly observe the 3 lines of the nitrogen center with the nuclear spin I = 1 (99.6 % abundance) at 3442 G (N1), 3447 G (N2), and 3452.5 G (N3). These signals represent the allowed EPR transitions with the selection rules $\Delta m_S = \pm 1$ and $\Delta m_I = 0$. It appears that the 3 lines have a different EPR signal intensity, they differ in line width ΔB and peak-to-peak intensity ΔI. But the signal with the smallest peak-to-peak intensity has the biggest line width and since the EPR intensity is given by $I_{EPR} \sim \Delta I \cdot \Delta B^2$ all the lines have the same EPR intensity.

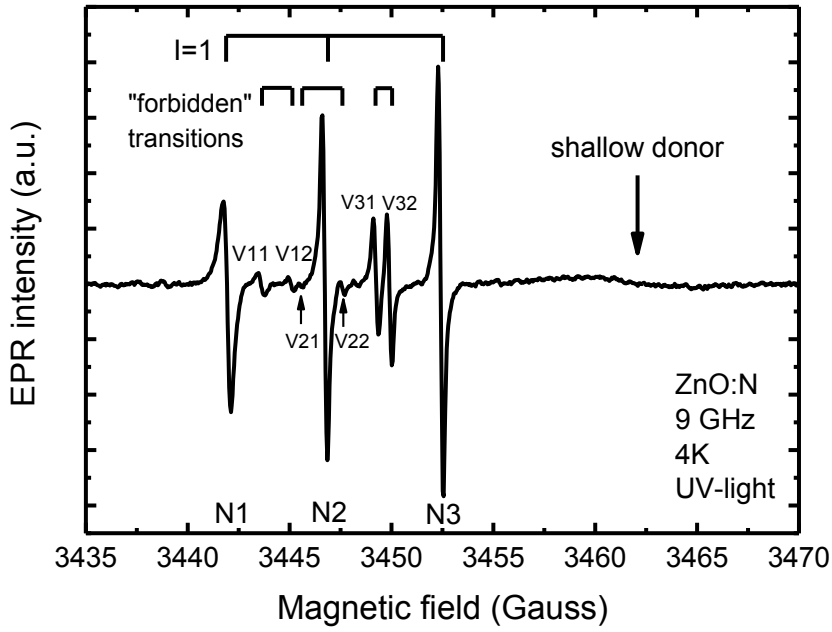

Figure 3.4: Detailed EPR spectrum of the neutral nitrogen center in ZnO recorded at 4 K after illumination with UV light. The allowed hyperfine transitions are marked N1, N2, and N3, whereas the "forbidden" transitions are marked as V11, V12, V21, V22, V31, and V32.

For the EPR measurement shown in Figure 3.4 the angle of the c-axis of the crystal was rotated 80° away from c||B to observe the EPR signals marked with V11, V12, V21, V22, V31, and V32. They are due to "forbidden" EPR transitions not following the selection rules stated above. For paramagnetic ions with a hyperfine structure and a more than doubly degenerate ground state, which is split by the crystalline electric field by amounts of 10^{-2} to 10^{-1} cm^{-1}, "forbidden" hyperfine lines can be observed which are due to transitions in which the nuclear magnetic quantum m_I changes by ±1 and ±2 [2]. They appear when the magnetic field is at an angle between the parallel and perpendicular orientation toward the crystal axis. These transitions are caused by second-order effects due to cross terms in the spin Hamiltonian between the fine structure splitting and the hyperfine structure splitting. All allowed and forbidden transitions for the neutral nitrogen center in ZnO are shown in Figure 3.5. The allowed

hyperfine transitions with $\Delta m_I = 0$ are represented by the solid arrows, the "forbidden" hyperfine transitions with $\Delta m_I = \pm 1$ are depicted by the dashed arrows and the ones with $\Delta m_I = \pm 2$ are shown by the dotted arrows. Above the energy level diagram a schematic EPR spectrum with all transitions is shown from which we can assign V11, V12, V31, and V32 to the $\Delta m_I = \pm 1$ transitions and V21 and V22 to the $\Delta m_I = \pm 2$ transitions.

The complete spin Hamiltonian to describe all the effects mentioned above is given by:

$$H = \mu_B \vec{B} \hat{g} \vec{S} + \vec{S} \hat{A} \vec{I} + \vec{I} \hat{P} \vec{I} - g_N \mu_N \vec{B} \vec{I} \qquad (3.1)$$

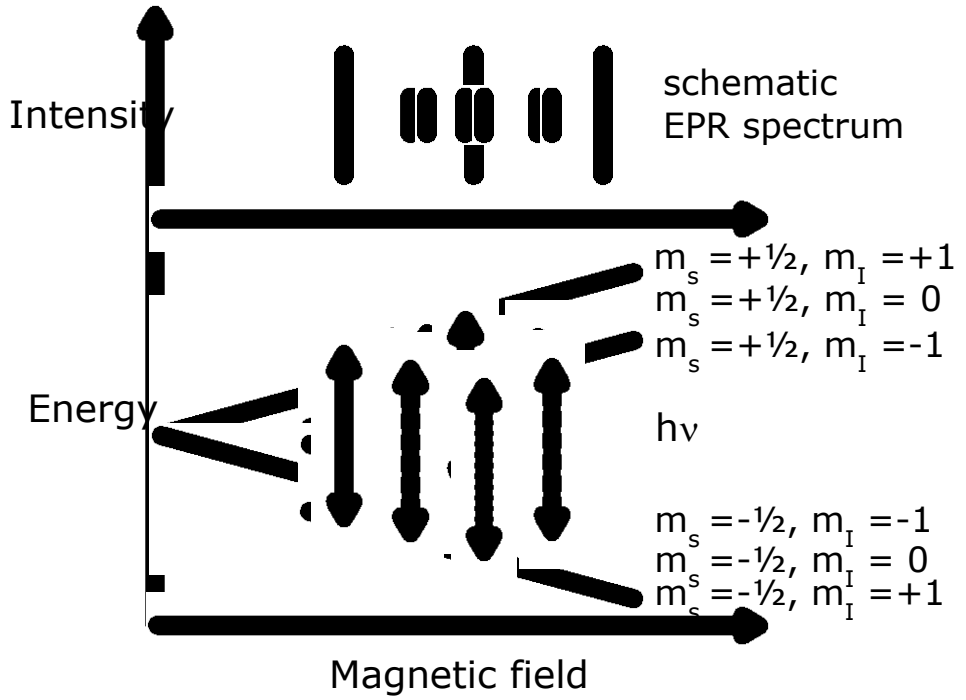

Figure 3.5: Energy level splitting due to the hyperfine interaction for a system with S = ½ and I = 1 with all allowed (solid arrows) and "forbidden" (dashed and dotted arrows) hyperfine transitions. Above a schematic EPR spectrum for this system is shown.

The values of the interaction parameters can be determined by angular dependent measurements. The results of these measurements are shown in the following sections.

The angular dependent behavior of all the nitrogen EPR signals is shown in Figure 3.6, 0° represents here c⊥B and 90° is c||B. The EPR signal intensity is also angular dependent. One can see that the "forbidden" transitions are only observable if the c-axis of the crystal is at least 60° rotated away from the direction of the magnetic field. For the orientations near c||B the intensity is too small.

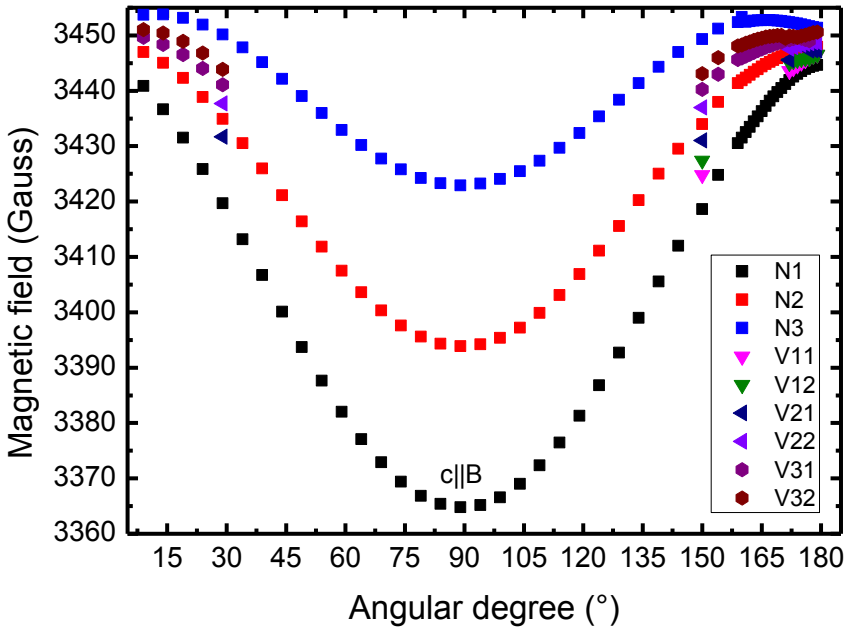

Figure 3.6: Angular dependent behavior for all EPR lines of the nitrogen center recorded at 4 K after the illumination with UV light.

The angular dependence of the hyperfine coupling constant A recorded at 4 K after the illumination of the sample with UV light is shown in Figure 3.7 together with the magnetic field position of the central nitrogen line. From these measurements the values of A are determined to $A_{\perp} = 8.9\,MHz$ and $A_{\parallel} = 81.1\,MHz$, as well as $g_{\perp} = 1.963$ and $g_{\parallel} = 1.995$. They are in quite good agreement with previous studies [16] and theoretical calculations [19]. With equations (2.34) to (2.36) the isotropic part $a = 33\,MHz$ and the anisotropic part $b = 24\,MHz$ of the hyperfine coupling constant can be calculated. From these values one can calculate the contribution of the nitrogen 2s and 2p electron orbitals to the electron spin density at the nucleus. The atomic

parameters for the comparison to isolated atoms are given by Morton and Preston [28]. The isotropic hyperfine interaction parameter $a = 33\ MHz$ is compared to 1811 MHz which yields a contribution of 0.02 for the $^{14}N(2s)$ orbital. For the contribution of the $^{14}N(2p)$ orbital the anisotropic hyperfine interaction parameter $b = 24\ MHz$ is compared to 55.5 MHz, resulting in a contribution of 0.42. These values yield a 95 % p-orbital contribution for electron spin density at the nucleus of nitrogen in ZnO. The values of a and b could change, due to the fact that it is not possible to determine the signs of the hyperfine interaction parameters from EPR measurements alone. Gallino et al. [19] calculated 97 % for the p-orbital contribution using a negative sign for $A_{\perp}$ an a positive sign for $A_{\parallel}$. The relative signs of the hyperfine interaction parameters were in this case determined by HYSCORE measurements. Using the same relative signs as given by Gallino et al. would yield also 97 % p-orbital contribution for the present study. Anyway, the main statement of the analysis of the nitrogen hyperfine parameters is the fact that the electron is located in the p-orbital.

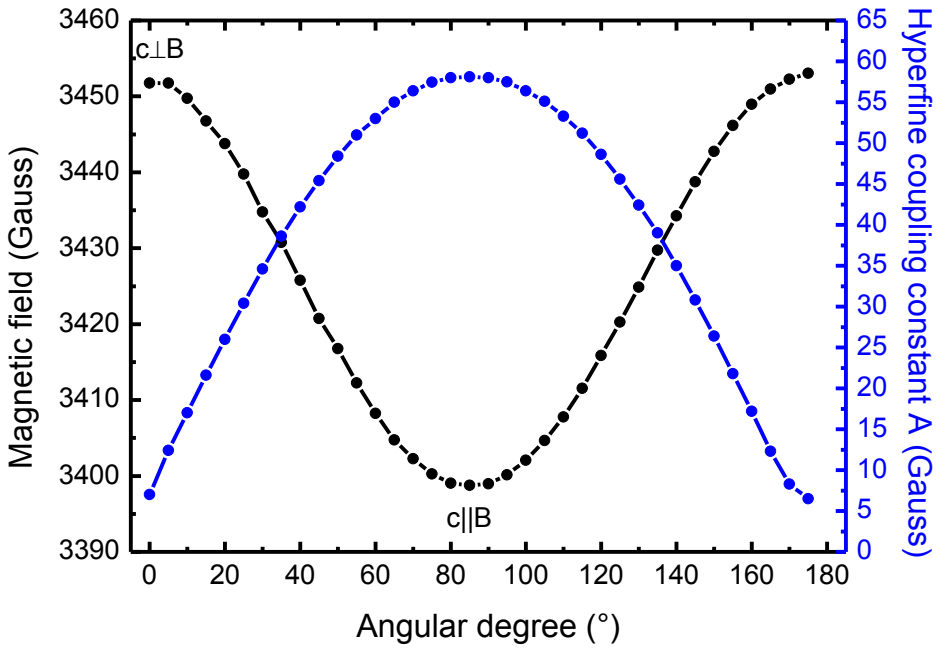

Figure 3.7: Angular dependence of the central nitrogen line (black circles) and the hyperfine coupling constant A (blue circles). The measurements were carried out at 4 K after the illumination with UV light.

The sample was also mounted in a different position on the sample holder to perform EPR measurements rotating it around the c-axis of the crystal. The EPR spectrum at 4 K shows after the illumination with UV-light the 3 lines of the I = 1 nitrogen center in ZnO (see inset of Figure 3.8). One can also observe the "forbidden" transitions in between the hyperfine lines. The angular dependence of the sample rotating it around the c-axis is displayed in Figure 3.8, it reveals an isotropic signal with a g-value of g = 1.966 and a hyperfine coupling constant of A = 10.2 MHz. These values are very similar to the parameters obtained from the measurements with the c-axis of the crystal perpendicular to the magnetic field direction. That implies that the defect is aligned along the c-axis of the crystal.

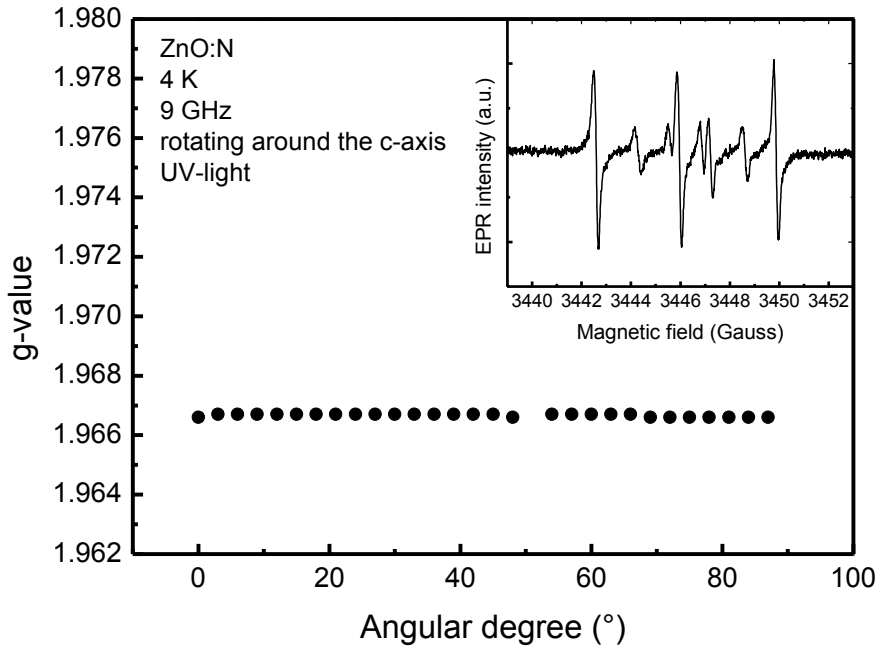

Figure 3.8: Angular dependence of the nitrogen center in ZnO rotating the sample around the c-axis of the crystal measured at 4 K after the illumination with UV light. In the inset the EPR spectrum is shown.

Together with the data from the angular dependent measurements not rotating around the c-axis it is possible to obtain the asymmetry parameter $\eta = 0.02$ and the quadrupolar coupling constant $K = -1.94\,MHz$. With these values e^2qQ/h can be calculated to 7.8 MHz. The very low asymmetry parameter gives a further hint that the defect is orientated along the c-axis of the crystal.

Since the sample saturates very fast with increasing microwave power it is interesting to record microwave power dependent EPR measurements. From these data it is also possible to gather more information on the relaxation behavior of the defect. The measurements were carried out at 4 K after the illumination with UV light. In Figure 3.9 the peak-to-peak amplitude of the EPR signal is plotted against the square root of the microwave power. For low microwave powers there is a linear behavior between the peak-to-peak amplitude and the square root of the microwave power, this is indicated in the plot by a dashed blue line. The maximal peak-to-peak amplitude is reached for a microwave power of 64 µW. From the microwave power dependent saturation behavior of the EPR signal it is possible to calculate the spin-lattice relaxation time T_1 and the spin-spin relaxation time T_2. To do this one has first to calculate the amplitude $B_1$of the magnetic field component of the electromagnetic field of the microwave. The connection to the microwave power is given by [29]:

$$B_1{}^2 = 2 \cdot 10^{-3} Q_L P \tag{3.2}$$

With the microwave power P and the quality factor Q_L of the microwave cavity.

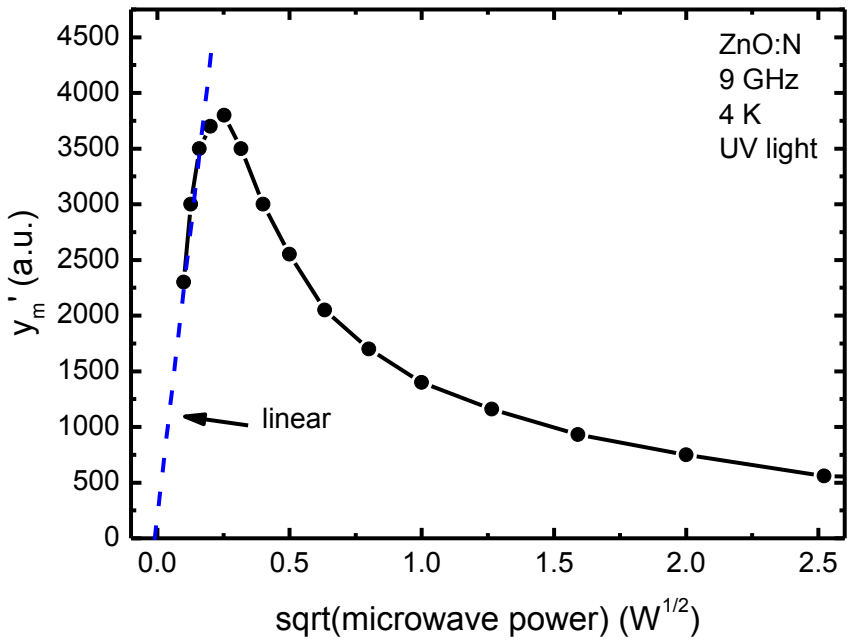

Figure 3.9: The peak-to-peak amplitude y_m' of the nitrogen center in ZnO is plotted as a function of the square root of the microwave power P. The measurements were taken at 4 K after the illumination with UV light.

The quality factor depends on the geometry of the cavity and the microwave absorption of the sample and the sample holder [4]. Also the peak-to-peak line width ΔH_{pp} of the EPR signal has to be determined. The unsaturated value ΔH_{pp}^0 of the peak-to-peak line width is given by:

$$\Delta H_{pp}^0 = \lim_{B_1 \to 0} \Delta H_{pp} \tag{3.3}$$

With these parameters the relaxation times can be estimated as the following [4]:

$$T_1 = 1.97 \cdot 10^{-7} \frac{\Delta H_{pp}^0}{g B_1^2} \tag{3.4}$$

$$T_2 = \frac{1.3 \cdot 10^{-7}}{g \Delta H_{pp}^0} \tag{3.5}$$

This yield for the nitrogen center a spin-spin relaxation time $T_2 = 3.4 \cdot 10^{-7}\ s$. For the spin-lattice relaxation time one obtains $T_1 = 1.2 \cdot 10^{-4}\ s$. The nitrogen center is after it

is converted into its paramagnetic charge state stable up to several hours, this behavior is also observed by Tarun et al. [21] and theoretically predicted by Lyons et al. [30]. One cannot draw conclusions whether the latter behavior depends on the relaxation times, since there are no other results to compare with available. However, it would be interesting to study the relaxation times for nitrogen acceptors in ZnO for thin films and nanoparticles.

To determine the temperature dependence of the EPR signal the sample was cooled down in the dark to 4 K and then illuminated with UV light to create the defect. Before the first measurement the UV light was turned off. This was done to be sure that the decrease of the EPR signal due to a temperature increase was not overlaid by the charging effect of the UV light. The first measurement was carried out at 4 K, for the second measurement the sample was heated up to 10 K and the measurement than was taken again at 4 K. This procedure was repeated up to RT. The results are shown in Figure 3.10, where the EPR intensity is plotted against 1000/T. In the inset the representative spectra for 4 K and 200 K are depicted. With increasing temperature the intensity of the EPR signal is decreasing. Compared to the EPR temperature dependence of a shallow defect, the effect of the signal degradation is very small (only a factor of 3), which indicates a high thermal stability of the center. This behavior gives a further hint for the deep acceptor nature of the N_O center in ZnO. Since it was not possible to observe the neutral nitrogen EPR signal at measurements with temperatures higher than 15 K, a calculation of the thermal activation energy could also not be done. For the same reason the temperature dependency of the relaxation times could not be determined.

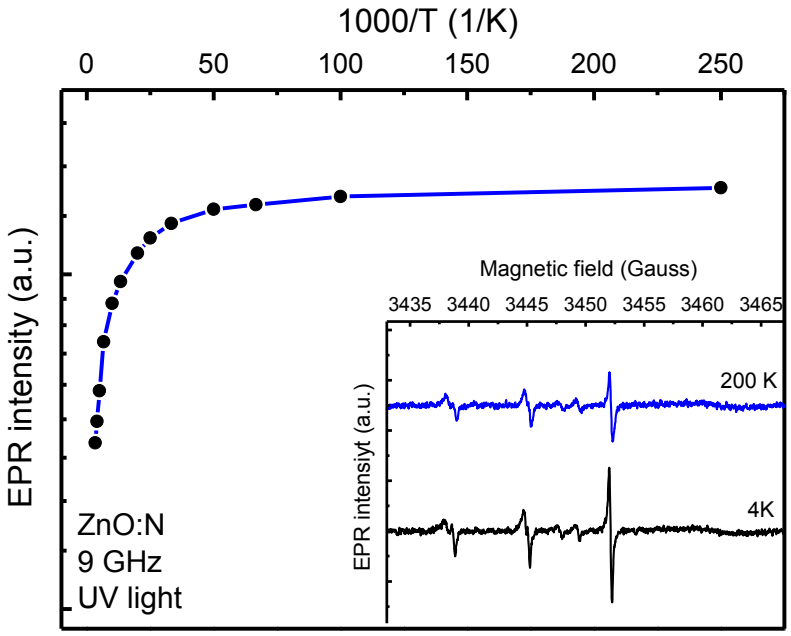

Figure 3.10: The logarithmic EPR intensity of the nitrogen center in ZnO is plotted versus 1000/T. In the inset the spectra recorded at 4 and 200 K are shown.

To gain more information on the properties of the defect it is also valuable to study the wavelength dependence of the creation of the paramagnetic nitrogen EPR-signal. A xenon arc lamp together with bandpass filters was used to for the illumination of the sample. To be sure that the intensity of the light on the microwave cavity was constant grey filters were used.

For each of the measurements for a specific wavelength the sample was cooled down from room temperature to 4 K in the dark to have the same initial state for each data point. This was necessary to avoid photo induced effects from previous measurements. The threshold wavelength to charge the defect into its paramagnetic state was 610 nm. Figure 3.11 shows the intensity of the EPR signal plotted against the energy of the incident light. But before one can do calculations with these data, one has also to take into account that the absorption of the sample at 4 K is also wavelength dependent and therefore the EPR intensity has to be corrected. A simple model to do this is given by

Godlewski [8]. Since the EPR intensity is proportional to the square root of the light intensity the correction factor is $\sqrt{1-exp(-\alpha d)}$. The values of αd were obtained earlier by optical absorption measurements (see Figure 3.15). To determine the ionization parameters of the photo transitions the data of Figure 3.11 were fitted by equation (2.48). The optical ionization energy is determined to $E_{opt} = 2.11\ eV$ and the broadening parameter to $\Gamma = 0.22\ eV$. From theoretical predictions a value of 2.4 eV is calculated for the optical ionization energy [30].

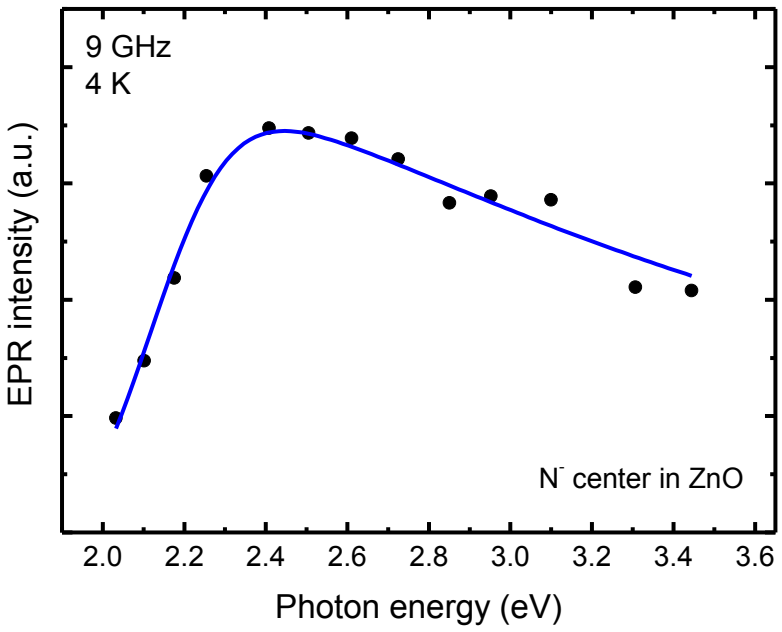

Figure 3.11: Energy dependence of the EPR intensity of the nitrogen center in ZnO measured at 4 K. The solid blue line represents a fit of the optical cross section with equation (2.48).

The next step is to derive the thermal ionization energy of the defect which is connected to the thermal ionization energy by $E_{opt} - E_{th} = E_{rel}$. At a first glance the temperature dependence of $\Gamma(T)$ is the method of choice to determine E_{th}, but one should keep in mind that the amplitude and kinetics of light induced EPR signals depend heavily on the rates of different capture processes. And due to the fact that capture processes change with the temperature it is very difficult to obtain reliable

values of E_{th} by this approach. However in the case of small or moderate lattice relaxations which is granted in our case, the thermal ionization energy can be estimated from the edge of the photo excitation process of the EPR signal [8]. So the thermal ionization energy can be estimated to $E_{th} = 2\ eV$ which results in a lattice relaxation energy of $E_{rel} = 0.11\ eV$.

Now that the energy level position of the $(N_o)^{0/-}$ charge state has been appointed to be 2.1 eV below the conduction band edge, the energy level position respective to the valence band edge has to be determined. To achieve this, an EPR experiment at 4 K was performed in which the sample was illuminated constant with 325 nm light from a high pressure mercury lamp with a bandpass filter. Simultaneously infrared light (980-660 nm) from a laser diode was coupled into the sample to lift an electron from the valence band to the defect. The EPR spectrometer setup was changed to the time-sweep mode in which the EPR signal intensity was recorded as a function of time at a fixed magnetic field value. When the light has enough energy to lift an electron from the valence band to the defect level the EPR signal should quench. Unfortunately it was not possible to observe such quenching of the EPR signal. There are various options why that have happened; the capture cross section for the photo transition from the valence band to the defect could be much smaller than for the transition to the conduction band. In this case the power of the laser diodes was too low to compensate the effects of the capture cross section. The calculation of the electron spin density contributions of the nitrogen 2s and 2p orbitals from the hyperfine interaction parameters reveals that there is only a vanishing small contribution of the 2s orbital. Thus the 2p orbital dominates the contribution to the electron spin density. Since the ZnO valence band has also p character, due to the oxygen p orbitals, a transition from the valence band to the defect is parity forbidden. Therefore the capture cross section is vanishingly small and it is not possible to quench the (N_O) EPR signal.

With the time-sweep measurement mode of the EPR spectrometer the time dependence of the EPR intensity of the nitrogen EPR signal labeled N3 was tracked in Figure 3.12, the measurement was taken at 4 K. The arrow indicates the time when the UV light lamp was turned on to illuminate the sample. From this moment the EPR intensity

increases until it reaches its maximum and stays at a constant value. This exponential behavior was fitted using the equation:

$$I_{EPR} = A \cdot e^{-\frac{t}{T_1}} + I_0 \tag{3.6}$$

From this fit the time constant of the creation process was determined to $T_1 = 0.4\ s$.

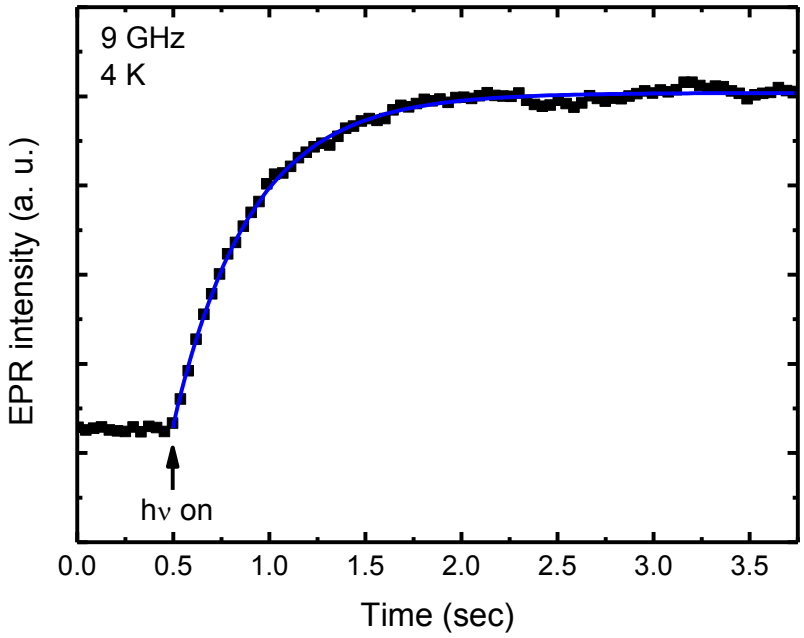

Figure 3.12: Time dependence of the intensity of the EPR signal labeled N3 after the light source is switched on. The blue line indicates a fit with a mono-exponential behavior.

As the fitting equation suggests the growing behavior of the EPR intensity is mono-exponential. This indicates that only one process is involved in this photo-transition. One electron from the nitrogen center is lifted directly into the conduction band (see below).

The mono-exponential behavior can be seen directly if the saturation value of the photo-EPR signal minus the photo-EPR signal $ln(I_\infty - I)$ is plotted as a function of the time. In this case the data points can be described by a linear slope (see Figure 3.13).

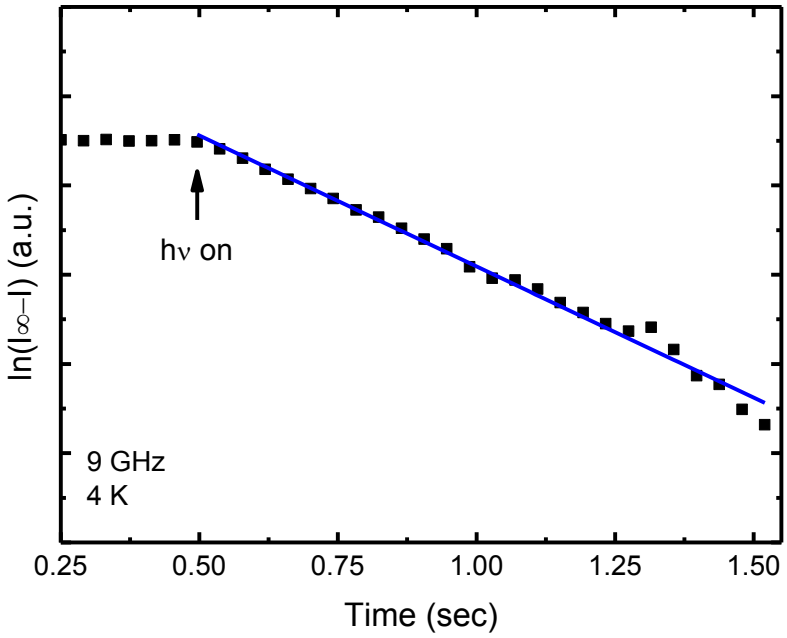

Figure 3.13: Time dependence of the ZnO (N_O) acceptor EPR signal intensity after switching on the light source. The linear slope indicates a monoexponential behavior.

With all the data gathered during the EPR measurements it is possible to draw an energy level diagram of the nitrogen acceptor in ZnO (Figure 3.14). The $(N_O)^{0/-}$ charge state of the nitrogen atom substituting an oxygen atom in ZnO is located 2.1 eV below the conduction band edge, which is known from the photo EPR measurements. The recombination path for the charging of the N_O center from its negative into the neutral charge state is shown with the blue lines in Figure 3.13.

$$N_O{}^- + h\nu \rightarrow N_O{}^0 + e^-$$

The electron lifted up into the conduction band can then be localized in a shallow donor.

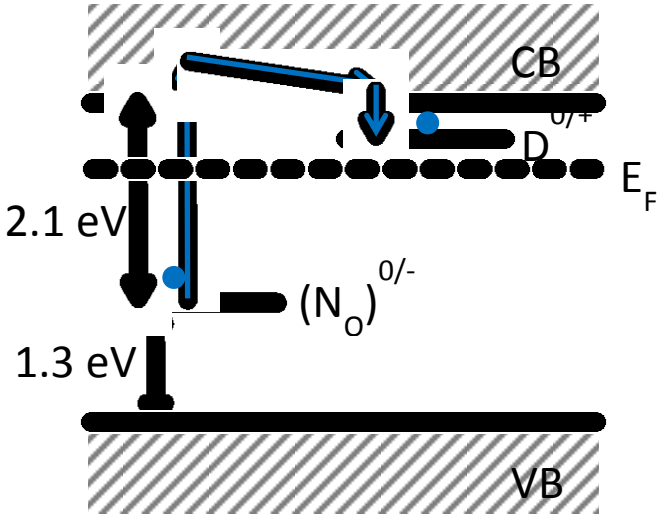

Figure 3.14: Energy level diagram of the N_O acceptor in ZnO. The blue arrows indicate the recombination path of the EPR signal creation.

The energy position of the defect respectively to the valence band could not be determined by EPR measurements due to the fact, that it was not possible to elevate an electron from the valence band to the defect level. However, the optical ionization energy of the $(N_O)^{0/-}$ defect level and the optical band gap of the ZnO sample is known, therefore one can estimate the energy level position of the defect to be 1.3 eV above the valence band.

3.2.3 Optical absorption spectroscopy

For the optical absorption spectroscopy measurements a Perkin Elmer Lambda 900 spectrometer was used together with an Oxford helium flow cryostat to adjust the temperatures from 4 K up to room temperature. There are no special features to observe in the transmission spectra of the sample. One can track the band gap from room temperature down to 4 K.

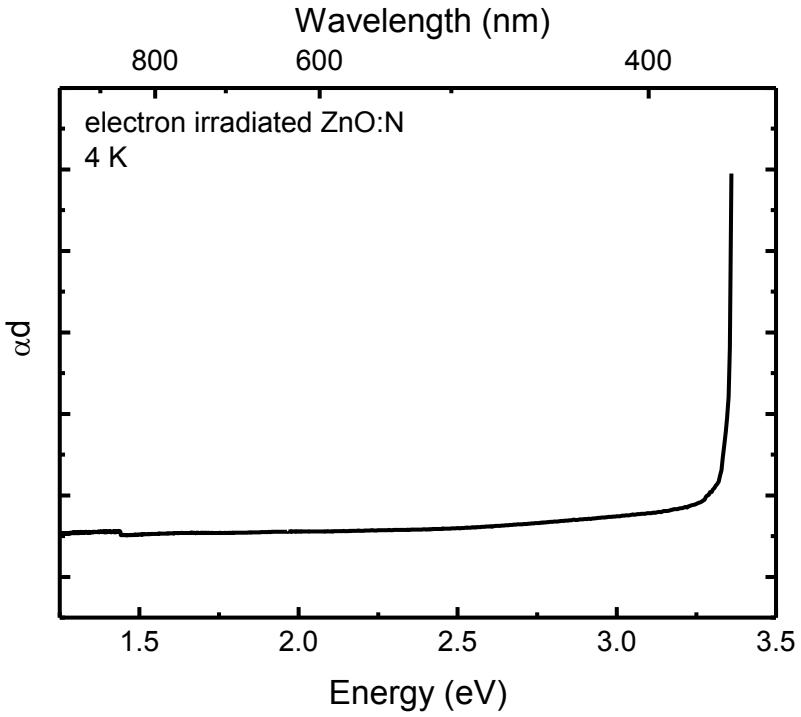

Figure 3.15: Optical absorption spectrum of the electron irradiated Eagle Picher ZnO sample at a temperature of 4 K.

These measurements were performed from room temperature down to 4 K in order to derive the dependence of αd from the energy. These values were necessary for the corrections of the photo-EPR measurements to calculate the optical ionization energy of the nitrogen acceptor in ZnO, which was done before in this chapter. Figure 3.15 shows αd in dependence of the energy at a temperature of 4 K.

3.3 Discussion

The neutral nitrogen acceptor (N_O) in ZnO could be observed with EPR measurements after the sample was electron irradiated. With this treatment the position of the Fermi level could be lowered, which leads to a decreased number of occupied shallow donors. That the number of shallow donors was reduced by the electron irradiation was proved by EPR. The neutral nitrogen acceptor shows up at low temperatures in EPR after the illumination with UV light. Due to the illumination the defect is charged from

its single negative charge state into the neutral charge state. The parameters of the g-tensor are in good agreement with the ones known from literature [16]. The analysis of the angular dependence reveals nearly the same hyperfine parameters Garces et al. [16, 18] and Gallino et al. [19] have shown in their works. However, there are some deviations for the quadrupole interactions parameters compared to the theoretical calculations and the experimental data of Gallino et al. [19]. The values for the quadrupolar coupling constant and the asymmetry parameter measured in this work are closer to the theoretical predictions than the experimental data from the other groups, especially the asymmetry parameter, which is nearly zero. From the angular dependent measurements rotating around the c-axis of the crystal and the asymmetry parameter of 0.023 it is obvious that the defect has to be aligned along the c-axis of the crystal. This is again in coincidence with the theoretical predictions, which predict no asymmetry at all.

With the wavelength dependent photo-EPR measurements the energy level position of the $(N_O)^{0/-}$ level could be determined to be 2.1 eV below the conduction band. This value is close to the calculated value of 2.4 eV from Lyons et al. [30]. For the thermal ionization energy a value of 2 eV can be estimated from the data, which leads to a lattice relaxation energy of 0.1 eV. Here the theory predicts a somewhat larger value of 0.3 eV [30]. The time dependent EPR measurements of the photo transition show a monoexponential behavior, therefore only one process is involved in the photo transition from the defect level to the conduction band. This process happens on a small time scale of 0.4 seconds.

The photoluminescence measurements give evidence for donator acceptor pair recombination (DAP) which would be a sign for a shallow acceptor level. The transitions from such a defect would be located in the broad unstructured PL band centered at 2.45 eV. Thus there is a further support of the deep acceptor state model.

4 Defects in Aluminum Nitride

4.1 Introduction

Aluminum Nitride (AlN) is a direct band gap semiconducting material. It crystallizes in the wurtzite structure and has an energy gap of approximately 6 eV. Alone it is an interesting material for optoelectronic devices operating in the UV range and as substrate material for epitaxy of group-III nitrides. But together with the wurtzite polytypes of InN and GaN it can form a continuous alloy system with a direct band gap ranging from 0.7 eV (InN) up to 6 eV (AlN) (see Appendix) [31]. Thus, these materials could potentially be used for the fabrication of optical devices that are active in a wavelength regime from the infrared to the UV range.

State of the art AlN in most cases shows a yellow coloration due to intrinsic and extrinsic defects. Due to these defects n-type AlN has a high resistivity caused by compensation effects, which is a big drawback for its use in optoelectronic devices. This chapter deals with the characterization of defects in AlN in order to assign them to chemical elements and thereby help to optimize the growth processes.

4.2 Experimental Results

For the investigations presented in this chapter an AlN bulk crystal from the University of Erlangen was used. It was grown by the method of Physical Vapor Transport (PVT) [32]. For more details on the material system see Appendix B. The crystal was cut from a larger boule and had a size of 5 mm x 3 mm x 1.5 mm. The coloration was yellowish (see Figure 4.1). XRD measurements showed that the crystal had a polycrystalline structure.

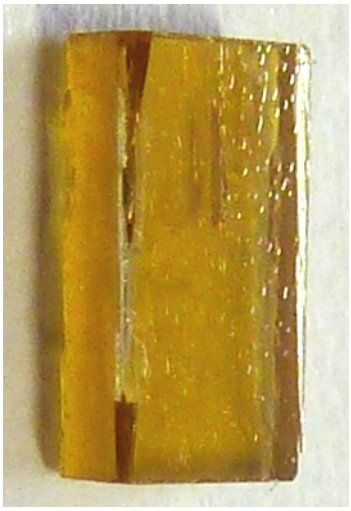

Figure 4.1: AlN crystal used for the investigations in this chapter

The sample was characterized by means of Raman spectroscopy, photoluminescence spectroscopy and

optical absorption spectroscopy. The results of these experiments are described in the following sections.

4.2.1 Raman spectroscopy

The Raman measurements were performed with a Renishaw Invia Raman microscope. Figure 4.2 shows a Raman spectrum recorded at room temperature with a 532 nm laser used for excitation. The E_2 (low), A_1 (TO), E_2 (high), E_1 (TO) and E_1 (LO) phonon modes, i.e. all allowed Raman modes, can be observed. The spectrum is dominated by the A_1 (TO) phonon mode, which is different from Raman spectra in the literature [33]. Comparing the present spectrum with experimental data from Bickermann et al. [33] the appearance of the A1 (TO) and the E1 (LO) phonon modes indicates that the sample was cut from the boule perpendicular to the growth direction of the crystal. From the position of the E_1 (TO) Raman mode one can estimate the stress in the sample along the c-axis of the crystal [34]. For increasing stress the peak position generally shifts to higher wavenumbers. In this case, the peak position of the E_1 (TO) Raman mode reflects a very low stress.

The full widths at half maximum (FWHM) values were determined for the A_1 (TO), E_2 (high) and E_1 (TO) Raman modes. They are all 6 cm^{-1} or smaller, which according to the literature is an indication for a high crystal quality of polycrystalline samples [33]. The Raman measurements delivered no indications for other phases or for the presence of high concentrations of impurities like oxygen [35].

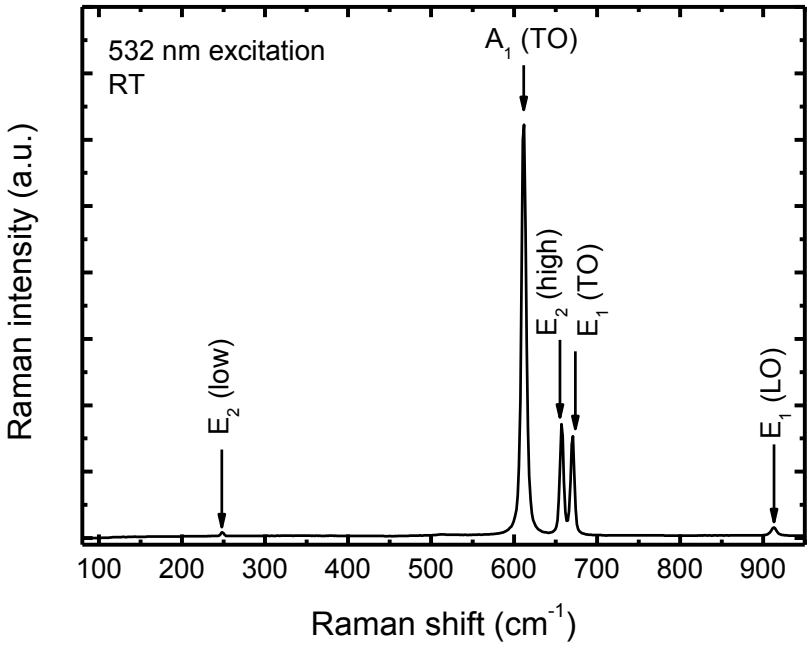

Figure 4.2: Raman measurement of the AlN crystal at room temperature. A laser with a wavelength of 532 nm was used for the excitation.

4.2.2 Photoluminescence measurements

The photoluminescence measurements were performed with a self-assembled setup, which consisted of an Omnichrome 3074 HeCd-Laser operating at a wavelength of 325 nm, an Oxford Helium bath cryostat with an adjustable temperature regime from 1.5 to 300 K and a Jobin-Yvon monochromator.

In Figure 4.3 a photoluminescence spectrum of the AlN sample is shown. It was recorded at a temperature of 4 K and a 325 nm laser was used for excitation. A broad asymmetric band centered at 2.75 eV can be observed as the only feature in this spectrum. It is important to mention, that the observation of near band edge photoluminescence signals was not possible because in the present measurements the excitation energy was low compared to the AlN band edge energy.

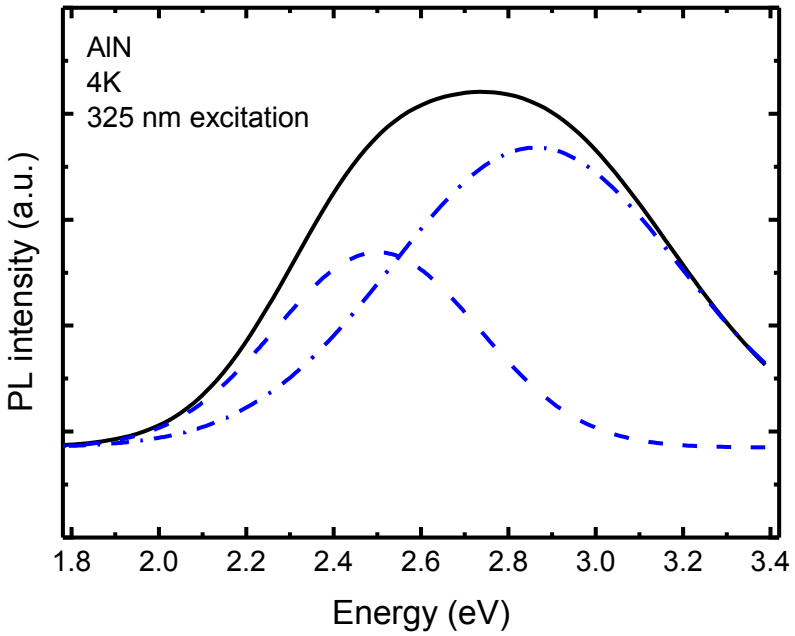

Figure 4.3: Photoluminescence spectrum (solid black line) of the AlN crystal at 4 K obtained using a 325 nm laser for excitation. The blue curves represent curves with Gaussian line shapes centered at 2.5 eV (dashed line) and 2.86 eV (dashed dotted line).

The line shape of the broad asymmetric band is well described by two overlapping PL signals. The latter also explains the asymmetry of the PL signal. For the analysis of the photoluminescence peaks a Gaussian line shape was assumed. The blue curves in Figure 4.3 indicate the two overlapping PL signals, the dashed one with a peak position of 2.5 eV and the dashed dotted curve peaking at 2.86 eV. In the literature, the broad photoluminescence band ranging from 2 to 3 eV centered at 2.8 eV has been assigned to an oxygen related defect [36, 37]. Results obtained by Lan et al. indicate that the photoluminescence peak at 2.6 eV might be attributed to nitrogen vacancies, but these results have not yet been confirmed by other groups [38].

4.2.3 Optical absorption spectroscopy

The optical absorption spectroscopy measurements were performed with a Perkin Elmer Lambda 900 spectrometer in combination with an Oxford helium flow cryostat. The sample temperature could be adjusted between 4 K and room temperature. Several transmission and reflection measurements were carried out at temperatures ranging from 4 K up to 300 K. From the data of these experiments the αd values as a function of the photon energy were calculated. These values are necessary for the interpretation of the photo-EPR measurements.

A generic spectrum of αd versus the photon energy and the photon wavelength of the AlN sample recorded at room temperature is shown in Figure 4.4. There are three optical absorption bands at 2.85 eV, 3.6 eV and 4.7 eV indicated by the vertical blue lines. Moreover, there is another absorption band in the shoulder of the 2.85 eV absorption band with its center at 2.5 eV (also indicated by a vertical blue line). Different models have been proposed in the literature to explain the broad absorption band with peaks at 2.5 eV and 2.85 eV. In older publications it was connected to either nitrogen vacancies, excess aluminum or oxygen related defects, but an exact assignment was not possible [39-41]. However, recent results raised doubts about these interpretations. For example theoretical calculations of the ionization levels [42] did not show satisfying agreement with the experimental data. Furthermore, the model for the oxygen vacancies was discarded and there are now evidences for a transition from an aluminum vacancy to a shallow donor [43]. The absorption band at 3.6 eV is possibly also caused by a transition from an aluminum vacancy, but in this case to the conduction band [43]. Finally, the absorption band at 4.5 eV can be attributed to oxygen vacancies [44].

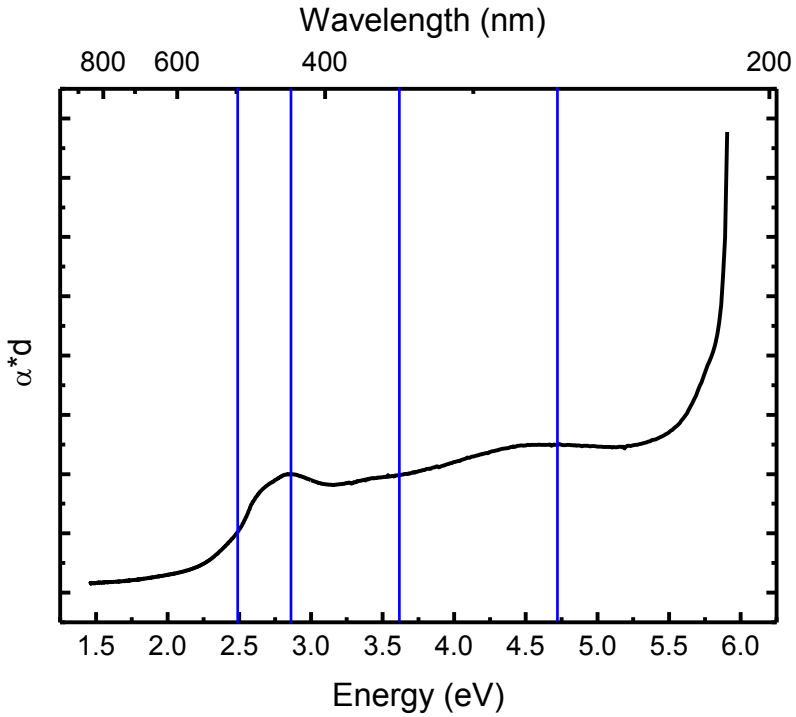

Figure 4.4: Plot of αd versus the photon energy and wavelength of the AlN crystal. The data were gathered during a transmission measurement at room temperature. The blue lines indicate the centers of several absorption bands.

4.2.4 Electron Paramagnetic Resonance

The EPR setup used for all measurements is the same as in the previous chapter and is described in the appendix. The EPR spectrum of the AlN sample without illumination is shown in Figure 4.5 (a). For the measurement the crystal was cooled down to 4 K in the dark to avoid ambient light effects. Apart from the signal of the microwave cavity (marked by an asterisk) one cannot observe any other EPR signal. Hence, without illumination there are no defects that are in a paramagnetic charge state. After illumination of the sample with UV light of a UVP UV spot lite system (see appendix for more information) a sharp signal at approximately 3400 Gauss appears (see Figure 4.5 (b)). The signal remains visible at low temperatures even if the UV light is switched off and there is only a slight decrease in intensity (see below). The signal only disappears after heating the sample up.

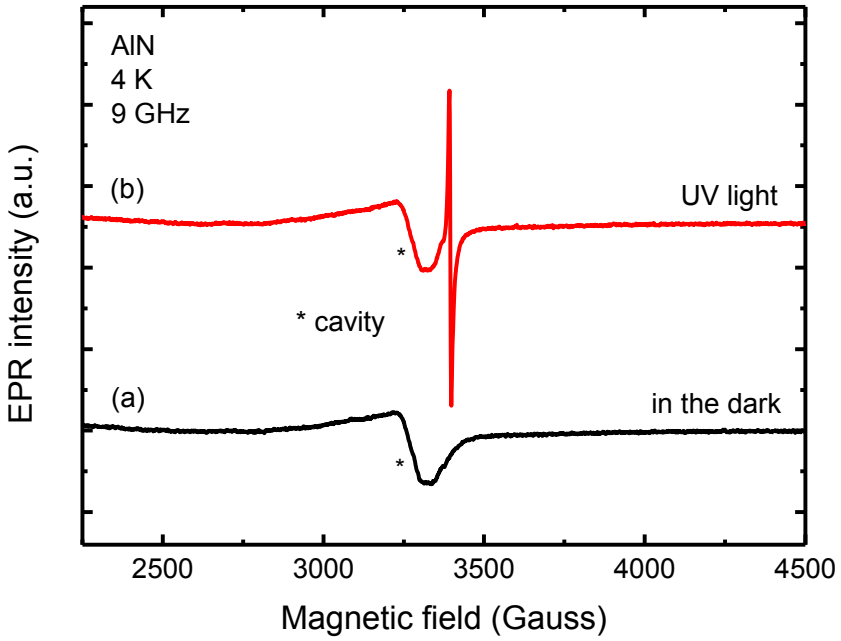

Figure 4.5: EPR overview spectra of the AlN crystal at 4 K with (b) and without (a) illumination with UV light. The signal caused by the microwave cavity is marked by an asterisk.

A more detailed EPR spectrum is depicted in Figure 4.6. Here, one can see two EPR signals that are close together. The first one is a sharp S=½ signal with a peak-to-peak width ΔB of 5 Gauss and a high peak-to-peak amplitude ΔI. It is located at a g-value of 1.99. Based on the similarity of the g-value and the line shape to the signal observed by Schweizer et al. it can be attributed to an isolated oxygen atom substituting a nitrogen atom, i.e. a (O_N) donor [36]. The second feature is a broader signal with a peak-to-peak width ΔB of 15 Gauss and a g-value of 2.003. The peak-to-peak amplitude ΔI of the signal is smaller than the amplitude of the first one. The observed g-value indicates that it represents an acceptor signal, which can possibly be assigned to a defect complex consisting of an aluminum vacancy and an oxygen atom substituting a nitrogen atom (V_{Al}-O_N) [36]. The EPR signal intensity given by $I_{EPR} \sim \Delta I \cdot \Delta B^2$ is similar for both signals.

As a next step the angular dependence of these signals was investigated in order to gain some more information on the defects. However, a rotation of the sample around any of its crystal axes did not change the EPR signals. This means that the signals are isotropic, which could be due to the polycrystalline character of the sample.

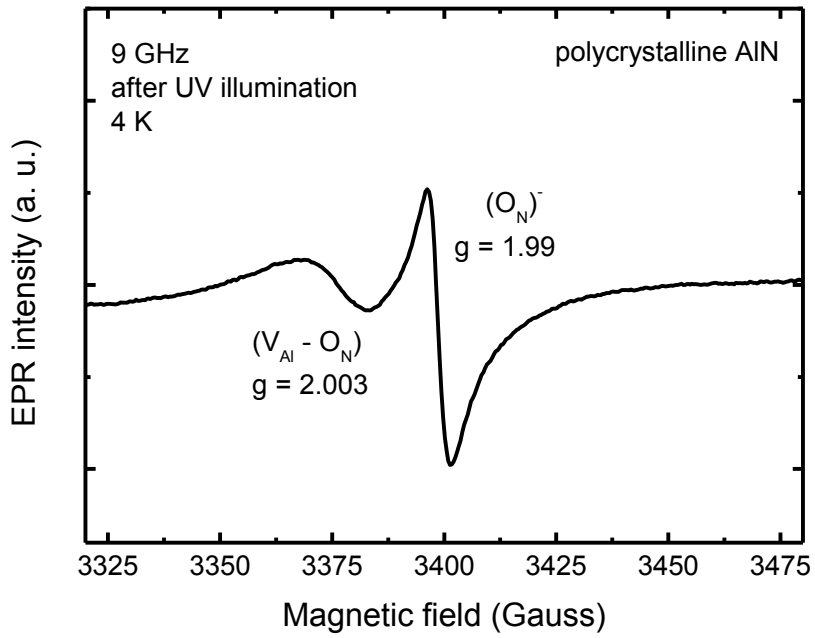

Figure 4.6: Detailed EPR spectrum of the AlN crystal after UV light illumination at 4 K. An acceptor signal at g = 2.003 and a shallow donor signal at g = 1.99 are observed.

Studying the temperature dependence of the EPR signal of a defect is a valuable tool to gain more information on its properties. The temperature dependent behavior of the donor and acceptor EPR signal intensity was measured from 4 K up to 240 K. For this purpose, the AlN sample was cooled down in the dark and afterwards illuminated with UV light in order to charge the defects into a paramagnetic charge state. Once the defects were in their paramagnetic charge state the light source was turned off to study the thermal decay of the EPR signals. In Figure 4.7 the AlN EPR spectra containing the donor and acceptor signals are shown for 4 K (black line), 22 K (red line), 50 K (green line) and 150 K (blue line). The intensity of the EPR donor signal decreases

very strongly with increasing temperature because of a decrease of both the peak-to-width and the peak-to-peak amplitude. The signal vanishes at 60 K. In contrast to this, the acceptor signal decreases less strongly and is stable up to 240 K. In this case, the peak-to-peak width remains constant and the peak-to-peak amplitude decreases with increasing temperature. Due to the high thermal stability as indicated by the small EPR signal intensity changes for the acceptor signal, it was not possible to calculate a reliable activation energy value for the defect. In the case of the donor signal, a very small value of 3 meV is obtained for the thermal activation energy (see below).

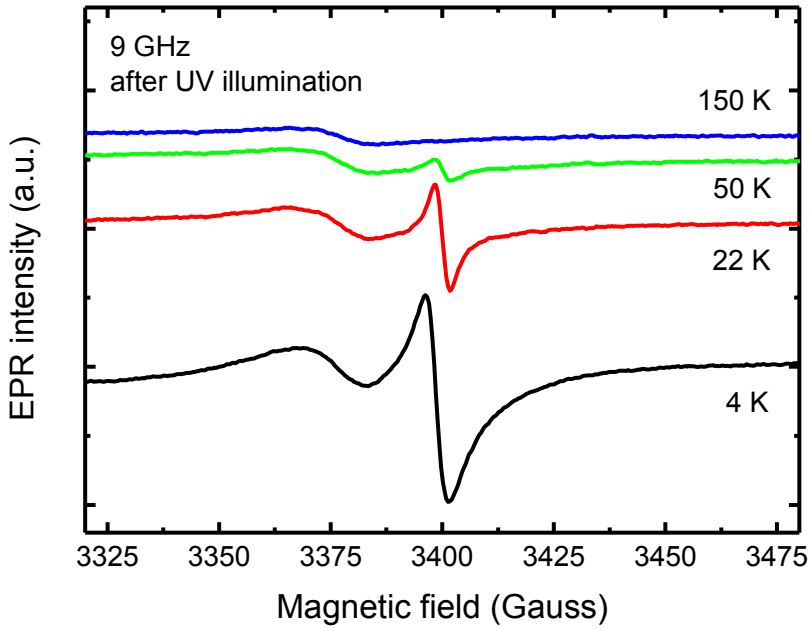

Figure 4.7: Series of detailed EPR spectra of the AlN sample with increasing temperature after illumination with UV light. The donor signal decreases strongly, whereas the acceptor signal is much more stable and is observable up to high temperatures.

The dependence of the AlN donor signal on the microwave power was investigated in order to ensure that the results of the EPR measurements are not influenced by saturation effects. Moreover, the relaxation times can be derived from these measurements using equations (3.2) to (3.6). In Figure 4.8 the dependence of the AlN

donor signal intensity on the square root of the microwave power is depicted for 4 K (square symbols) and 17 K (triangle symbols). As before, the sample was cooled down in the dark and then illuminated with UV light. The EPR signal intensity increases with increasing microwave power. For a better overview, a logarithmic scale was used for the EPR signal intensity, since for high microwave powers it quickly reaches high values. To indicate the linear behavior of the data a linear fit was inserted, represented by the blue lines. The fact that the linear behavior of the curve shown in Figure 2.1 is maintained for all microwave powers the EPR spectrometer could achieve proves that no saturation appears. While this behavior on the one hand makes it easy to choose the right microwave power for the EPR measurements, it leads on the other hand to the situation that it is impossible to derive the relaxation times using the saturation method described in the previous chapter.

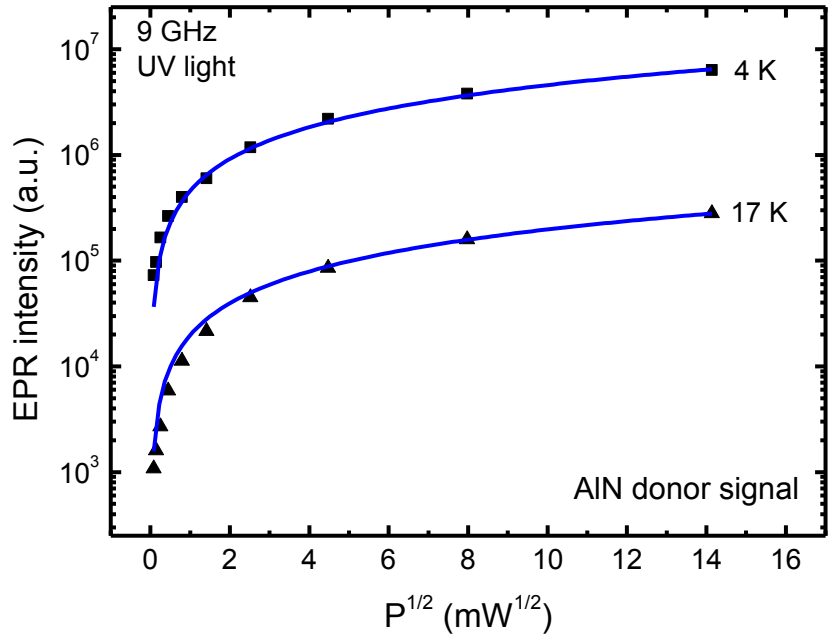

Figure 4.8: Dependence of the AlN donor EPR signal intensity on the square root of the microwave power for two different temperatures. The black squares show the data at 4 K and the black triangles represent measurements at 17 K. The blue lines indicate fits of the data points with a linear fit function.

The dependence of the EPR signal intensities of the donor and acceptor on the photon energy was also studied to gain a deeper insight into the photo transition processes. For this purpose, an array of laser diodes with wavelengths ranging from 980 nm to 490 nm was used. With these wavelengths it was not possible to charge the (V_{Al}-O_N) acceptor from the negative A^- state into the neutral A^0 state (see below). However, the dependence of the donor EPR signal intensity on the photon energy could be observed. To avoid photo-induced effects from previous measurements, it was necessary to heat the sample up to room temperature after each measurement at a specific wavelength and to cool it down to 4 K in the dark. This way the same initial state was reached for each data point. The results of these measurements are shown in Figure 4.9. The data points are fitted using equation (2.48) after the EPR signal intensity correction with the model proposed by Godlewski et al. [8]. The dependence of αd on the photon energy used to correct the EPR data is shown in Figure 4.4. From the optical cross section fit the ionization parameters can be determined. The optical ionization energy is $E_{opt} = 1.91\ eV$ and the broadening parameter equals $\Gamma = 0.17\ eV$. In order to derive the thermal ionization energy of the defect, which is connected to the thermal ionization energy by $E_{opt} - E_{th} = E_{rel}$, the temperature dependence of $\Gamma(T)$ could be measured, but again one should keep in mind that the amplitude and kinetics of light-induced EPR signals strongly depends on the rates of different capture processes. Moreover, due to the fact that capture processes change with temperature it is very difficult to obtain reliable values of E_{th} by this approach. Nevertheless, for small or moderate lattice relaxations as in the present case, the thermal ionization energy can be estimated from the edge of the photo excitation process of the EPR signal [8]. This way, the thermal ionization energy is estimated to $E_{th} = 1.75\ eV$ yielding a lattice relaxation energy of $E_{rel} = 0.16\ eV$.

After the donor EPR signal was created, the sample was also illuminated with infrared light from diode lasers in order to quench the signal again. However, quenching could not be observed. A possible explanation for this could be that the optical cross section for the photo transition from the defect level to the conduction band is too low.

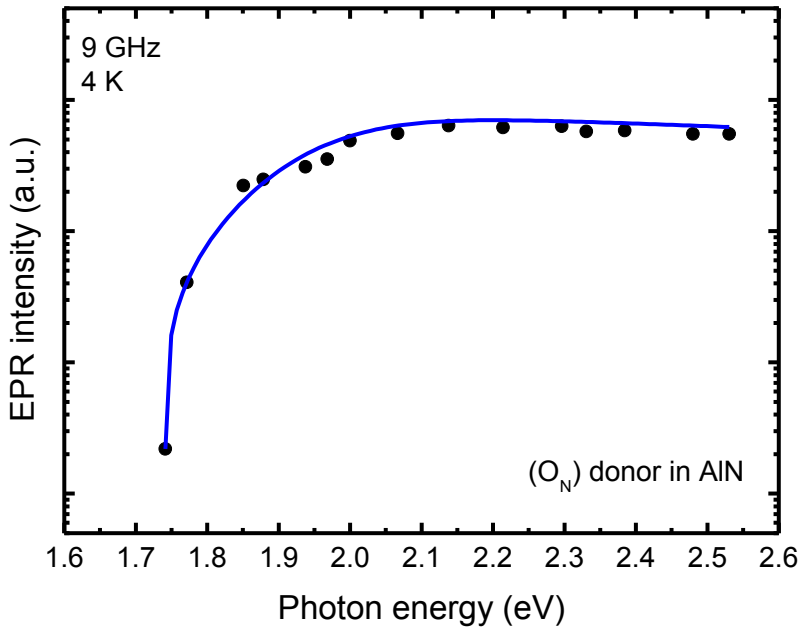

Figure 4.9: Dependence of the shallow donor EPR signal intensity on the photon energy measured at 4 K. The blue line indicates a fit of the optical cross section of the photo transition using equation (2.48).

As a next step the time dependence of the shallow donor signal creation process was observed. The sample was cooled down in the dark to 4 K and the EPR signal intensity was tracked over time at a fixed magnetic field value. The resulting curve is shown in Figure 4.10. The dataset was first fitted using a monoexponential function (see equation (3.6)), which is indicated by the dashed red line in Figure 4.10. However, the fit curve does not match the data points. In the inset of Figure 4.10, the saturation value of the photo-EPR intensity minus the photo-EPR intensity $ln(I_\infty - I)$ is plotted as a function of the time. If the photo-transition would follow a monoexponential behavior the data points could be described by a linear slope. However, one can observe a deviation from a linear behavior for the time regime shortly after the UV light was switched on. Since a monoexponential increase indicates that only one photo-transition process takes place, it is obvious that more than one photo-transition process occurs in this case. The first possibility to explain this is that two or more

photo transition processes are running in parallel. The mathematical description for such a behavior would be a sum of monoexponential growth functions (see equation (3.6)). The second option is that a certain number of photo-transition processes occur in series. In the latter case, the mathematical description is given by the product of monoexponential growth functions. The last option is a combination of both processes taking place in series and such occurring in parallel. Thus, the corresponding mathematical description is also a combination of both models.

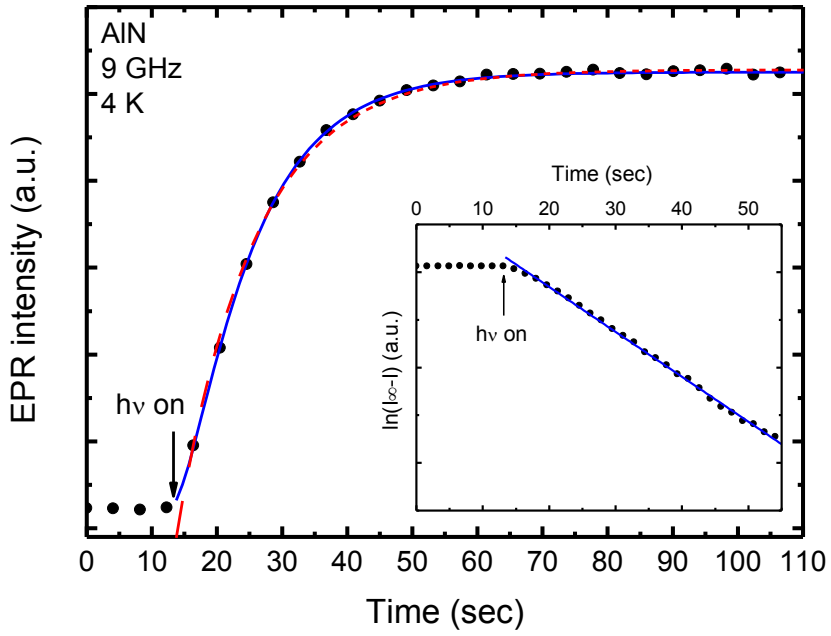

Figure 4.10: Time dependent study of the AlN donor EPR signal creation after the light source was switched on. The best fitting parameters are shown by the blue line. In the inset the saturation value of the photo-EPR intensity minus the photo-EPR intensity $ln(I_\infty - I)$ is plotted as a function of the time. The blue line represents a linear fit.

The slope of the EPR donor signal intensity curve is best described by the blue line in Figure 4.10 and was obtained with a complex model including two processes in series occurring in parallel to another process. However, the only thing that can be stated without any doubts is the fact that in this case there is involved more than one process.

After the light source has been switched off, one can observe a slight decay of the EPR signal intensity of the donor signal. The EPR signal intensity decreases by about 20 % of the initial value. To obtain more information on the decay process, the time dependence of this effect was studied (see Figure 4.11). The measurement was performed at 4 K after cooling down the sample in the dark. After that the sample was illuminated to create the EPR signal and subsequently the light source was switched off. One can observe an exponential change of the EPR signal intensity with time. Again, various fits using all three models described in the paragraph above were performed. In this case, a multi-exponential decay assuming two processes running in parallel delivers the best results. The corresponding fit curve is indicated by a blue line in Figure 4.11. The fit yields the time constants of $T_1 = 4.9\ s$ and $T_2 = 68.6\ s$. Thus, the decay process consists of a slow and a fast process. Fast photo-transition processes are usually non-radiative, whereas fast ones are radiative.

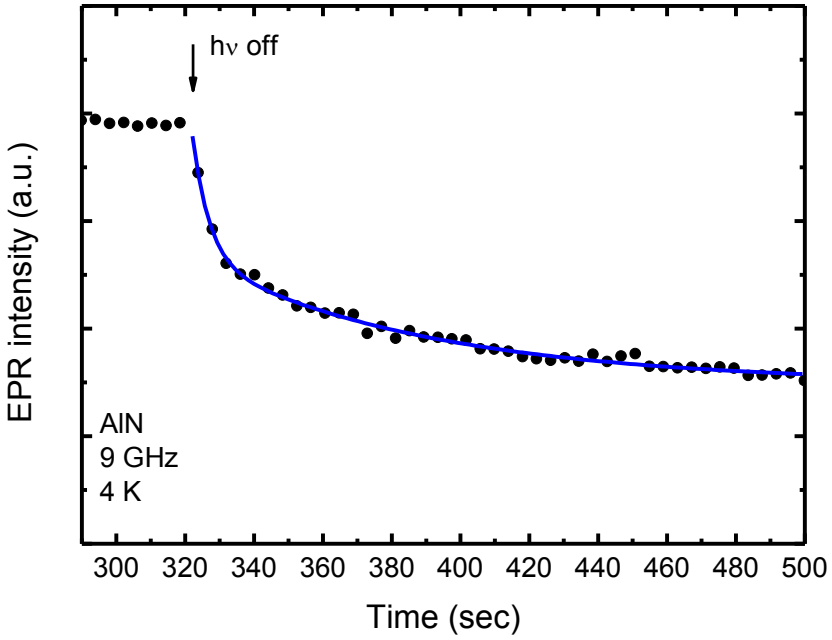

Figure 4.11: Time dependence of the AlN donor EPR signal intensity after switching off the light source. The blue line indicates a fit based on a multi-exponential decay model.

By the means of the information collected in all the EPR experiments described in the last section it is possible to draw an energy level diagram (see Figure 4.12). Since the donor signal is not observable in an EPR measurement in the dark its energy level position has to be above the Fermi energy level. After illumination with wavelengths shorter than 710 nm (corresponding to 1.75 eV), the donor signal appears in the EPR spectra. Considering that the band gap of AlN is nearly 6 eV, it is obvious that the electron charging the donor into its paramagnetic charge state does not come from the valence band. From the photo-EPR data one can conclude that there is another defect state located 1.9 eV below the conduction band, most likely also a donor. This hypothesis is supported by the results of the time dependent photo-EPR measurements, which suggest two photo transitions for the creation process of the EPR donor signal. Such a recombination path is shown in Figure 4.12 with the blue arrows.

$$(D?)^0 + h\nu \rightarrow (D?)^+ + e^-$$

$$(O_N)^+ + e^- \rightarrow (O_N)^0$$

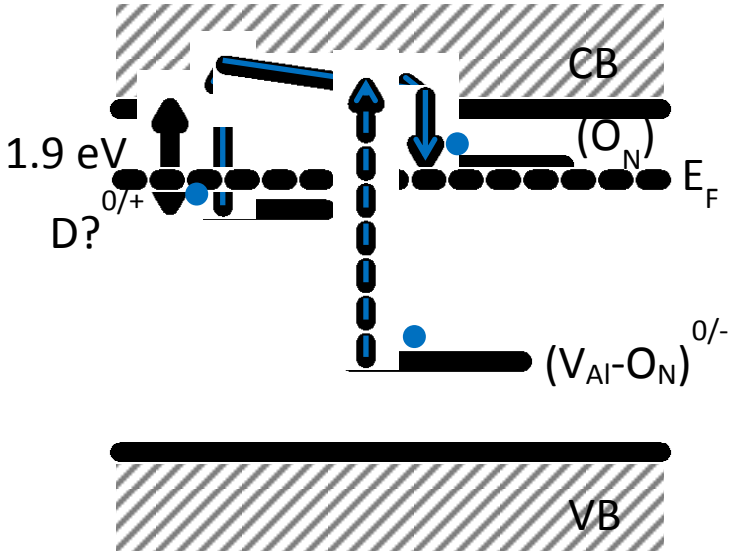

Figure 4.12: Energy level diagram of the donor and acceptor levels in AlN investigated in this chapter.

A drawback on this model is the fact that the (D?) defect could not be observed in the EPR experiment, no matter if the sample was illuminated or in the dark.

The only information gathered about the energy level of the (V_{Al}-O_N) acceptor is the fact that it becomes observable in the EPR experiment after the illumination with UV light, therefore it was in a non-paramagnetic charge state before the latter. Due to the high thermal stability of the acceptor, which is revealed from the temperature dependent measurements, one can conclude that it is a deep acceptor level. However, another possibility is to assume that the (V_{Al}-O_N) acceptor is the defect from which the electron being transferred to the (O_N) donor originates. In this case, the (V_{Al}-O_N) defect level would be located 1.9 eV below the conduction band edge. This could be a reason why the (D?) defect could not be observed in the EPR experiment with or without illumination. A strong argument against this is the fact that the (V_{Al}-O_N) acceptor appears only in EPR spectra after the sample is illuminated with UV light from a UVP spot light system with 254 nm. This corresponds to an energy of 4.9 eV and gives one limit of the energy regime in which the (V_{Al}-O_N) acceptor is located. The other energy limit is given by the minimal wavelength of the bandpass filters used for the photo-EPR measurements, which equals 2.53 eV. Together with the value of the optical band gap (E_{gap} = 6 eV) attained from the optical absorption measurements, one can estimate the energy level position of the (V_{Al}-O_N) acceptor to be at least 1.1 eV but not more than 3.5 eV above the valence band edge. The corresponding recombination path is shown in Figure 4.12 by the dashed blue arrow.

$$(V_{Al} - O_N)^- + h\nu \rightarrow (V_{Al} - O_N)^0 + e^-$$

4.3 Discussion

After illumination of the AlN crystal with wavelengths shorter than 710 nm an S=½ EPR donor signal with a g-value of 1.99 becomes observable. Based on the similarity of the g-value and the line shape of the EPR signal observed by Schweizer et al. the donor signal could be assigned to a defect containing an oxygen atom substituting a nitrogen atom (O_N) [36]. This assignment is in accordance with the photoluminescence results, which also indicate the presence of oxygen related defects because of the appearance of a PL band at 2.85 eV [37]. Furthermore, the optical absorption band at 4.7 eV is connected to the presence of oxygen related defects [44]. Additionally,

oxygen is a common extrinsic defect in AlN that can be easily incorporated during the growth of the crystals.

From the temperature dependent behavior of the (O_N) defect one can see that the EPR signal already vanishes at 60 K. The activation energy is estimated to be approximately 3 meV. A possible explanation for this behavior is a negative correlation energy U of the (O_N) donor in AlN. The paramagnetic donor appears to be unstable. It is energetically preferred for the donor to accept another electron from a donor, which leaves the former donor in the non-paramagnetic d^+ state. The donor, which now possesses two electrons, transforms into the non-paramagnetic DX^- state. Since there is a strong coupling between the electronic and vibrational system the energy level of the DX center drops deep into the band gap [45-47]. Together with the photo-EPR data which show a non-paramagnetic donor state 1.9 eV below the conduction band it seems obvious to assign the unknown (D?) donor level to the DX^- center. The corresponding configuration diagram is shown in Figure 4.13.

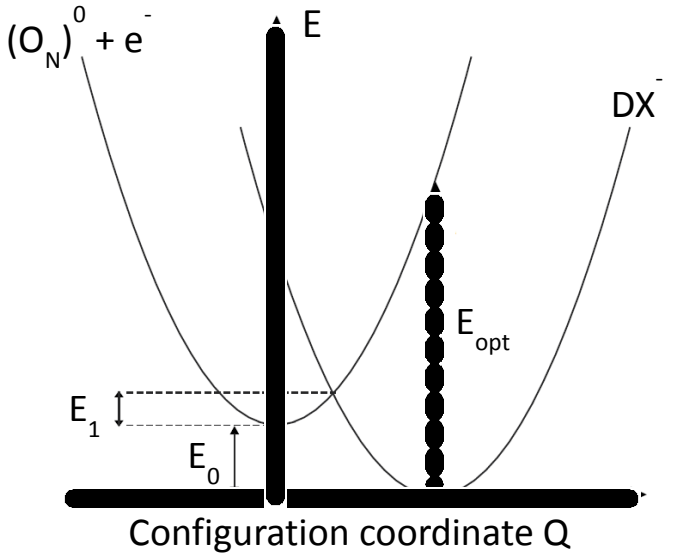

Figure 4.13: Configuration coordinate diagram for DX centers in AlN after [46]. The DX center is more stable than the (O_N) center.

On the right side is the parabola of the DX^- center shown and on the left side the parabola of the metastable donor which generates the (O_N) donor EPR signal; they are

separated by the energy E_0. Note that there is a large Stokes shift between the optical ionization energy E_{opt} and the thermal ionization energy $E_{th} = E_1 + E_0$ of the DX^- center. Due to illumination at low temperatures the stable but non-paramagnetic d^+ and DX^- states transform by the capturing of the free electron by the d^+ state into two metastable d^0 states. With Electron Nuclear Double Resonance (ENDOR) experiments it can be proved that the donor signals correspond to coupled pairs with an exchange interaction in the lowest triplet state [45, 46]. However, with EPR measurements alone it is not possible to resolve S=½ and S=1 states, since the EPR spectra are identical in both cases. There is an energy barrier E_1 between the metastable state and the DX^- state which prevents a counter reaction from the DX^- state back to the stable state. By an increase of the temperature the energy barrier can be overcome and the (O_N) EPR signal disappears. With the temperature dependency of the (O_N) EPR signal intensity a value of E_1 can be roughly estimated to 3 meV.

A further evidence for this model is the lack of defects in AlN with recombination energies in the range of 1.9 eV [42, 43].

For the acceptor found in the EPR measurements the attribution to a (V_{Al}-O_N) defect complex is due to the similarity of the g-value and line shape of the EPR signal observed by Schweizer et al. the most likely one [36]. The 2.8 eV optical absorption band confirms the presence of aluminum vacancies in the sample and from theoretical calculations it is known that the formation energy of (V_{Al}-O_N) defect complexes is very low what gives a further support for this model [42, 48]. The energy level position is located in a range from 1.1 eV above the valence band edge to 3.5 eV above the valence band edge. Bickermann at al. attributed an optical absorption with an energy of 4.4 eV to a transition from $(V_{Al}\text{-}O_N)^{-/2-}$ to the conduction band [43]. The latter energy is in the energy range estimated for the (V_{Al}-O_N) defect.

5 Characterization of Gallium Oxide

5.1 Introduction

The compound semiconductor gallium oxide with its thermodynamically stable β-Ga_2O_3 phase is a wide band gap material with an band gap E_{opt} = 4.9 eV [49]. When synthesized or annealed under reducing conditions, gallium oxide shows n-type semi-conductive behavior. That originates from oxygen vacancies acting as shallow donors with ionization energies in the range of 20 to 40 meV [50, 51]. Thus β-Ga_2O_3 is a suitable material for deep UV transparent conducting oxide (TCO) applications [52, 53]. Due to the fact that the electrical conductivity of β-Ga_2O_3 changes in oxidizing and reducing atmospheres noticeably and reversibly at high temperatures, it can be used as gas sensor [54, 55]. Anther applications is as luminescent phosphors [51]. From the technological point of view one would prefer to control the electrical and optical properties by doping, but up to date only rare information exists on the nature of elements causing either n- or p-type conductivity in β-Ga_2O_3. By a substitution of gallium, which is three times positively charged in the crystal, group II elements such as Zn, may act as p-type dopants and group IV elements may cause n-type conductivity. Considering the oxygen sub-lattice, one may expect group V elements to cause acceptors, and group VII elements to cause donors. Surprisingly, information on such potential donors and acceptors in Ga_2O_3 is very limited.

This chapter deals with the characterization of β-Ga_2O_3 bulk crystals and powder by electron paramagnetic resonance (EPR) and optical spectroscopy.

5.2 Gallium Oxide bulk crystals

The β-Ga_2O_3 bulk crystal used for characterization in this section was grown by the Czochralski technique by the Leibniz institute for crystal growth in Berlin. The crystal boule had a maximum diameter of 20 mm and was cut into slices, 5 mm in thickness. Since β-Ga_2O_3 has a natural (100) cleaving plane, it is very easy to cleave smaller samples from the crystal along this plane. Obtaining suitable surfaces for optical measurements perpendicular to this plane is problematic, because the crystal is cleaved unintentionally along the (100) plane when small forces are applied. Therefore

polishing is also difficult. Since surface properties are not that important for a volume technique like EPR, a sample with a splinted surface and a size of 6 mm x 3 mm x 1.5 mm was used for the EPR measurements. For XRD, Raman and optical absorption measurements small thin plates (3 mm x 2 mm x 0.2 mm) with surfaces as smooth as possible were cleaved from the large crystal.

5.2.1 X-ray diffraction measurements

The x-ray diffraction measurements were performed with a Siemens D 5000 diffractometer with Cu Kα1-radiation (40 kV, 20 mA). Effects due to Cu Kα2-radiation and background radiation were eliminated from the experimental data by the analysis software (X-Pert Highscore Plus). An x-ray diffractogram of the β-Ga_2O_3 sample is depicted in Figure 5.1. It is dominated by 3 reflexes which can be assigned to the crystallographic (400), (112) and (800) axes [56].

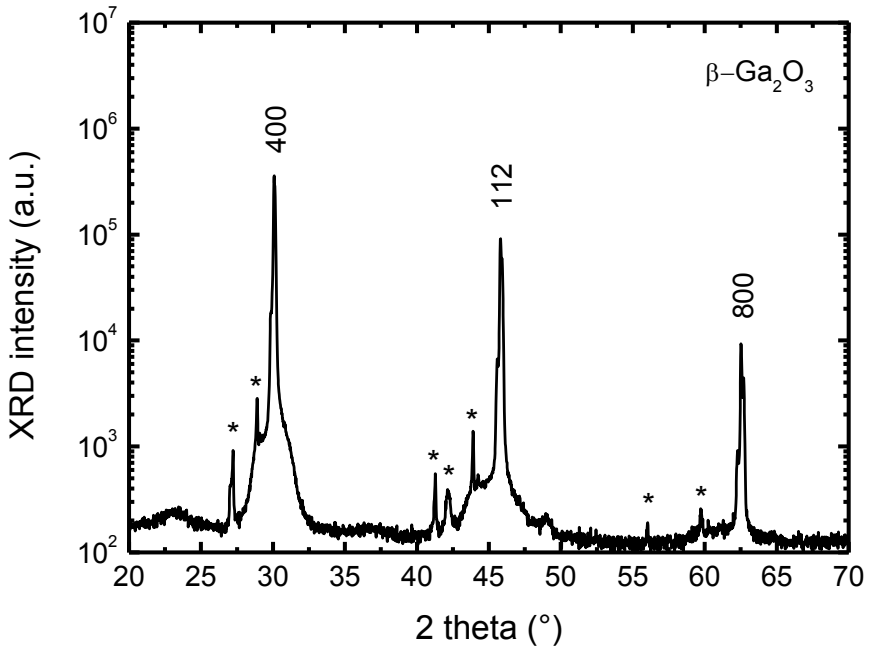

Figure 5.1: X-ray diffraction measurement of a β-Ga_2O_3 crystal.

Therefore the a-axis points out of the surface of the crystal, which coincides with the fact that the crystal was cleaved along the natural (100) cleaving plane. There are some small reflexes (marked by asterisk symbols) at least 2 orders of magnitude smaller in intensity, which could not be assigned to β-Ga_2O_3. An explanation for these reflexes could be given by crystal twins. Foreign phases seem to be unlikely, since in XRD reflex databases there are no indicators found for reflexes located at the given 2υ values, at least for reasonable elements and compounds. However, the presence of non-crystalline foreign phases cannot be excluded due to the results of the XRD measurements.

5.2.2 Raman spectroscopy

To further ensure the absence of foreign phases the β-Ga_2O_3 crystal was investigated by Raman spectroscopy. The measurements were performed with a Renishaw Invia Raman microscope. A room temperature Raman spectrum of a β-Ga_2O_3 crystal with a laser operating at 633 nm used for excitation is depicted in Figure 5.2. In total eleven Raman modes in three groups can be observed. According to Dohy et al. [57] the modes at 114 cm^{-1}, 147 cm^{-1}, 169 cm^{-1} and 199 cm^{-1}, respectively are attributed to the libration and translation of the doubly connected straight chains of GaO_6 edge shared octahedra running along the b-axis of the crystal. The Raman modes at 318 cm^{-1}, 346 cm^{-1}, 415 cm^{-1} and 475 cm^{-1}, respectively are connected to the deformation of the GaO_6 octahedra. The origin of the last group of Raman modes located at 628 cm^{-1}, 657 cm^{-1} and 763 cm^{-1} represents the stretching and bending of GaO_4. Since only allowed β-Ga_2O_3 modes can be observed in the Raman measurements, there are again no indicators for additional phases in the samples.

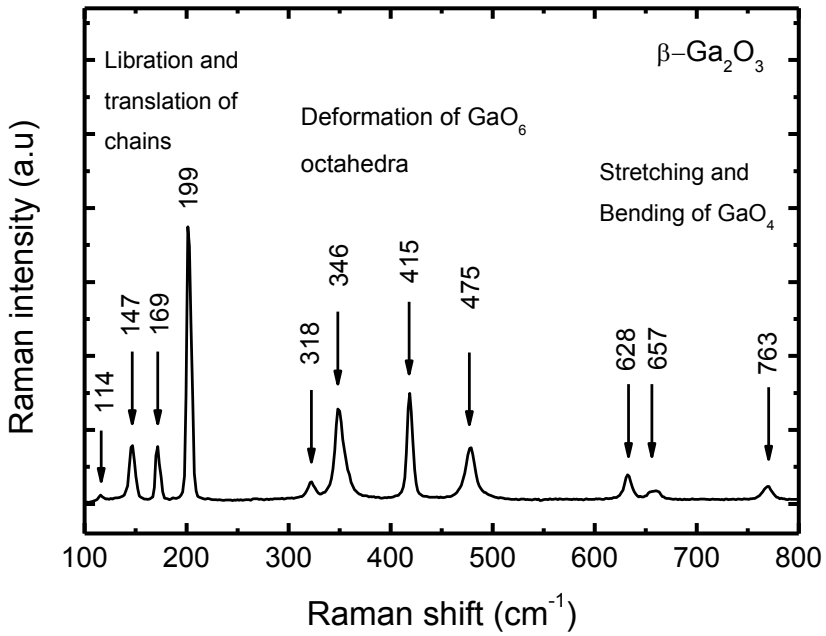

Figure 5.2: Raman spectrum of the β-Ga_2O_3 crystal measured at room temperature with a 633 nm laser used for excitation.

5.2.3 Optical absorption spectroscopy

The optical absorption measurements were carried out with a Perkin Elmer Lambda 900 spectrometer in combination with an Oxford helium flow cryostat. Thus the sample temperature was adjustable between 4 K and room temperature. Several transmission and reflection measurements were performed using the full temperature range available. In Figure 5.3 is a transmittance spectrum of a β-Ga_2O_3 crystal shown. The measurement was performed at room temperature and one can observe two absorption edges in β-Ga_2O_3. The fundamental absorption edge is dependent on the orientation of the electric field vector $\vec{E}$ of the incident light. In fact the orientation towards the b-axis of the crystal is relevant (for more information on the β-Ga_2O_3 crystal structure see appendix); therefore the observed absorption edges are marked as E ∥ b and E ∥ c. An explanation for this behavior is given by Ueda et al. [58, 59]. By tight-binding band calculations they consider the electronic structure of β-Ga_2O_3 as it is depicted in the inset of Figure 5.3. The conduction band minimum at the center of

the Brillouin zone is mainly constituted by Ga 4s orbitals with a Γ_1^+ symmetry. However, the top of the valence band has an oxygen 2p character and according to the group theory the direct allowed transition to the Γ_1^+ state occurs only from the Γ_1^- state for E ∥ c and from the Γ_2^- state for E ∥ a and E ∥ b. Since the only observed transitions originate from the Γ_1^- and Γ_2^- valence band states to the Γ_1^+ conduction band state, the valence band maximum has to have a Γ_1^- symmetry and the next valence band with Γ_2^- symmetry is just beneath it. The transitions from the Γ_1^+ and Γ_2^+ valence band states to the conduction band minimum with Γ_1^+ symmetry are direct forbidden.

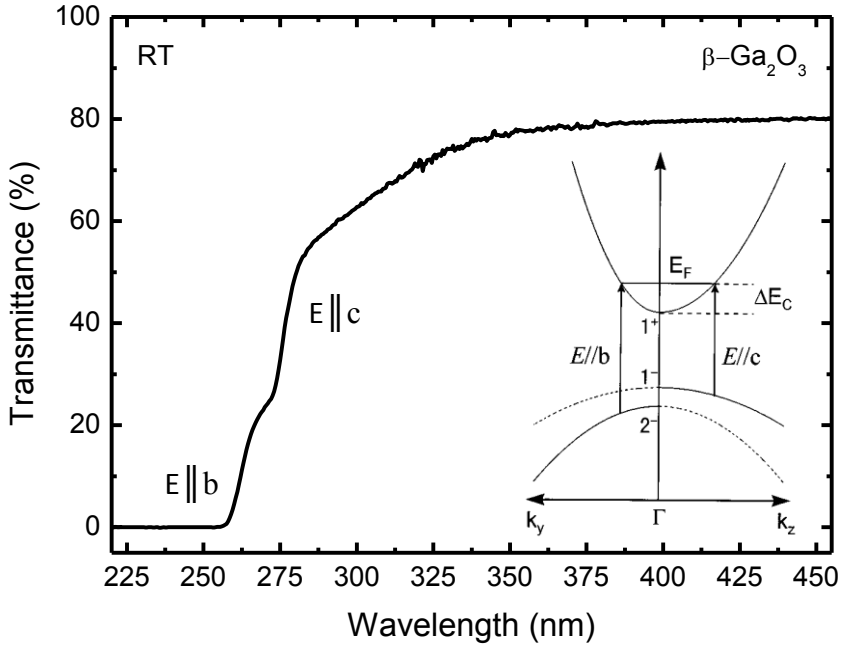

Figure 5.3: Transmittance spectrum of the β-Ga_2O_3 crystal measured at room temperature. In the inset is a schematic diagram of the band structure of β-Ga_2O_3 depicted showing the different band gap energies for E ∥ b and E ∥ c [59].

A generic reflection spectrum measured at room temperature of the β-Ga_2O_3 sample is depicted in the inset of Figure 5.4. The measurements show a constant I_{ref} value of about 20 % over the complete range from 250 nm to 650 nm (corresponding to 2 eV to 5 eV). The refection remains constant for a temperature regime ranging from 4K up to

room temperature. To estimate the band gap energy one first has to calculate αd which is given by:

$$\alpha d = \frac{100\% - I_{ref}(\%)}{I_{trans}(\%)} \tag{5.1}$$

The αd value is then modified according to the transition behavior of the absorption. In the present case it is a direct allowed transition, therefore the modification of αd is an exponent of 2. Now $(\alpha d)^2$ is plotted versus the photon energy, such a graph is shown in Figure 5.4 for room temperature. The band gap energy can be determined through linear extrapolation, indicated by a dashed blue line for the orientation E ‖ b and a solid blue line for E ‖ c. In both cases the energy position on the x-axis of the graph is marked by vertical blue lines.

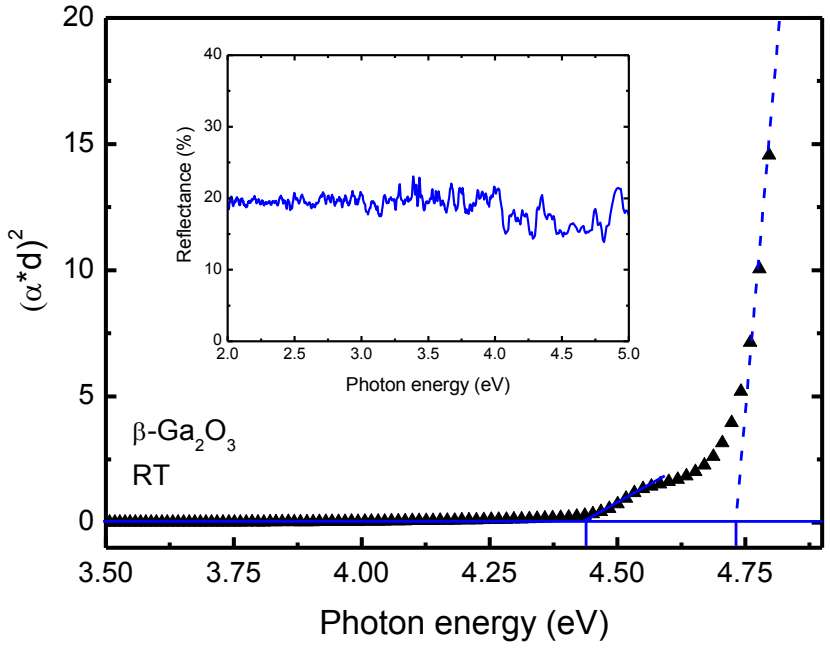

Figure 5.4: $(\alpha d)^2$ of the β-Ga_2O_3 sample is depicted as a function of the photon energy. The band gap energy is determined by linear extrapolation (indicated by dashed and solid blue lines). The inset illustrates the reflectance plotted versus the photon energy for a room temperature measurement.

The band gap energy was tracked from room temperature down to 4 K for E‖b and E‖c. The temperature dependence of the band gap energies of the respective orientations is shown in Figure 5.5. The curves can be described by a model given by O'Donnel et al. [60]:

$$E_g = E_{g0} - S\langle\hbar\omega\rangle\left(\coth\left(\frac{\langle\hbar\omega\rangle}{2k_BT}\right) - 1\right) \tag{5.2}$$

In this case E_{g0} defines the band gap energy at zero temperature analogously to the Varshni model [61], whereas S is a dimensionless coupling constant and $\langle\hbar\omega\rangle$ describes the average phonon energy. This notation was adopted by O'Donnel et al. from the vibronic model of Huang and Rhys [62].

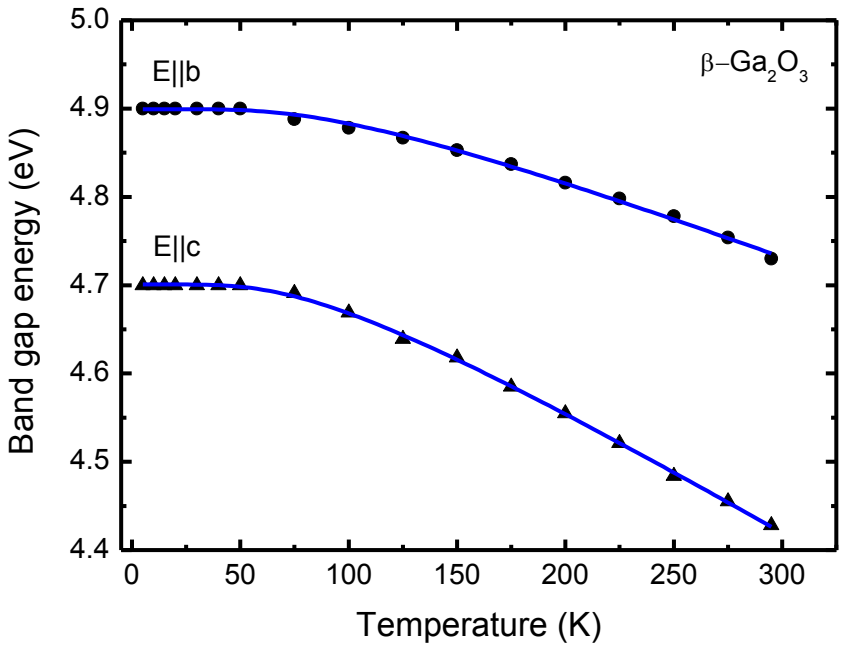

Figure 5.5: Temperature dependence of the band gap energy of β-Ga_2O_3. The behavior is shown for E‖b (parallel to the GaO_6 octahedron chains) as well as E‖c (perpendicular to the GaO_6 octahedron chains). The blue lines indicate fits using equation (5.2).

The blue lines in Figure 5.5 indicate fits using equation (5.2) with the following parameters:

$$E \parallel b\text{: } E_{g0} = 4.9\ eV, \qquad S = 5.4, \qquad \langle \hbar\omega \rangle = 24.5\ meV$$

$$E \parallel c\text{: } E_{g0} = 4.7\ eV, \qquad S = 8.5, \qquad \langle \hbar\omega \rangle = 21.5\ meV$$

The values determined for E_{g0} are in agreement with the values known from the literature [49]. The determined Huang Rhys factors (S > 5) indicate a moderate electron phonon coupling. Similar values are observed by photoluminescence measurements for chromium in β-Ga_2O_3 by Nogales et al. [63]. The phonon energies of the measured β-Ga_2O_3 crystal range from 14 meV to 94 meV with an average value of 47 meV. But one has to take into account that the model of O'Donnel et al. [60] is no exact determination of the phonon energies.

5.2.4 EPR measurements

The EPR measurements were performed with the Bruker spectrometer described in the appendix. The β-Ga_2O_3 crystal was mounted on the sample holder in a way that the rotation was around the b-axis of the crystal. For all EPR measurements described in this section the sample was cooled down in the dark to avoid ambient light effects.

An EPR overview spectrum of a β-Ga_2O_3 crystal is depicted in Figure 5.6. The measurement was taken at 10 K with the a-axis of the crystal parallel to the magnetic field. Three signals in the EPR spectrum marked as I, II and III can be observed. The resonance due to the microwave cavity is indicated by an asterisk. Signal I consist of 8 equidistant lines centered at 1070 Gauss. Signal II and III each consist of only one line, they are located at 2875 Gauss and 3457 Gauss.

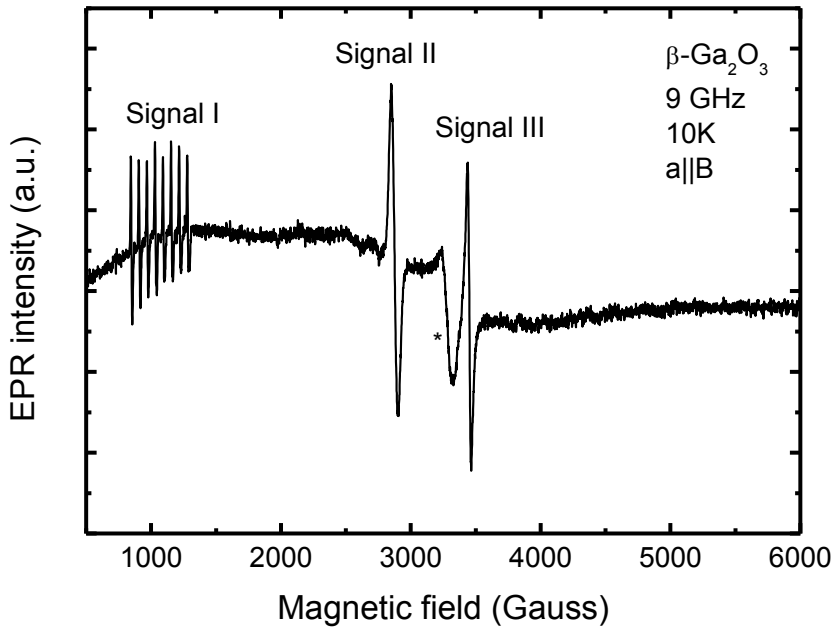

Figure 5.6: EPR overview spectrum of a β-Ga_2O_3 crystal measured at 10 K with the a-axis of the crystal parallel to the magnetic field. Three EPR signals marked as I, II and III can be observed. The effect due to the cavity is indicated by an asterisk.

The illumination with UV light of a UVP spot light lamp (minimal wavelength 254 nm) did not alter the EPR signals in any form. The origins of these signals in particular will be discussed in the following sections.

Signal I and signal II show a distinct angular dependent behavior, however signal III does not. In Figure 5.7 several overview spectra are depicted for a rotation of the sample around the b-axis. The measurements were taken at 10 K rotating the sample by 180°, starting at a position with the a-axis parallel to the magnetic field. The resonance due to the microwave cavity is again marked by an asterisk.

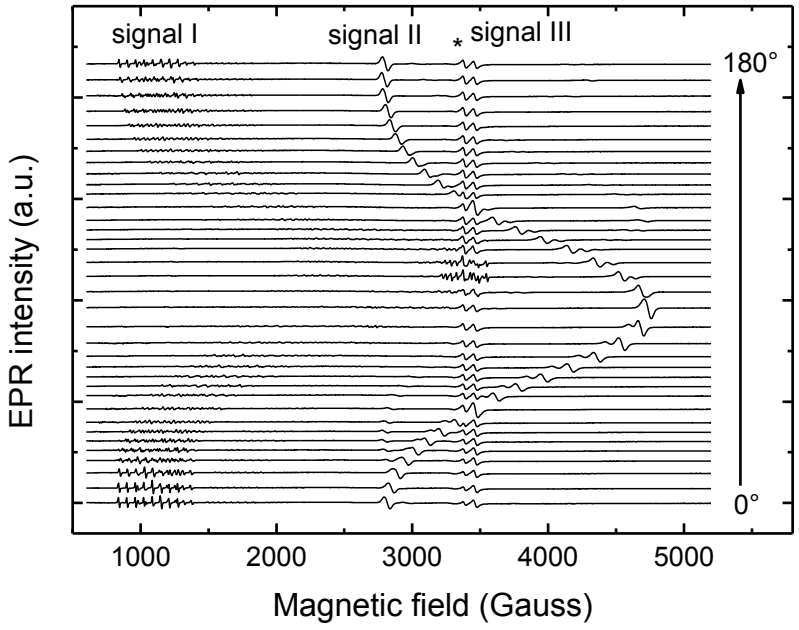

Figure 5.7: EPR overview spectra of β-Ga_2O_3 measured at 10 K. The crystal was rotated around the b-axis by 180° starting from a parallel B. The angular dependent behavior of signal I, signal II and signal III was tracked.

Signal I

A detailed EPR spectrum measured at 10 K with the a-axis of the crystal parallel to the magnetic field is shown in Figure 5.8. Signal I consists of 8 equidistant lines (marked by a black rake) indicating a hyperfine interaction with a nuclear spin I = 7/2 and 100 % natural abundance. The origin of this hyperfine interaction will be discussed later in this section in conjunction with the data from the angular dependent EPR measurements. The 8 signals have the same peak-to-peak intensity ΔI and a line width ΔB of 9 Gauss. If the sample is heated up, signal I can be observed up to temperatures of 35 K. Beyond this value it vanishes.

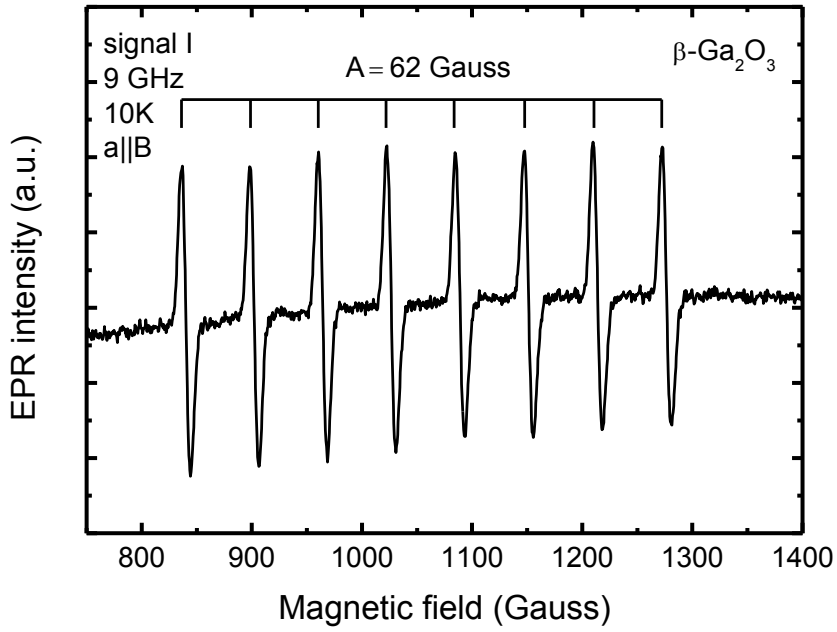

Figure 5.8: Detailed EPR spectrum of Signal I measured at 10 K with the a-axis parallel to the magnetic field. The hyperfine splitting with a hyperfine coupling constant of 62 Gauss due to a nuclear spin I = 7/2 is indicated by a rake.

To determine the full set of parameters necessary to describe this defect with a spin-Hamiltonian in the form of

$$H = \mu_B \vec{B} \hat{g} \vec{S} + \vec{S} \hat{A} \vec{I} + \vec{I} \hat{P} \vec{I} - g_N \mu_N \vec{B} \vec{I}, \tag{5.3}$$

angular dependent measurements of signal I were performed at a temperature of 10 K. Therefore the sample was rotated around the b-axis of the β-Ga_2O_3 crystal by 240° in 5° steps. The measurement was started from a position with the a-axis of the crystal parallel to the magnetic field. The results of these measurements are depicted in Figure 5.9. The magnetic field position of signal I is plotted versus the rotation angle, whereas the perpendicular and parallel orientations of the a-axis towards the magnetic field are indicated by vertical dashed lines. Hence, the g-values and the hyperfine coupling constant are determined to the following:

$$g_{a\|B} = 6.4,\ g_{a\perp B} \approx 2.8,\ A_{a\|B} = 62\ Gauss \text{ and } A_{a\perp B} \approx 107\ Gauss$$

The EPR signal intensity is also angular dependent, it reaches its maximum value for a‖B, whereas for a⊥B the intensity is extremely slight. Therefore the exact g-value and hyperfine coupling constant are only approximate values for the latter orientation. Due to this fact it was not possible to calculate reliable values for the isotropic and anisotropic hyperfine coupling constants. Furthermore, the angular dependence yields the information that the defect is aligned along the a-axis of the crystal. Due to the natural (100) cleaving plane it was not possible to prepare an appropriate sample for a measurement around another axis of the crystal. Therefore the full set of spin-Hamilton parameters could not be determined.

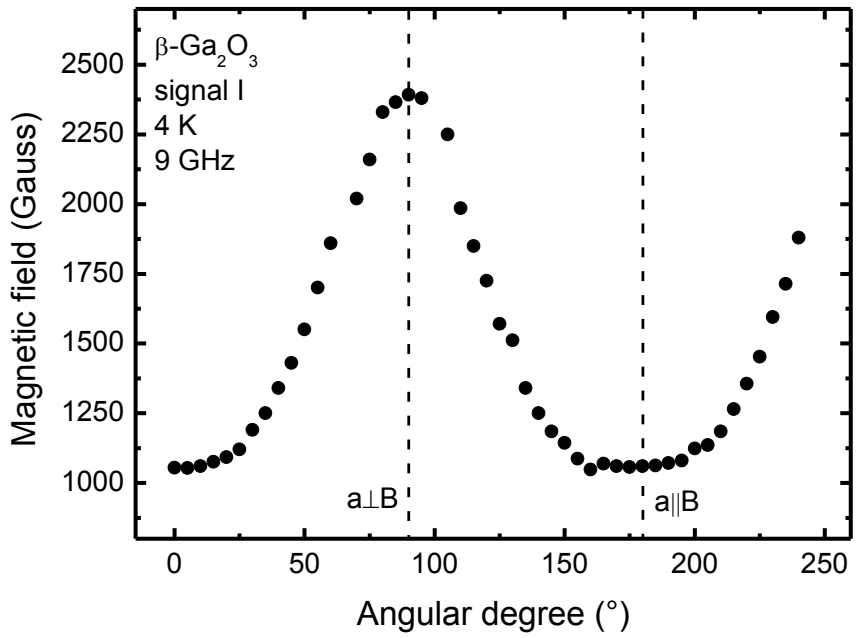

Figure 5.9: Angular dependent magnetic field position of signal I measured at 10 K. The orientations of the a-axis of the crystal towards the magnetic field are indicated by vertical dashed lines.

To be sure that the EPR measurements are not distorted by saturation effects, it is useful to investigate the microwave power dependence of the EPR signals. From that data it is also possible to gather more information on the relaxation behavior of the defect electrons. The spin-lattice relaxation time T_1 and the spin-spin relaxation time

T_2 can be calculated from the microwave power dependent saturation behavior of the EPR signal. The following measurements were carried out at 10 K. In Figure 5.10 the peak-to-peak amplitude y_m' of signal I is plotted against the square root of the microwave power. For low microwave powers a linear behavior between the peak-to-peak amplitude and the square root of the microwave power can be observed (indicated by a dashed blue line). The maximum peak-to-peak amplitude is reached for a microwave power of 10 mW, thereafter saturation occurs.

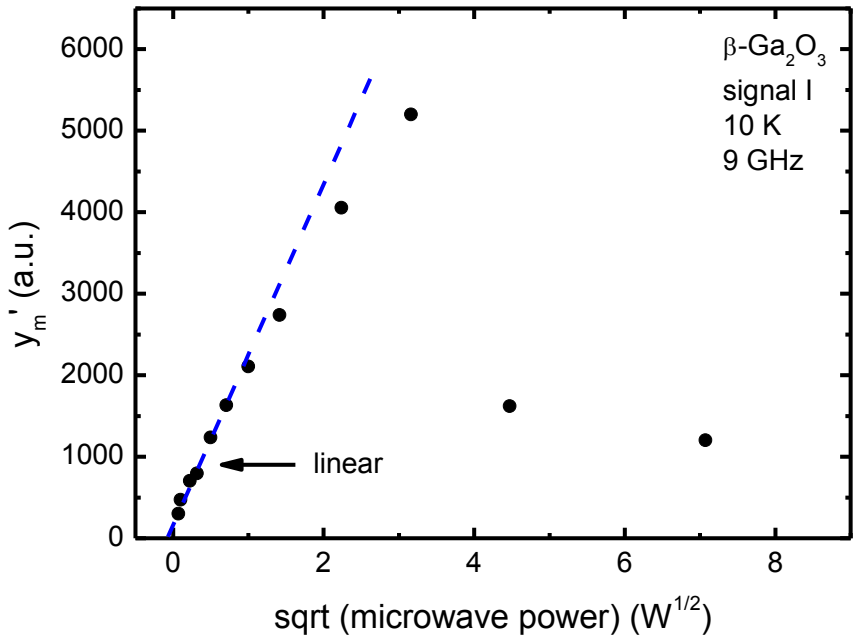

Figure 5.10: The peak-to-peak amplitude y_m' of signal I in β-Ga_2O_3 is plotted as a function of the square root of the microwave power P. The measurements were performed at 10 K. The dashed blue line indicates a linear behavior.

The calculations of T_1 and T_2 are performed in the same manner as described in chapter 3.2.2. This yields $T_1 = 9.5 \cdot 10^{-6}\ s$ for the spin-lattice relaxation time of signal I in β-Ga_2O_3. For the spin-spin relaxation time one obtains $T_2 = 3.6 \cdot 10^{-9}\ s$. However, it was not possible to follow the temperature dependence of the relaxation of signal I, since it already vanished at 35 K and the peak-to-peak intensity decreased fast with increasing temperature.

Signal II

A detailed EPR spectrum of signal II measured at 4 K is depicted in Figure 5.11. The line width ΔB and the peak-to-peak intensity ΔI are indicated by black arrows. Signal II consists of one line with a line width ΔB of 40 Gauss. The signal is stable up to room temperature and the EPR signal intensity is only decreasing by a factor of 10 from 4 K up to room temperature. Due to the high thermal stability coming along with low changes of the EPR signal intensity, it was not possible to calculate a reliable activation energy value for signal II. The line width is constant over the complete temperature range.

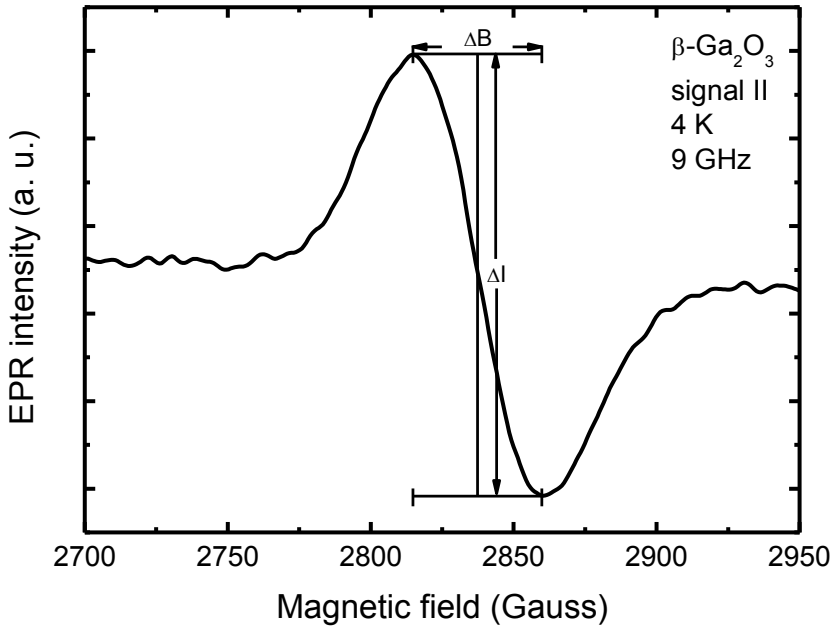

Figure 5.11: Detailed EPR spectrum of signal II measured at 4 K. The line width ΔB and the peak-to-peak intensity ΔI are indicated by black arrows.

In Figure 5.12 the peak-to-peak amplitude of signal II is plotted versus the square root of the microwave power. For low microwave powers a linear behavior between the peak-to-peak amplitude and the square root of the microwave power can be observed (indicated by a dashed blue line). The maximum peak-to-peak amplitude is reached for a microwave power of 10 mW. After that value saturation occurs. The calculations of

T_1 and T_2 are performed in the same manner as described above. This yields $T_1 = 1 \cdot 10^{-4}\ s$ for the spin-lattice relaxation time of signal I in β-Ga_2O_3. For the spin-spin relaxation time one obtains $T_2 = 2.6 \cdot 10^{-9}\ s$.

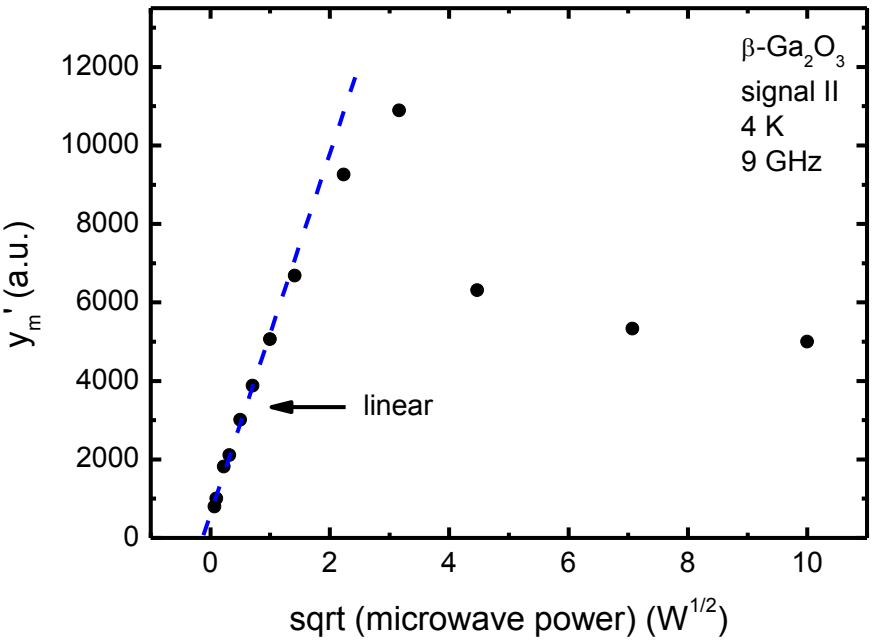

Figure 5.12: The peak-to-peak amplitude y_m' of signal II in β-Ga_2O_3 is plotted as a function of the square root of the microwave power P. The measurements were performed at 10 K. The dashed blue line indicates a linear behavior.

The temperature dependence of the spin-spin-relaxation time can be estimated by the temperature dependence of ΔB_{pp}^0 which is given by [64]:

$$\Delta B_{pp}^0 = \frac{2}{\sqrt{3}\gamma T_2} \tag{5.4}$$

However, the line width is constant over the whole temperature range and therefore T_2 is also constant from 4 K up to room temperature. The spin-lattice relaxation time T_1 is connected to the EPR line width by equation (3.4):

$$T_1 = 1.97 \cdot 10^{-7} \frac{\Delta H_{pp}^0}{g B_1^2}$$

One can see that for a temperature independent EPR line width the spin-lattice relaxation time T_1 remains constant, too.

The angular dependence of signal II was studied in order to obtain the g-values of the defect and information on its orientation towards the crystal axes. Therefore the sample was rotated around the b-axis of the β-Ga_2O_3 crystal by 240° in 5° steps. The measurement was started from a position with the a-axis of the crystal parallel to the magnetic field. The results of these measurements performed at 10 K are shown in Figure 5.13. The magnetic field position of signal II is plotted versus the rotation angle, whereas the perpendicular and parallel orientations of the a-axis towards the magnetic field are indicated by vertical dashed lines.

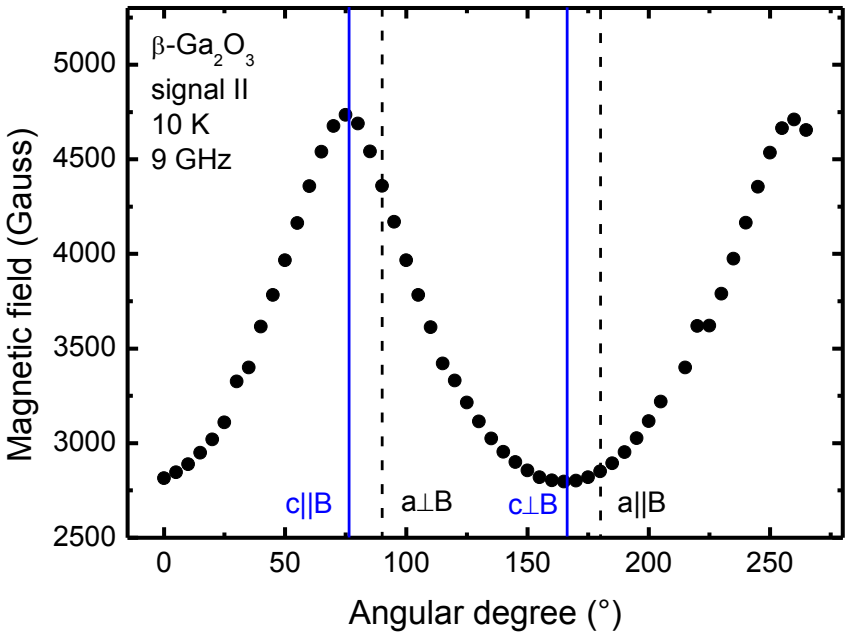

Figure 5.13: Angular dependent magnetic field position of signal II measured at 10 K. The orientations of the c-axis (solid blue lines) and the a-axis (dashed black lines) of the crystal towards the magnetic field are indicated by vertical lines.

One can see that in this case the minimum and maximum magnetic field position values are not correlated to the a-axis of the β-Ga_2O_3 crystal. There is a deviation from the position of the a-axis which equals exactly the difference between an orientation perpendicular to the a-axis and parallel to the c-axis of β-Ga_2O_3. The orientations parallel and perpendicular to the c-axis are indicated by solid blue lines. Hence according to signal II, the defect is aligned along the c-axis of β-Ga_2O_3. The g-values are determined to the following:

$$g_{c\|B} = 1.43 \text{ and } g_{c\perp B} = 2.41$$

Signal III

A detailed EPR spectrum of signal III measured at 100 K is depicted in Figure 5.14. The line width ΔB and the peak-to-peak intensity ΔI are indicated by black arrows. The S=½ EPR signal is very sharp with a line width of 5 Gauss. Due to the g-value of 1.96, the signal can be classified as a shallow donor.

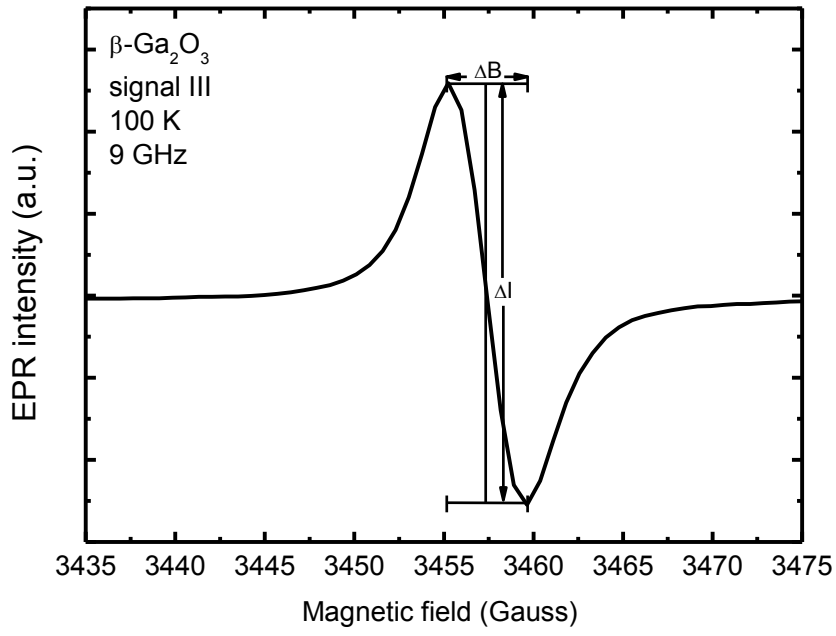

Figure 5.14: Detailed EPR spectrum of signal III measured at 100 K. The line width ΔB and the peak-to-peak intensity ΔI are indicated by black arrows.

An EPR signal in β-Ga_2O_3 with very similar properties is known from the literature, it is attributed to an oxygen vacancy (V_O) [51]. The small deviation of the g-value from the free electron g-value is caused by spin-orbit coupling due to a slight contribution from gallium 4p orbitals to the bottom of the conduction band.

The dependence of the β-Ga_2O_3 shallow donor signal on the microwave power was also investigated to assure that the results of the EPR measurements are not influenced by saturation effects. Also the relaxation times can be derived from these measurements using equations (3.2) to (3.6).

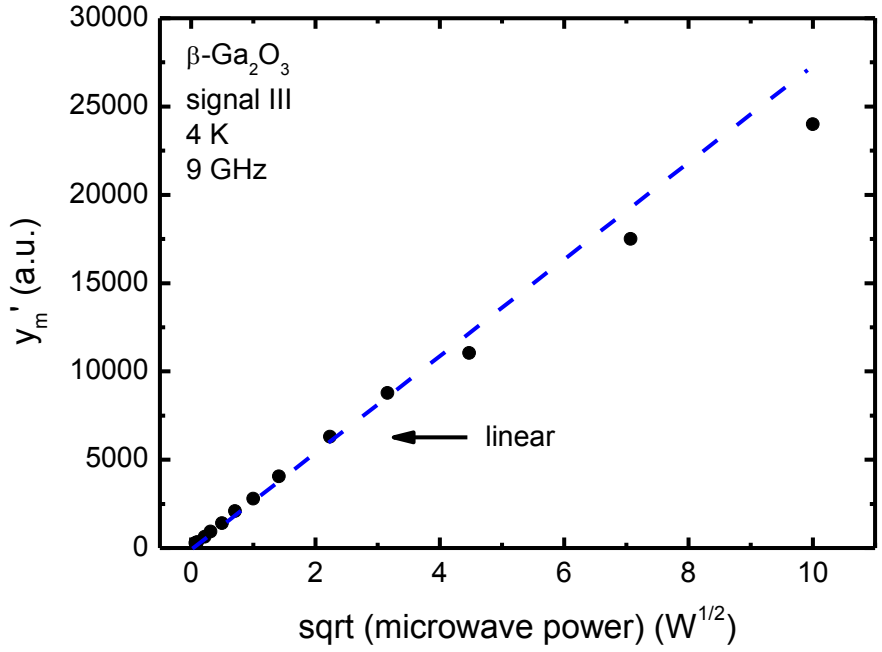

Figure 5.15: The peak-to-peak amplitude y_m' of signal III in β-Ga_2O_3 is plotted as a function of the square root of the microwave power P. The measurements were performed at 4 K. The dashed blue line indicates a linear behavior.

Figure 5.15 shows the dependence of the peak-to-peak intensity of signal III on the square root of the microwave power measured at a temperature of 4 K. The EPR signal intensity linearly increases with increasing microwave power, as indicated by the

dashed blue line in Figure 5.15, hence no saturation occurs. While this behavior makes it easy to choose the right microwave power for the measurements, it leads to the situation that it is not possible to derive the relaxation times with the saturation method described in the chapter before.

The temperature dependence of signal III was measured in order to determine the thermal activation energy. Therefore the EPR intensity of signal III was plotted versus the temperature (see Figure 5.16).

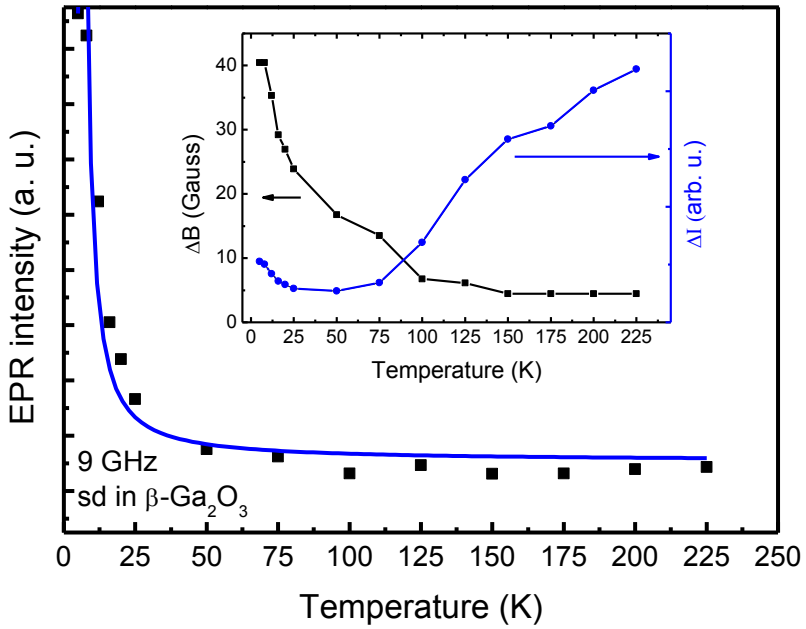

Figure 5.16: Temperature dependency of signal III. The best fitting parameters for equation (5.3) are indicated by the blue curve. In the inset the dependencies of the line width ΔB and the peak-to-peak intensity ΔI are depicted.

To calculate the activation energy the curve was fitted with the following equation:

$$I = I_0 \cdot e^{\frac{E_a}{k_B \cdot T}} \tag{5.5}$$

With the activation energy E_a and the Boltzmann constant k_B.

The best fitting parameters are indicated by the blue line in Figure 5.15 and yield an activation energy E_a = 38 meV. This value is in good agreement with the shallow donor ionization energy of 20 – 40 meV for β-Ga_2O_3 determined by Lorenz et al. and Binet et al. [50, 51].

Signal III is observable up to room temperature. In the inset of Figure 5.16 are the dependencies of the EPR line width ΔB and the peak-to-peak intensity ΔI of signal III on the temperature shown. The peak-to-peak intensity decreases from 4 K up to 25 K and beyond 25 K ΔI increases with increasing temperature. The line width decreases with increasing temperature and reaches a constant value of approximately 5 Gauss at 150 K.

5.2.5 Discussion

The characterization of a Czochralski grown β-Ga_2O_3 crystal reveals 3 defects from the EPR measurements. Signal I consist of 8 equidistant lines (I = 7/2) with the spin-Hamilton parameters $g_{a\|B} = 6.4$, $g_{a\perp B} \approx 2.8$, $A_{a\|B} = 62\ Gauss$ and $A_{a\perp B} \approx 107\ Gauss$. It can be observed for temperatures up to 35 K and is orientated along the a-axis of the β-Ga_2O_3 crystal. Only the elements scandium (Sc), vanadium (V), cobalt (Co), holmium (Ho) and tantalum (Ta) are known from the periodic table which fulfill the requirements. Sc^{2+} has a $3d^1$ electron configuration and g-values of $g_{\|} = 1.94$ and $g_{\perp} = 1.98$ can be found in the literature [5]. These values are very different from the experimental data, therefore scandium can be excluded. V^{2+} in the $3d^3$ electron configuration can also be neglected due to its g-value of 1.98 [5]. Holmium in the 2+ and 3+ charge state has a very large hyperfine splitting, as observed by Boyn et al. [65] and Shakurov et al. [66], what differs significantly from the hyperfine splitting observed for this center. In case of tantalum only little information on EPR data is available. Irmscher et al. observed a center in EPR they labeled as Ta^{3+} which shows a g-value around 2 and has a very large nuclear quadrupole moment what is not the case for signal I [67]. The last element to consider is Co^{2+} with a $(3d^7)$ $^4F_{9/2}$ electronic ground state configuration. Cobalt has a nuclear spin I = 7/2 with 100% natural abundance. If one assumes a purely octahedral crystal field, the lowest orbital state is a

triplet (labeled as Γ_4). That is split by means of spin-orbit splitting consisting of three orbitally degenerated states each with a fourfold spin degeneracy. In the model given by Abragam and Pryce [68] these 12 levels split, in zero magnetic field, into a doublet, a quadruplet and a sextet, where the doublet is lying lowest. Resonance can be only observed for the lowest doublet. The evaluation of the Zeeman effect within this doublet using the spin-Hamilton operator $\tilde{g}_l \boldsymbol{l} + g_s \boldsymbol{S}$ yields the isotropic $\tilde{g}$-factor [5]:

$$\tilde{g} = \frac{5}{3} g_s - \frac{2}{3} \tilde{g}_l \tag{5.6}$$

This results in S = ½ EPR signals with $g \sim 4.3$ and $A \sim 0.01\ cm^{-1}$ [3]. Due to the presence of a large amount of orbital angular momentum in the Γ_4 triplet, there is a large deviation of the ground state g-factor from the free electron value of 2.00232. However, the most cobaltous salts show very high anisotropy, in the case of octahedral coordination the g-values are $g_\perp = 2.95$ and $g_\parallel = 6.24$ (see Abragam and Bleaney [5] or Pilbrow [3]). That behavior is caused by small trigonal or tetragonal distortions of the octahedron. One can describe this effect by adding terms to the energy matrices what results in a splitting of the quadruplet and sextet. The parallel and perpendicular g-values are then given by [3]:

$$g_\parallel = \frac{5}{3} g_s - \frac{2}{3} \tilde{g}_l + \left(\frac{4\sqrt{5}a}{3} \right) (2g_s - \tilde{g}_l) \tag{5.7}$$

$$g_\perp = \frac{5}{3} g_s - \frac{2}{3} \tilde{g}_l - \left(\frac{2\sqrt{5}a}{3} \right) (2g_s - \tilde{g}_l) \tag{5.8}$$

Here g_s describes the electron spin g-factor which equals 2. The effective orbital g-factor $\tilde{g}_l$ equals -3/2 for the triplet orbital ground state with a fictitious angular momentum $\tilde{l} = 1$. The parameter a is a measure of the distortion and small compared to unity. From the experimental $g_\parallel$-value the distortion parameter a was calculated to 0.23 using equation (5.7) what is in agreement with the values for several cobaltous salts showing a value of 0.2 [5]. The g-factors follow roughly the relation:

$$g_\parallel + 2g_\perp \approx 5g_s - 2\tilde{g}_l \approx 13$$

In this case a value of 12 is achieved what is quite close to the model.

Cobalt on the tetrahedral gallium site is less likely due to nearly isotropic g- values around 2.4 [3, 5]. Therefore signal I can most likely be assigned to Co^{2+} located on the octahedral gallium site (0.62 Å lattice space). This position seems more preferable compared to the tetrahedral gallium site (0.477 Å lattice space), since there is more space for the Co^{2+} (0.75 Å ion radius) which has a larger ion radius compared to the Ga^{3+} ion radius of 0.62 Å.

Signal II consists of one line and can be observed from 4 K up to room temperature. A further identification of the defect is difficult, since no fine structure or hyperfine structure could be observed. The g-values $g_{c\|B} = 1.43$ and $g_{c\perp B} = 2.41$ are observed for the center which is orientated along the c-axis of the β-Ga_2O_3 crystal. A similar defect in Czochralski grown β-Ga_2O_3 crystals with the same angular behavior is observed by Galazka et al. [69]. They associated the EPR signal with native defects like oxygen vacancies, but gave no further explanation. However, it is a very uncommon behavior that the g-value crosses the border of g = 2 due to anisotropy. Such a behavior was only observed for transition metal ions. Cu^{2+} in tetrahedral symmetry was observed in hexagonal BeO by de Wit et al. and showed such a behavior with $g_{\|} = 1.7$ and $g_{\perp} = 2.38$ [70]. Fourfold coordinated Co^{2+} shows also such a g-value behavior [3, 5]. A further connection to cobalt is given by the similarity of the spin-spin relaxation times of signal I and signal II. The relaxation times remain constant over the complete temperature range, since the EPR line width does not change with temperature. This behavior is not unexpected since signal II has a high thermal stability.

Signal III can be attributed to an oxygen vacancy (V_O) shallow donor with an activation energy of 38 meV. Binet et al. [51] observed a very similar defect in β-Ga_2O_3 which was attributed to conduction band electrons located in a (V_O) donor impurity band. They support this model by the temperature dependence of the DC-conductivity, which varies only slightly from 4 K up to 300 K. Further the spin-lattice relaxation time shows the same temperature behavior as the conductivity [64]. That behavior is typical for free electron spins relaxing via the Elliot mechanism [71]. The defect observed in this work has the same small line widths for temperatures above 100 K, below 100 K the EPR signals are much broader (see the inset of Figure 5.16).

However, in the graphs shown by Binet et al. [51] a similar behavior of the temperature dependence of the line width can be observed when compared to signal III in this work. For low temperatures (20K) the line width is 10 Gauss and it decreases to 2 Gauss with increasing temperature. The same line width behavior of the conduction band electrons in β-Ga_2O_3 was presented by Vincent et al. [72]. Therefore, signal III can most likely be attributed to conduction band electrons, located in an oxygen vacancy impurity band. Another indicator is given by the fact that signal III can be observed for temperatures up to 300 K. That is quite unusual for shallow donors, since the thermal energy is high enough to lift the electron from the donor state to the conduction band and therefore charge the defect into a non-paramagnetic state. In addition the microwave power dependent saturation behavior of signal III is quite uncommon for shallow donor EPR signals. The microwave power dependence for shallow donors would appear with an apparent saturation behavior like the ones for signal I and signal II (see for instance Figure 5.10 of Figure 5.12). The behavior observed in this case is characteristic for delocalized electrons.

5.3 Ammonolysis of Gallium Oxide powder

A common way to synthesize Gallium Nitride (α-GaN) is the ammonolysis of Gallium Oxide (β-Ga_2O_3). It is described by the following reaction:

$$Ga_2O_3 + 2NH_3 \rightarrow 2GaN + 3H_2O \tag{5.9}$$

The process is performed by flowing ammonia over β-Ga_2O_3 powder in a temperature regime ranging from 600 °C to 1100 °C [73, 74]. To study the effect of the ammonolysis at elevated temperatures for different times a set of 4 commercially available β-Ga_2O_3 powder samples was first caked for 3 days at 1250 °C and afterwards treated with ammonia at 780 °C for 5, 18, 30 and 120 minutes. One sample was kept untreated as reference. The ammonolysis was performed in the group of Prof. Martin at the RWTH Aachen.

The samples were investigated by Electron Paramagnetic Resonance (EPR) in order to find traces of nitrogen incorporated in the β-Ga_2O_3 powder after short nitridation times.

5.3.1 EPR measurements

A Bruker ESP 300E spectrometer, described in detail in the appendix, was used for the EPR measurements. A representative overview spectrum of the nitridated β-Ga_2O_3 powder samples measured at 15 K is shown in Figure 5.17, in this case the sample treated for 5min with ammonia was taken. All the features found in this spectrum were observed for the other samples, too, albeit with different EPR signal intensities. One can see 4 EPR signals marked as A, B, C and D. The spectrum is depicted in two parts for a better overview, whereby the EPR signal intensities on the high field side of the spectrum were multiplied by a factor of 10 since the intensity of signal D is very high compared to the other ones. Signal A consists of 2 signals with a further structure superimposed to them. The origin of these signals will be discussed further below together with a detailed EPR spectrum.

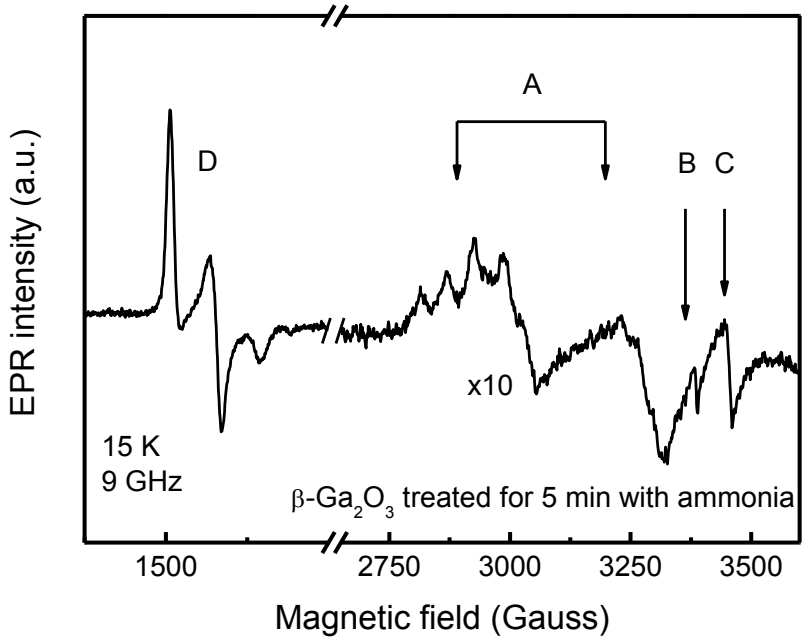

Figure 5.17: EPR overview spectrum measured at 15 K of a β-Ga_2O_3 powder sample treated with ammonia for 5 min at a temperature of 780 °C. There are 4 EPR signals marked as A, B, C and D. The part on the right side of the EPR spectrum was multiplied by a factor of 10.

The EPR signal marked as B is located at a g-value of 2.002 and consists of only one single line, hence it is a S = ½ defect. This defect can be assigned to surface dangling bonds because the g-value equals the free electron g-value [75]. There is another signal with S = ½ marked as C, at a g-value of 1.96. This defect is well known from the literature and can be attributed to free electrons located in an oxygen vacancy donor impurity band [51, 76]. Signal D can be ascribed to Fe^{3+} with the following spin Hamilton parameters S = 5/2, g = 2.0043, D = 0.2212 cm^{-1} and E = 0.06965 cm^{-1} [77, 78].

For the measurement of a more detailed EPR spectrum of signal A the sample with the largest EPR signal intensity, i.e. the untreated β-Ga_2O_3 powder reference sample, was chosen. 20 measurements taken at 15 K were accumulated to further increase the signal intensity. The results of these measurements are shown in Figure 5.18 (a). In the EPR powder spectrum one can observe 2 groups of signals, each consisting of 4 EPR transitions at g-values of 2.4 and 2.08 (indicated by the black rakes). These g-values are characteristic for acceptor centers. The 4 lines are caused by a hyperfine interaction with a nuclear spin I = 3/2, since the distance between them is too small for a fine-structure splitting. The possible candidates with a nuclear spin of 3/2 are the group I elements Li, Na and K as well as Ga, As and Cu. However, on the low field side of the spectrum another group with 4 lines can be observed (indicated by the blue rake). It is superimposed to the first group of signals at g = 2.4. The intensities of these EPR signals are smaller and cannot be resolved in case of the second group at g = 2.08. A possible explanation for these signals could be the presence of an element with 2 isotopes and a nuclear spin I = 3/2. By comparing the signal intensities from both groups the isotope ratio can be estimated. The calculation yields 71 % for the signals marked by a black rake and 29 % for the other ones. Figure 5.18 (b) shows a simulated EPR powder spectrum of a defect with I = 3/2 with the following simulation parameters:

$$g_{\parallel} = 2.08,\ g_{\perp} = 2.4,\ A_{\parallel} = 200\,MHz \text{ and } A_{\perp} = 184\,MHz$$

The simulation describes the experimental data of 2 groups with each 4 lines (indicated by the black rakes) quite well.

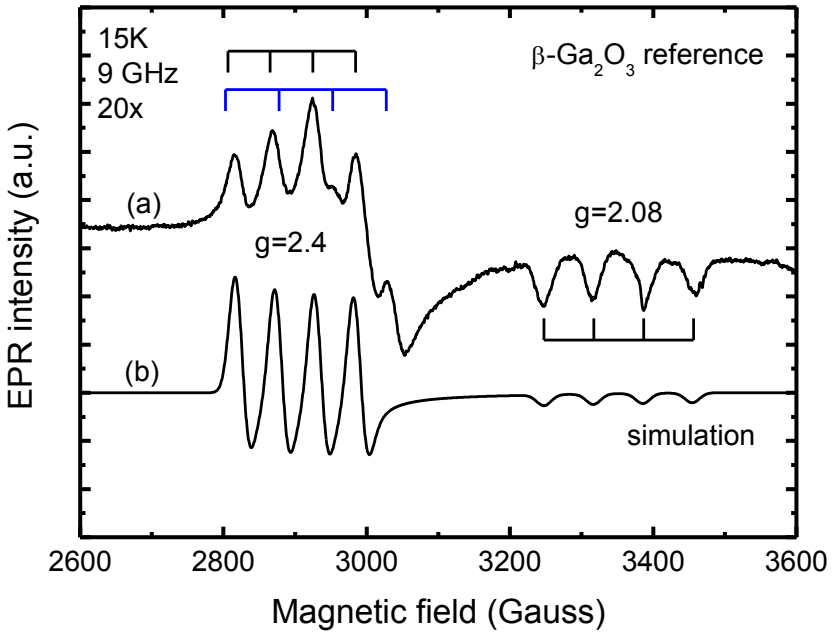

Figure 5.18: Detailed EPR spectrum of signal A of the β-Ga_2O_3 powder reference sample (a). The measurement was taken at 15 K and repeated 20 times to increase the signal intensity. Below, a simulated powder spectrum for an S = ½, I = 3/2 defect is depicted (b).

For the group of signals marked by the blue rake the spin-Hamilton parameters can be estimated to $g_\perp = 2.38$ and $A_\perp = 246\ MHz$. For the EPR signal group at g = 2.08 it was not possible to observe any differences to the first group marked by the black rakes. Therefore, the same values as used for the EPR signal group with 71 % natural abundance were used for the EPR signals with 29 % natural abundance. A simulated powder spectrum for an S = ½ defect with I = 3/2 and the natural abundances of 71 % and 29 % using the spin-Hamilton parameters given for the EPR signals mentioned above is depicted in Figure 5.19 (b). The simulation fits the positions of the EPR signals shown in Figure 5.19 (a) quite well.

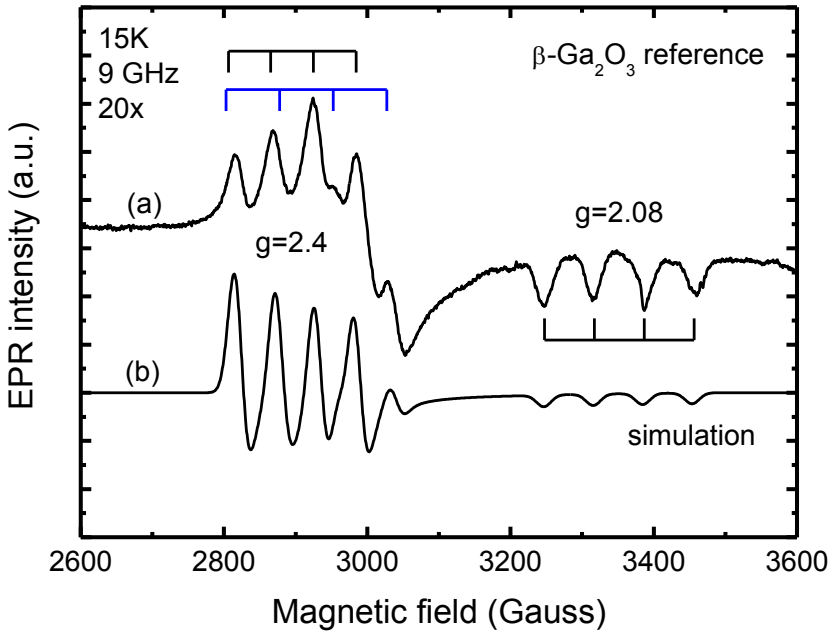

Figure 5.19: Detailed EPR spectrum of signal A of the β-Ga_2O_3 powder reference sample (a). The measurement was taken at 15 K and repeated 20 times to increase the signal intensity. Below, a simulated powder spectrum for an S=½ defect with I=3/2 (71 % and 29 % natural abundances) is depicted (b).

After all the defects observed in the samples have been described, it is time to study the effect of the ammonolysis on the β-Ga_2O_3 powder. For this purpose, the EPR intensities of signal A (depicted by black dots) and signal C (indicated by blue triangles) have been tracked over the nitration time (see Figure 5.20). The measurements were performed at 4 K. With increasing nitridation time the EPR intensity of signal A decreases, whereas the EPR intensity of signal C increases with increasing nitridation time. However, the intensity of signal B is not correlated to the nitration time.

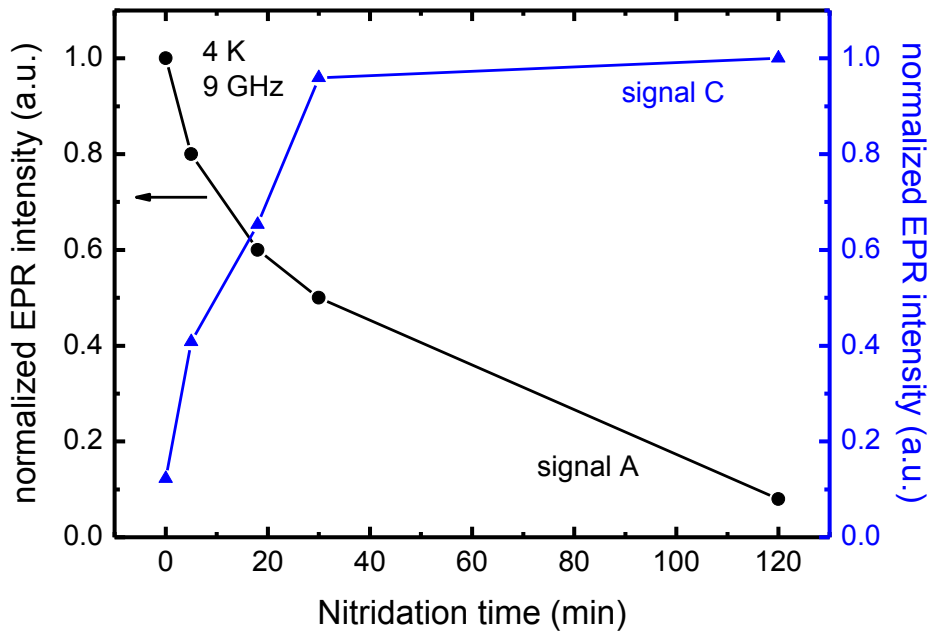

Figure 5.20: Dependence of the EPR intensities of signal A and signal B on the nitridation time measured at 4 K.

5.3.2 Discussion

A set of 4 β-Ga_2O_3 powder samples was nitridated for up to 2 hours at 780 °C and characterized by EPR spectroscopy. Before and after the ammonolysis Fe^{3+} could be found as a residual impurity. This can be explained by the impurity of the gallium used for the preparation of the gallium oxide. Possible origins of signal A are lithium, sodium, potassium, gallium, arsenic and copper, which all fulfill the prerequisite of a nuclear spin I = 3/2. However, the neutral group I elements Li, Na and K all have s-type electron wave functions, which leads to nearly isotropic g-values near the free electron g-value of 2. Hence, the group I elements can be excluded as possible origins of signal A. Gallium has two isotopes with a nuclear spin I =3/2 (^{69}Ga with 60.1 % natural abundance and ^{71}Ga with 39.9 % natural abundance). The presence of Ga could explain the second group of signals at g = 2.4, but the isotope ratio of gallium does not match the experimentally observed isotope ratio (71 % and 29 %). Ga^{2+} as well as Ga^{4+} are the possible charge states for an acceptor in gallium oxide. The electron

configuration of Ga^{2+} would be an $4s^1$ state with g~2, see for instance gallium interstitials in GaAs [79]. Ga^{4+} would be detected by EPR spectroscopy as a hole in a gallium bond; it would require a thermal or optical excitation and a distant defect to compensate the charge. However, the EPR experiment was performed in thermal equilibrium and recharging of the defects was not noticed. Thus gallium, both in the fourfold or in the twofold positive charged state, can also be excluded as the origin of signal A. As^0 would be located in the oxygen sub lattice and has a nuclear spin I = 3/2 with 100 % natural abundance. The electron configuration is $3p^5$ with $g_{\parallel} \leq 2.002$ and $g_{\perp} > 2$ [80], which is in conflict with the experimental data. Furthermore the As^0 acceptors would be compensated by shallow donors and therefore could not be observed in EPR spectroscopy under equilibrium conditions. The last candidate is Cu^{2+} with a $3d^9$ electron configuration located in the gallium sub lattice. The isotopes are ^{63}Cu (69.2 % natural abundance) and ^{65}Cu (30.8 % natural abundance). These isotopic abundances are in quite good coincidence with the experimental data of the isotope ratio (72 % and 28%). One possible location for the Cu^{2+} ion is the tetrahedral gallium position. However, in this case the g-values should be similar to the g-values of Cu^{2+} in GaN or in ZnO ($g_{\parallel} \leq 0.7$ and $g_{\perp}$~1.5) [22, 81] and thus very different to the g-values observed for the center in this experiment. On the other hand, Cu^{2+} located at the octahedral site shows g-values ($g_{\parallel}$~2.4 and $g_{\perp}$~2.1) very similar to the ones obtained from the experimental data, see e.g. Abragam and Bleaney ($3d^9$ Cu^{2+} in an octahedral field) [5] or Keeble et al. (Cu^{2+} in $PbTiO_3$) [82]. Thus, signal A can most likely be assigned to Cu^{2+} located on the octahedral gallium site.

During the ammonolysis, the EPR intensities of signal A and signal C change with time. The EPR intensity of the shallow donor (signal C) increases with increasing nitridation time. Due to the reducing effect of the ammonia, oxygen vacancies (V_O) acting as shallow donors are created. The increasing number of shallow donors causes the acceptors to be more and more compensated with increasing nitridation time, which leads to the decrease of the Cu^{2+} acceptor signal.

6 Summary

In this thesis the material systems zinc oxide, aluminum nitride and gallium oxide were investigated by electron paramagnetic resonance and optical spectroscopy in order to gain insight into the point defects in these materials which are affecting the optical and electrical properties.

For a long time doping with nitrogen was thought to be the best possibility to create p-type conducting ZnO. However, recently there were doubts whether nitrogen forms a shallow acceptor or not. That acceptor level and the corresponding photo-transition process were characterized by EPR and photo-EPR. The photo-transition process charging the nitrogen acceptor from the negative charged non-paramagnetic state into the neutral paramagnetic, was found to be a direct process to the conduction band with an optical ionization energy E_{opt} = 2.1 eV. Therefore, it was proven, that the defect caused by a nitrogen atom substituting an oxygen atom in ZnO, forms a deep acceptor level.

The characterization of aluminum nitride bulk crystals by EPR reveals two defects, a donor and an acceptor. The donor which originates most likely from an oxygen atom substituting a nitrogen atom has a negative U-behavior and forms a DX^- center. The optical ionization energy of the DX^- center was determined to 1.9 eV and the formation energy was estimated to 3 meV. A (V_{Al}-O_N) defect complex is most likely the origin of the acceptor observed in the EPR measurements. The presence of (V_{Al}) and (O_N) is confirmed by optical spectroscopy and further the formation of (V_{Al}-O_N) defect complexes is thermodynamically favored over the isolated defects. The energy level position is estimated to be 1.1 eV to 3.5 eV above the valence band.

Transition metal ions are often incorporated in semiconductors as residual impurities and form deep level defects. In the case of gallium oxide two 3d transitions metals could be identified by EPR. Co^{2+} with a $3d^7$ electron configuration, located at an octahedral gallium lattice site, could be identified in bulk crystals due to its strong anisotropic g-values and its hyperfine interaction. In β-Ga_2O_3 powder Cu^{2+} with a $3d^9$ electron configuration, the isotopes ^{63}Cu (69.2 % natural abundance) and ^{65}Cu (30.8 % natural abundance), located on an octahedral gallium site, could be identified.

Appendix

A Zink Oxide

Zinc oxide (ZnO) is an II-VI compound semiconductor crystallizing in the wurtzite, zinc blende, and rocksalt structures. For ambient conditions, the thermodynamically stable phase is the wurtzite structure. ZnO in the zinc blende structure can be stabilized only by growth on cubic substrates, and the rocksalt NaCl structure may be obtained at relatively high pressures [83]. In the hexagonal wurtzite structure with the $P6_3mc$ space group each anion is surrounded by four cations at the corners of a tetrahedron, and vice versa (Figure A.1). That tetrahedral coordination is typical for sp3 covalent bonding, but materials with this structure also have a substantial ionic character. In the case of ZnO the ionicity is located at the borderline between covalent and ionic semiconductors. ZnO has the lattice parameters a = 0.52042 nm and c = 0.32496nm [84]. The c/a ratio of ZnO is 1.6018, whereas the c/a ratio of an ideal wurtzite structure equals 1.633 [83]. Therefore, the tetrahedral structure is distorted.

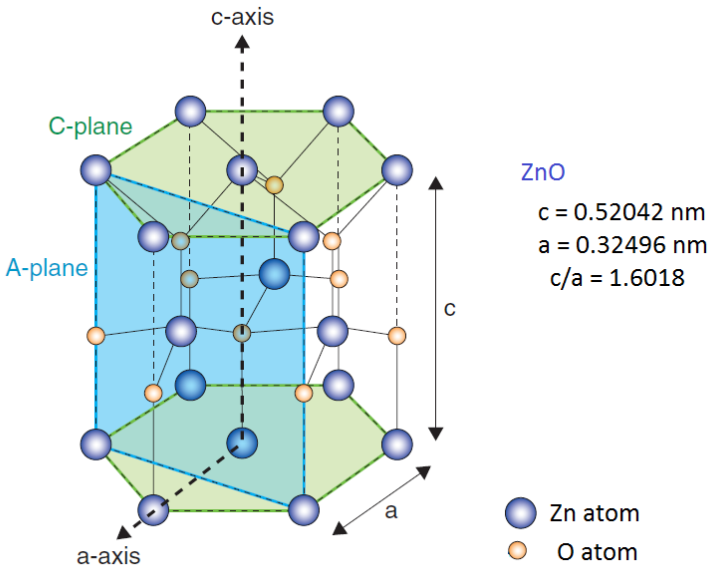

Figure A.1: Hexagonal wurtzite crystal structure of ZnO after [85].

Currently, the three main methods used for the growth of ZnO bulk crystals are high pressure melt, hydrothermal, and chemical vapor transport [83]. Each of these methods has advantages and limitations on their own. In general, it is important to know how a crystal was grown, since this knowledge provides information on the relative types of point defects that may be present. A comprehensive review paper on ZnO, also going into the details of ZnO bulk single-crystal growth techniques, has been published by Ozgur et al [83].

A summary of the spin-Hamilton parameters of known donors and acceptors in ZnO is given in Table A.1. The spin-Hamilton parameters of the 3d transition metals are summarized on their own in Table A.2.

Table A.1: Spin-Hamilton parameters of donors and acceptors in ZnO

Center	Electron spin g-factor	Hyperfine interaction	Fine structure	Reference
Shallow donor (S = 1/2)	$g_{\parallel} = 1.955$ $g_{\perp} = 1.953$	Not observed		[86]
Shallow donor (S = 1/2)	$g_{\parallel} = 1.957$ $g_{\perp} = 1.956$	Not observed		[87]
Shallow halogen donor (S = 1/2)	g = 1.956	Not observed		[87]
Shallow In donor (S = 1/2)	$g_{\parallel} = 1.957$ $g_{\perp} = 1.956$	A(^{115}In) = 36.6 G		[88, 89]
Shallow Ga donor (S = 1/2)	$g_{\parallel} = 1.957$ $g_{\perp} = 1.956$	A(^{69}Ga) = 4.2 G A(^{69}Ga, ^{72}Ga) = 6.7 G		[88] [16]
Shallow Al donor (S = 1/2)	g = 1.9595	A(^{27}Al) = 1.45 MHz		[90]
Shallow H donor (S = 1/2)	$g_{\parallel} = 1.9569$ $g_{\perp} = 1.9552$	A(^{1}H) = 1.4 MHz		[91]
Shallow Zn interstitial (S = 1/2)	$g_{\parallel} = 1.9605$ $g_{\perp} = 1.9595$	Not observed		[92]

Table A.1 continued

Center	Electron spin g-factor	Hyperfine interaction	Fine structure	Reference
Oxygen vacancy F^+ (S = 1/2)	$g_{\parallel}$ = 1.9945 $g_{\perp}$ = 1.9960	Axial: $A_{\parallel}$ = 57.34 MHz $A_{\perp}$ = 42.3 MHz Non-axial: A_{xx} = 76.6 MHz A_{yy} = 75.9 MHz A_{zz} = 94.8 MHz		[93, 94]
Oxygen vacancy (S = 1)	$g_{\parallel}$ = 1.984 $g_{\perp}$ = 2.025	Not observed	D = 0.026 cm^{-1}	[25]
Zinc vacancy related (S = 1/2)	g_{xx} = 1.927 g_{yy} = 1.952 g_{zz} = 1.853	Not observed		[95]
Zinc vacancy related (S = 1)	g_{xx} = 1.927 g_{yy} = 1.952 g_{zz} = 1.853	Not observed	|D| = 1465 MHz |E| = 58 MHz	[95]
Deep Li acceptor (S = 1/2)	Axial: $g_{\parallel}$ = 2.0028 $g_{\perp}$ = 2.0253 Non-axial: g_{xx} = 2.0223 g_{yy} = 2.0254 g_{zz} = 2.0040	Axial: $A_{\parallel}$ = 0.61 MHz $A_{\perp}$ = 5.12 MHz Non-axial: A_{xx} = 5.1 MHz A_{yy} = 5.1 MHz A_{zz} = 0.81 MHz		[96]
Deep Na acceptor (S = 1/2)	Axial: $g_{\parallel}$ = 2.0029 $g_{\perp}$ = 2.0315 Non-axial: g_{xx} = 2.0250 g_{yy} = 2.0309 g_{zz} = 2.0036	Axial: $A_{\parallel}$ = 8.1 MHz $A_{\perp}$ = 4.49 MHz Non-axial: A_{xx} = 4.57 MHz A_{yy} = 4.04 MHz A_{zz} = 11.64 MHz		[97]
Deep N acceptor (S = 1/2)	$g_{\parallel}$ = 1.9953 $g_{\perp}$ = 1.9633	$A_{\parallel}$ = 81.3 MHz $A_{\perp}$ = 9.5 MHz		[16-18]
N_2^- acceptor (S = 1/2)	$g_{\parallel}$ = 2.0036 $g_{\perp}$ = 1.9935	$A_{\parallel}$ = 9.8 MHz $A_{\perp}$ = 20.1 MHz		[18, 98]
$(Zn_i^+ - N_O^-)$ (S = 1/2)	$g_{\parallel}$ = 2.020 $g_{\perp}$ = 2.006	Not observed		[99]

Table A.2: Spin-Hamilton parameters of 3d transition metals in ZnO

Center	Electron spin g-factor	Hyperfine interaction	Fine structure	Reference
V^{3+} (S = 1/2)	$g_{\parallel} = 1.945$ $g_{\perp} = 1.937$	$\|A_{\parallel}\| = 68x10^{-4}$ cm^{-1} $\|A_{\perp}\| = 93x10^{-4}$ cm^{-1}	$\|D\| = 0.075$ cm^{-1}	[100]
Ni^{3+} (S = 1/2)	$g_{\parallel} = 2.143$ $g_{\perp} = 4.318$	Not observed		[101]
Fe^{3+} (S = 5/2)	g = 2.0060	$\|A\| = 9.02x10^{-4}$ cm^{-1}	D = -0.0594 cm^{-1} F = 0.0004 cm^{-1} a = 0.0039 cm^{-1}	[102]
Mn^{2+} (S = 5/2)	g = 2.016	A = -76x10^{-4} cm^{-1}	D = -0.0217 cm^{-1}	[103]
Co^{2+} (S = 1/2)	$g_{\parallel} = 2.25$ $g_{\perp} = 4.55$	$A_{\parallel} = 15.3$ G $A_{\perp} = 2.8$ G		[104]
Cu^{2+} (S = 1/2)	$g_{\parallel} = 0.74$ $g_{\perp} = 1.53$	$\|A_{\parallel}\| = 195x10^{-4}$ cm^{-1} $\|A_{\perp}\| = 231x10^{-4}$ cm^{-1}		[105]

B Aluminum Nitride

Aluminum nitride (AlN) is an III-V compound semiconductor crystallizing in the wurtzite structure with the $P6_3mc$ space group under normal pressure. For high pressures (P > 17 GPa) it transforms to the rocksalt structure (Fm3m space group) and becomes metastable at ambient pressure [106].

The wurtzite structure of AlN is hexagonal with four atoms surrounding a lattice site in form of a distorted tetrahedron. Three equivalent neighboring atoms are located in the basal plane, while the fourth one with a different bond length defines the c-axis of the crystal. The crystal structure of AlN is depicted in Figure B.1. One can see that each aluminum atom is surrounded by four nitrogen atoms forming a distorted tetrahedron around the aluminum atom. In the same manner the nitrogen atoms are surrounded by aluminum atoms. AlN has the lattice parameters a = 0.4982 nm and c = 0.3112 nm [85]. The c/a ratio of AlN is 1.600, whereas the c/a ratio of an ideal wurtzite structure equals 1.633 [83].

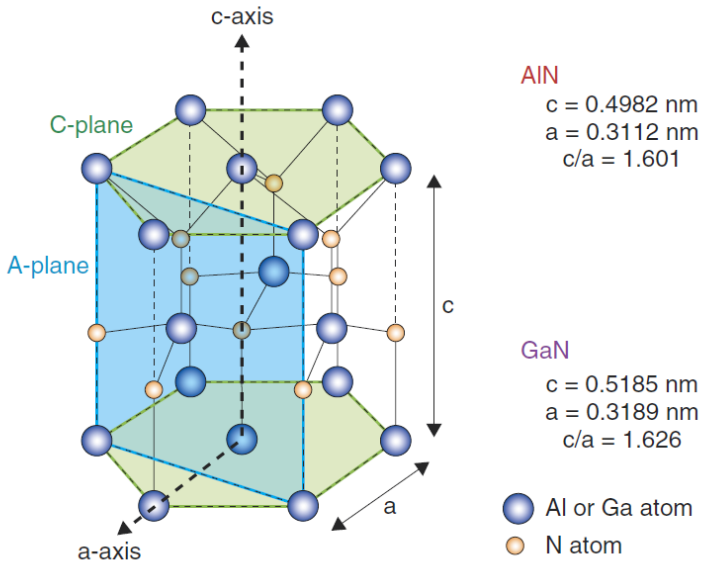

Figure B.1: Hexagonal wurtzite crystal structure of AlN and GaN [85].

A common technique to grow AlN bulk crystals is sublimation growth. This method has become prevalent towards other techniques like vapor cracking, plasma torch, flux growth and chemically aided vapor transport [32, 40, 41].

Aluminum Nitride (AlN) has a direct band gap of approximately 6 eV. Together with the wurtzite polytypes of InN and GaN it can form a continuous alloy system with a direct band gap ranging from 0.7 eV (InN) up to 6 eV (AlN). The dependence between band gap energy and lattice constant *a* of AlN, GaN, InN and their alloys is depicted in Figure B.2 for the wurtzite structure (solid black lines) and the zinc blende structure (dashed black lines).

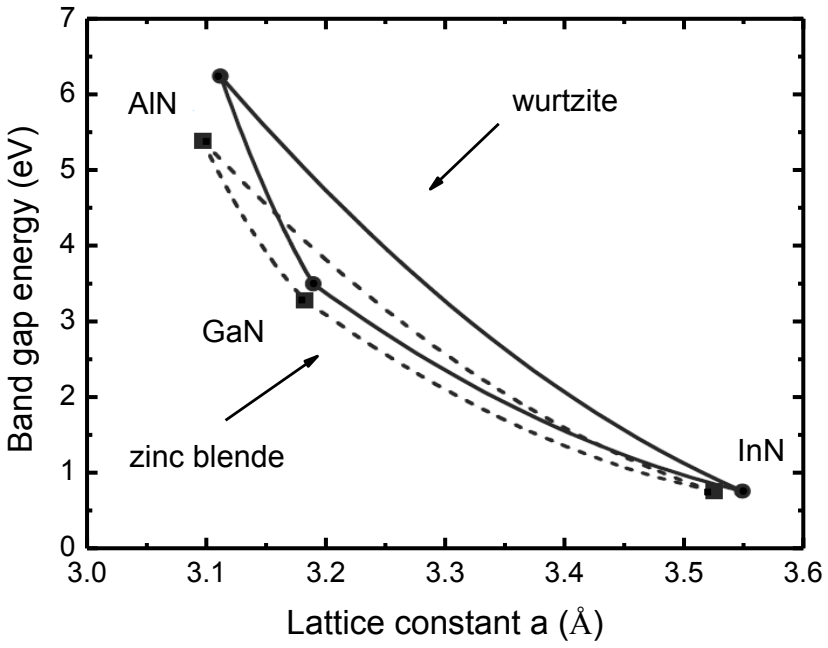

Figure B.2: Relation between band gap energy and lattice constant *a* for wurtzite structure AlN, GaN, InN, and their alloys (solid black lines). The same relation is depicted for the zinc blende structure with $a = a_{ZB}/\sqrt{2}$ (dashed black lines) [31].

C Gallium Oxide

β-Ga_2O_3 is under ambient conditions the thermodynamically stable phase in the gallium-oxygen system [107]. It crystallizes in the base centered monoclinic crystal structure with the C2/m space group, as depicted in Figure C.1 [56]. Doubly connected straight chains of edge shared GaO_6 octahedra run along the b-axis of the crystal and are connected by GaO_4 tetrahedra to one another [59]. One can see two cation positions, the tetrahedrally coordinated one marked as Ga(I) and the octahedrally coordinated Ga(II) position. In the case of the anion sites there are three crystallographically different positions. The first position, marked as O(I) is trigonally coordinated and is located at the intersection of two octahedra and one tetrahedron. Each O(II) is also trigonally coordinated and is shared between one octahedron and two tetrahedra. The third position, indicated as O(III) is tetrahedrally coordinated and lies at the corner of three octahedra and one tetrahedron [108]. β-Ga_2O_3 has the lattice parameters a = 1.223 nm, b = 0.304 nm, c = 0.580 nm and β = 103.7° [56].

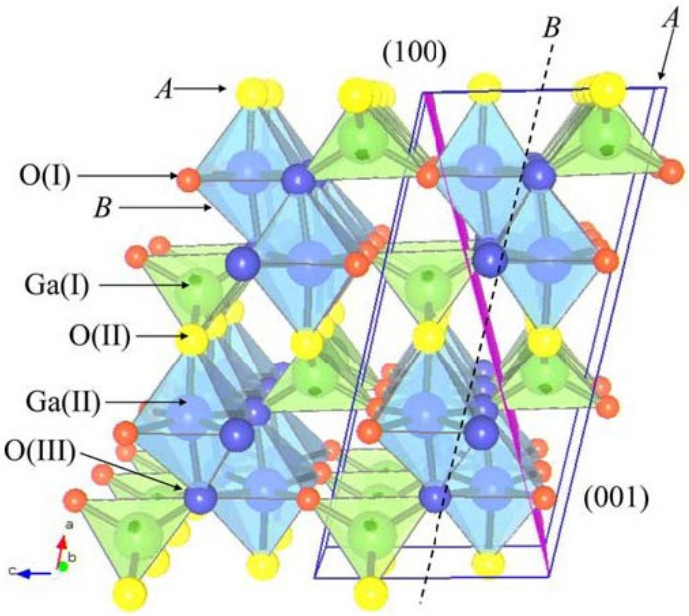

Figure C.1: Crystal structure of β-Ga_2O_3 [108].

A summary of spin-Hamilton parameters of impurities in β-Ga_2O_3 is given in Table C.1.

Table C.1: Spin-Hamilton parameters of impurities in β-Ga_2O_3

Center	Electron spin g-factor	Hyperfine interaction	Fine structure	Reference
Shallow donor (S = 1/2)	$g_x = 1.9601$ $g_y = 1.9629$ $g_z = 1.9649$	Not observed		[51]
Ti^{3+} (S = 1/2)	$g_x = 1.927$ $g_y = 1.952$ $g_z = 1.853$	Super-hyperfine splitting with Ga neighbors was resolved by ENDOR		[58]
Cr^{3+} (S = 3/2)	$g_x = 1.976$ $g_y = 1.9787$ $g_z = 1.9797$	Not observed	D = -14.03 GHz E = 6.157 GHz	[109]
Fe^{3+} (S = 5/2)	g = 2.0043	Not observed	D = 0.2212 cm^{-1} E = 0.0696 cm^{-1}	[78] [77]
Mn^{2+} (S = 5/2)	$g_x = 2.014$ $g_y = 2.012$ $g_z = 2.001$	$\|A_\perp\| = 82.7x10^{-4}$ cm^{-1} $\|A_\parallel\| = 80.7x10^{-4}$ cm^{-1}	D = 0.0510 cm^{-1} E = 0.0116 cm^{-1}	[110] [111]
Er^{3+} (S = 3/2)	$g_a = 5.75$ $g_b = 9.45$ $g_c = 0.9$	Hyperfine splitting with ^{167}Er (I = 7/2) was observed		[72]
Co^{2+} (S = 1/2)	$g_{\parallel a} \approx 2.8$ $g_{\perp a} = 6.4$	$\|A_{\parallel a}\| \approx 107$ Gauss $\|A_{\perp a}\| = 62$ Gauss		This work
Cu^{2+} (S = 1/2) Powder spectrum	^{63}Cu: $g_\parallel = 2.08$ $g_\perp = 2.4$ ^{65}Cu: $g_\parallel \approx 2.08$ $g_\perp = 2.38$	 $\|A_\parallel\| = 200$ MHz $\|A_\perp\| = 184$ MHz $\|A_\parallel\| \approx 200$ MHz $\|A_\perp\| = 246$ MHz		This work

D EPR spectrometer setup

The EPR measurements presented in this work were performed with a commercial available Bruker ESP 300E spectrometer. A klystron was used as microwave source, providing microwave frequencies ranging from 9.2 GHz up to 10 GHz with a maximum power of 200 mW. An Oxford Instruments helium flow cryostat, controlled by an ITC4, allowed measurements at temperatures ranging from 3.8 K up to 295 K. Figure D.1 shows a drawing of a Bruker ER 4102 ST universal x-band rectangular resonator, operating in the H_{102} mode, which was used as microwave cavity. There are two apertures in this resonator allowing the illumination of the sample. The first one is located on the front side of the resonator. Through that window it was possible to shine light of a laser diode array on the sample (see Table D.1 for wavelengths and powers).

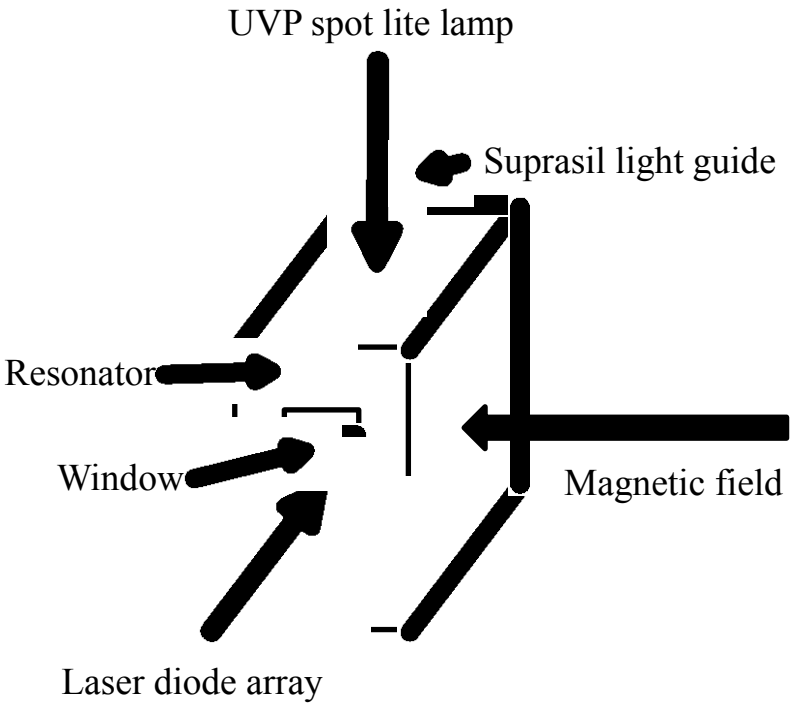

Figure D.1: Schematic drawing of the EPR resonator together with the available illumination sources.

The second aperture to the microwave cavity is realized through the sample holder, which is made of Herasil 102 (providing over 90 % transmittance from 200 nm up to 2000 nm) from the Heraeus Company in Germany. Through the latter light of an UVP

spot lite lamp, operating at 254 nm with a maximum power of 1 W per cm^2, was coupled into the sample. To assure that the light intensities were constant for all wavelengths, the intensity for a given wavelength at a certain distance was measured with a laser power meter and then adjusted to a fixed value by the use of gray filters.

A more detailed description of the EPR setup is given by [112].

Table D.1: Wavelengths and corresponding powers of the laser diode array.

Wavelength (nm)	Power (mW)
980	50
960	30
905	100
850	50
830	50
808	100
780	50
685	50
660	50

E Fundamental constants and useful conversion factors

Table E.1: Fundamental constants

Speed of light	c	2.9979×10^{8} m s^{-1}
Bohr magneton	μ_B	9.2740×10^{-24} J T^{-1} 5.7883×10^{-5} eV T^{-1}
Planck constant	h	6.6260×10^{-34} J s 4.1356×10^{-15} eV s
Boltzmann constant	k_B	1.3806×10^{-23} J K^{-1} 8.6173×10^{-5} eV K^{-1}
Free electron spin g-factor	g_e	2.0023
Nuclear magneton	μ_N	5.0507×10^{-27} J T^{-1}
Vacuum permeability	μ_0	12.5663×10^{-7} H m^{-1}
Free electron gyromagnetic ratio	γ_e	1.7608×10^{-11} s^{-1} T^{-1}

Conversion factors:

$$10^{-4} \cdot cm^{-1} = 2.9979\ MHz$$

$$A\ (MHz) = 2.80247 \left(\frac{g}{g_e}\right) A\ (Gauss)$$

F List of Figures

G Bibliography

[1] Bloch, F., W.W. Hansen, and M. Packard, Physical Review, **69**(3-4), 127 (1946).

[2] Mesiah, A., *Quantenmechanik*. Vol. Band 1. 1991: de Gruyter.

[3] Pilbrow, J.R., *Transition Ion Electron Paramagnetic Resonance*1991: Oxford University Press.

[4] Pake, G.E. and T.L. Estle, *The Physical Principles of Electron Paramagnetic Resonance*1973: Benjamin, W. A.

[5] Abragam, A. and B. Bleaney, *Electron Paramagnetic Resonance of Transition Ions*1970: Clarendon, P.

[6] Spaeth, M., H. Overhof, and H.-J. Queisser, *Point Defects in Semiconductors and Insulators*2003: Springer. 490.

[7] Spaeth, M., J.R. Niklas, and B.R. H., *Structural Analysis of Point Defects in Solids*1992: Springer.

[8] Godlewski, M., physica status solidi (a), **90**(1), 11-52 (1985).

[9] Desnica, U.V., Progress in Crystal Growth and Characterization of Materials, **36**(4), 291-357 (1998).

[10] Van de Walle, C.G., et al., Physical Review B, **47**(15), 9425-9434 (1993).

[11] Kobayashi, A., O.F. Sankey, and J.D. Dow, Physical Review B, **28**(2), 946-956 (1983).

[12] Look, D.C., et al., Appl. Phys. Lett., **81**(10), 1830-1832 (2002).

[13] Thonke, K., et al., Physica B: Condensed Matter, **308-310**(0), 945-948 (2001).

[14] Tsukazaki, A., et al., Nat Mater, **4**(1), 42-46 (2005).

[15] Lee, E.-C., et al., Physical Review B, **64**(8), 085120 (2001).

[16] Garces, N.Y., et al., Applied Physics Letters, **80**(8), 1334-1336 (2002).

[17] Carlos, W.E., E.R. Glaser, and D.C. Look, Physica B: Condensed Matter, **308-310**(0), 976-979 (2001).

[18] Garces, N.Y., et al., Journal of Applied Physics, **94**(1), 519-524 (2003).

[19] Gallino, F., et al., Journal of Materials Chemistry, **20**(4), 689-697 (2010).

[20] Janotti, A. and C.G. Van de Walle, Physical Review B, **76**(16), 165202 (2007).

[21] Tarun, M.C., M.Z. Iqbal, and M.D. McCluskey, AIP Advances, **1**(2), 022105 (2011).

[22] Garces, N.Y., et al., Appl. Phys. Lett., **81**(4), 622-624 (2002).

[23] Laiho, R., L.S. Vlasenko, and M.P. Vlasenko, J. Appl. Phys., **103**(12), 123709 (2008).

[24] Vlasenko, L.S. and G.D. Watkins, Physical Review B, **71**(12), 125210 (2005).

[25] Leiter, F.H., et al., physica status solidi (b), **226**(1), R4-R5 (2001).

[26] Meyer, B.K., et al., *Spectral Identification of Impurities and Native Defects in ZnO*. Zinc Oxide Materials for Electronic and Optoelectronic Device Applications2011: John Wiley & Sons, Ltd. 135-170.

[27] Sann, J., *Photolumineszenz gebundener Exzitonen in Zinkoxid*, in *Physics institute*2008, Justus-Liebig-University Giessen.

[28] Morton, J.R. and K.F. Preston, Journal of Magnetic Resonance (1969), **30**(3), 577-582 (1978).

[29] Poole, C., *Electron Spin Resonance: A Comprehensive Treatise on Experimental Techniques*1996: Courier Dover Publications.

[30] Lyons, J.L., A. Janotti, and C.G.V.d. Walle, Applied Physics Letters, **95**(25), 252105 (2009).

[31] Vurgaftman, I. and J.R. Meyer, J. Appl. Phys., **94**(6), 3675-3696 (2003).

[32] Bickermann, M., B.M. Epelbaum, and A. Winnacker, Journal of Crystal Growth, **269**(2-4), 432-442 (2004).

[33] Bickermann, M., et al., physica status solidi (a), **202**(4), 531-535 (2005).

[34] Darakchieva, V., et al., Appl. Phys. Lett., **80**(13), 2302-2304 (2002).

[35] A. Sarua, S.R., M. Kuball, N. Garro, O. Sancho, A. Cros, A. Cantarero, D. Olguin, B. Liu, D. Zhuang and J. H. Edgar MRS Proceedings, **798**(Y5), 17 (2003).

[36] Schweizer, S., et al., physica status solidi (b), **219**(1), 171-180 (2000).

[37] Youngman, R.A. and J.H. Harris, Journal of the American Ceramic Society, **73**(11), 3238-3246 (1990).

[38] Lan, Y.C., et al., Journal of Crystal Growth, **207**(3), 247-250 (1999).

[39] Cox, G.A., et al., Journal of Physics and Chemistry of Solids, **28**(4), 543-548 (1967).

[40] Slack, G.A. and T.F. McNelly, Journal of Crystal Growth, **34**(2), 263-279 (1976).

[41] Slack, G.A. and T.F. McNelly, Journal of Crystal Growth, **42**(0), 560-563 (1977).

[42] Mattila, T. and R.M. Nieminen, Physical Review B, **54**(23), 16676 (1996).

[43] Bickermann, M., et al., physica status solidi (b), **246**(6), 1181-1183 (2009).

[44] Pastrnak, J. and Roskovco.L, Physica Status Solidi, **26**(2), 591-& (1968).

[45] Soltamov, V.A., et al., Journal of Applied Physics, **107**(11), 113515-9 (2010).

[46] Orlinskii, S.B., et al., Physical Review Letters, **100**(25), 256404 (2008).

[47] Watkins, G.D., Advances in Solid State Physics, **24**, 163 (1984).

[48] Stampfl, C. and C.G. Van de Walle, Physical Review B, **65**(15), 155212 (2002).

[49] Tippins, H.H., Physical Review, **140**(1A), A316-A319 (1965).

[50] Lorenz, M.R., J.F. Woods, and R.J. Gambino, Journal of Physics and Chemistry of Solids, **28**(3), 403-404 (1967).

[51] Binet, L. and D. Gourier, Journal of Physics and Chemistry of Solids, **59**(8), 1241-1249 (1998).

[52] Orita, M., et al., Appl. Phys. Lett., **77**(25), 4166-4168 (2000).

[53] Tomm, Y., et al., Solar Energy Materials and Solar Cells, **66**(1-4), 369-374 (2001).
[54] Fleischer, M. and H. Meixner, J. Appl. Phys., **74**(1), 300-305 (1993).
[55] Ogita, M., et al., Applied Surface Science, **175-176**(0), 721-725 (2001).
[56] Geller, S., The Journal of Chemical Physics, **33**(3), 676-684 (1960).
[57] Dohy, D., G. Lucazeau, and A. Revcolevschi, Journal of Solid State Chemistry, **45**(2), 180-192 (1982).
[58] Binet, L., D. Gourier, and C. Minot, Journal of Solid State Chemistry, **113**(2), 420-433 (1994).
[59] Ueda, N., et al., Applied Physics Letters, **71**(7), 933-935 (1997).
[60] O'Donnell, K.P. and X. Chen, Appl. Phys. Lett., **58**(25), 2924-2926 (1991).
[61] Varshni, Y.P., Physica, **34**(1), 149-154 (1967).
[62] Huang, K. and A. Rhys, Proceedings of the Royal Society of London. Series A. Mathematical and Physical Sciences, **204**(1078), 406-423 (1950).
[63] Nogales, E., et al., J. Appl. Phys., **101**(3), 033517 (2007).
[64] Aubay, E. and D. Gourier, Physical Review B, **47**(22), 15023-15036 (1993).
[65] Boyn, R., et al., Journal of Physics: Condensed Matter, **7**(47), 9061 (1995).
[66] Shakurov, G., et al., Applied Magnetic Resonance, **28**(3), 251-265 (2005).
[67] Irmscher, K., et al., Physica B: Condensed Matter, **308-310**(0), 730-733 (2001).
[68] Abragam, A. and M.H.L. Pryce, Proceedings of the Royal Society of London. Series A. Mathematical and Physical Sciences, **206**(1085), 173-191 (1951).
[69] Galazka, Z., et al., Crystal Research and Technology, **45**(12), 1229-1236 (2010).
[70] de Wit, M. and A.R. Reinberg, Physical Review, **163**(2), 261-265 (1967).
[71] Elliott, R.J., Physical Review, **96**(2), 266-279 (1954).
[72] Vincent, J., et al., Journal of Applied Physics, **104**(3), 033519-6 (2008).
[73] Park, Y.J., et al., Journal of Crystal Growth, **264**(1-3), 1-6 (2004).
[74] Schwenzer, B., et al., Chemistry of Materials, **16**(24), 5088-5095 (2004).
[75] Miller, D.J. and D. Haneman, Physical Review B, **3**(9), 2918-2928 (1971).
[76] Müller, K.A. and J. Schneider, Physics Letters, **4**(5), 288-291 (1963).
[77] Gesmundo, F. and C. De Asmundis, Journal of Physics and Chemistry of Solids, **34**(4), 637-643 (1973).
[78] Meil'Man, M.L. and I.A. Gavrilov, Sov. Phys. Sol. State, **11**, 628 (1969).
[79] Trombetta, J.M., et al., Physical Review B, **43**(3), 2458-2461 (1991).
[80] Schneider, J., et al., Physics Letters, **5**(5), 312-315 (1963).
[81] Bozdog, C., et al., Physical Review B, **62**(19), 12923-12926 (2000).
[82] Keeble, D.J., Z. Li, and M. Harmatz, Journal of Physics and Chemistry of Solids, **57**(10), 1513-1515 (1996).
[83] Ozgur, U., et al., Journal of Applied Physics, **98**(4), 041301 (2005).
[84] Karzel, H., et al., Physical Review B, **53**(17), 11425-11438 (1996).

[85] Taniyasu, Y. and M. Kasu, NTT Technical Review, **8**(8) (2010).
[86] Schneider, J. and A. Räuber, Z. Naturforsch., **16a**, 712 (1961).
[87] Kasai, P.H., Physical Review, **130**(3), 989-995 (1963).
[88] Gonzalez, C., et al., Journal of Crystal Growth, **59**(1-2), 357-362 (1982).
[89] Block, D., A. Hervé, and R.T. Cox, Physical Review B, **25**(9), 6049-6052 (1982).
[90] Orlinskii, S.B., et al., Physical Review B, **77**(11), 115334 (2008).
[91] Hofmann, D.M., et al., Physical Review Letters, **88**(4), 045504 (2002).
[92] Vlasenko, L.S. and G.D. Watkins, Physical Review B, **72**(3), 035203 (2005).
[93] Smith, J.M. and W.E. Vehse, Physics Letters A, **31**(3), 147-148 (1970).
[94] Soriano, V. and D. Galland, physica status solidi (b), **77**(2), 739-743 (1976).
[95] Leutwein, K. and J. Schneider, Z. Naturforsch., **26a**, 1236 (1971).
[96] O.F, S., Journal of Physics and Chemistry of Solids, **29**(8), 1407-1429 (1968).
[97] Zwingel, D. and F. Gärtner, Solid State Communications, **14**(1), 45-49 (1974).
[98] Larach, S. and J. Turkevich, Journal of Physics and Chemistry of Solids, **29**(9), 1519-1522 (1968).
[99] Aliev, G.N., et al., Physical Review B, **70**(11), 115206 (2004).
[100] Hausmann, A. and E. Blaschke, Zeitschrift für Physik A Hadrons and Nuclei, **230**(3), 255-264 (1970).
[101] Holton, W.C., J. Schneider, and T.L. Estle, Physical Review, **133**(6A), A1638-A1641 (1964).
[102] Walsh, W.M., Jr. and L.W. Rupp, Jr., Physical Review, **126**(3), 952-955 (1962).
[103] Dorain, P.B., Physical Review, **112**(4), 1058-1060 (1958).
[104] Hausmann, A., physica status solidi (b), **31**(2), K131-K133 (1969).
[105] Dietz, R.E., et al., Physical Review, **132**(4), 1559-1569 (1963).
[106] Xia, Q., H. Xia, and A.L. Ruoff, Journal of Applied Physics, **73**(12), 8198-8200 (1993).
[107] Zinkevich, M. and F. Aldinger, Journal of the American Ceramic Society, **87**(4), 683-691 (2004).
[108] Bermudez, V.M., Chemical Physics, **323**(2-3), 193-203 (2006).
[109] Gunsser, W. and K. Rohwer, physica status solidi (b), **116**(1), 275-278 (1983).
[110] Folen, V.J., Physical Review, **139**(6A), A1961-A1964 (1965).
[111] Kim, I.G., et al., Journal of Applied Physics, **89**(8), 4470-4475 (2001).
[112] Henecker, F., *ESR- und ENDOR-Untersuchungen an neodymdotiertem stöchiometrischen Lithiumniobat*, in *Physics institute*1997, Justus-Liebig-University Giessen.

Acknowledgments

An dieser Stelle möchte ich mich bei allen bedanken, die zum Gelingen dieser Arbeit beigetragen haben.

Danke an:

- Prof. Dr. Bruno K. Meyer für die Möglichkeit diese Arbeit anzufertigen sowie die angenehme Arbeitsatmosphäre im I. Physikalischen Institut
- Prof. Dr. Detlev M. Hofmann für die Begutachtung und intensive Betreuung dieser Arbeit, sowie die vielen Gespräche über ESR und Festkörperphysik
- Dr. Albrecht Hofstaetter für die vielen Ratschläge zur ESR Spektroskopie und die tatkräftige Hilfe bei technischen Problemen mit dem Spektrometer
- Melanie Pinnisch für die PL Messungen
- Andreas Laufer für die SIMS Messungen
- PD Dr. Matthias Bickermann für die Bereitstellung der AlN Kristalle
- Dr.-Ing Eberhard Janata für die Elektronenbestrahlung der ZnO Proben
- Dr. Reinhard Uecker für die Bereitstellung der Ga_2O_3 Kristalle
- Daniel Röhrens für die nitridierten Ga_2O_3 Pulverproben
- Meinen Arbeitskollegen Dr. Swen Graubner, Dr. Joachim Sann, Anna Zagan, Achim Kronenberger, Daniel Reppin, Phillip Hering, Martin Becker, sowie den jetzigen und ehemaligen Mitgliedern des I. Physikalischen Instituts für die schöne Zeit und die Hilfe bei den vielen kleinen Problemen im Arbeitsalltag eines Physikers
- Friedel Nern und Andreas Katzer für die vielen Liter verflüssigten Heliums
- Allen technischen Mitarbeitern des I. Physikalischen Instituts, im besonderen Norbert Kurmann
- Allen Korrekturlesern
- Meiner Familie für die Unterstützung während meiner gesamten Studienzeit

Ich erkläre:

Ich habe die vorgelegte Dissertation selbständig und ohne unerlaubte fremde Hilfe und nur mit den Hilfen angefertigt, die ich in der Dissertation angegeben habe. Alle Textstellen, die wörtlich oder sinngemäß aus veröffentlichten Schriften entnommen sind, und alle Angaben, die auf mündlichen Auskünften beruhen, sind als solche kenntlich gemacht. Bei den von mir durchgeführten und in der Dissertation erwähnten Untersuchungen habe ich die Grundsätze guter wissenschaftlicher Praxis, wie sie in der „Satzung der Justus-Liebig-Universität Gießen zur Sicherung guter wissenschaftlicher Praxis“ niedergelegt sind, eingehalten.

Jan Eric Stehr